EFFECTS OF NOSE RADIUS AND AERODYNAMIC LOADING ON LEADING EDGE RECEPTIVITY

P.W. Hammerton & E.J. Kerschen

University of Arizona, Tucson, AZ 85721

July, 1998

Contents

List of Figures

Abstract

An analysis is presented of the effects of airfoil thickness and mean aerodynamic loading on boundary-layer receptivity in the leading-edge region. The case of acoustic free-stream disturbances, incident on a thin cambered airfoil with a parabolic leading edge in a low Mach number flow, is considered. An asymptotic analysis based on large Reynolds number is developed, supplemented by numerical results. The airfoil thickness distribution enters the theory through a Strouhal number based on the nose radius of the airfoil, $S = \omega r_n/U$, where ω is the frequency of the acoustic wave and U is the mean flow speed. The influence of mean aerodynamic loading enters through an effective angle-of-attack parameter μ, related to flow around the leading edge from the lower surface to the upper. The variation of the receptivity level is analyzed as a function of S, μ, and characteristics of the free-stream acoustic wave. For an unloaded leading edge, a finite nose radius dramatically reduces the receptivity level compared to that for a flat plate, the amplitude of the instability waves in the boundary layer being decreased by an order of magnitude when $S = 0.3$. Modest levels of aerodynamic loading are found to further decrease the receptivity level for the upper surface of the airfoil, while an increase in receptivity level occurs for the lower surface. For larger angles of attack close to the critical angle for boundary layer separation, a local rise in the receptivity level occurs for the upper surface, while for the lower surface the receptivity decreases. The effects of aerodynamic loading are more pronounced at larger values of S. Oblique acoustic waves produce much higher receptivity levels than acoustic waves propagating downstream parallel to the airfoil chord.

Chapter 1

Introduction

The accurate prediction of boundary-layer transition and the need to control this phenomenon are becoming increasingly important in the development of advanced aeronautical vehicles. These requirements have focused renewed attention on the physics of the transition process. It was known for many years that boundary-layer transition is influenced significantly by the free-stream disturbance environment. However, the physical mechanisms by which energy is transferred from the long wavelength free-stream disturbances to the much shorter wavelength instability waves were not understood. This came to be known as the receptivity problem (Morkovin 1969).

In order for an external disturbance to generate an instability wave, energy must be transferred to the unsteady motion in the boundary layer at an appropriate combination of frequency and wavelength. To simplify the discussion, it is useful to consider the situation where the external disturbance is of small enough amplitude that the unsteady motion can be represented as a linear perturbation of the mean flow. Attention can then be restricted to a single time harmonic, with the results for general time dependence obtained by superposition. In this report, we consider linear, time-harmonic disturbances to the mean flow.

The earliest theoretical analysis of instability wave generation in a boundary layer was presented by Gaster (1965). He considered the case of two-dimensional Tollmien-Schlichting (TS) wave excitation in a parallel boundary layer by a time-harmonic disturbance at the wall. The wall disturbance was localized in the streamwise direction, and hence the wavenumber spectrum of this disturbance was broad. Thus, the input disturbance contained energy at the appropriate frequency-wavelength combination to directly excite an instability wave.

The first attempts to predict receptivity to naturally occurring free-stream disturbances (Rogler & Reshotko 1975, Tam 1981) were based on a parallel flow formulation similar to that of Gaster. However, naturally occurring free-stream disturbances (sound waves, turbulence, etc.) travel at much higher speeds than instability waves. Thus, the wavenumber spectrum of the free-stream disturbance at a given temporal frequency is concentrated at wavenumbers which are significantly different than the wavenumber of the instability wave. Hence, these parallel flow analyses succeeded only in finding 'particular solutions' in the boundary layer which are unrelated to the instability wave. In order to transfer energy from a naturally occurring free-stream disturbance to an instability wave, a wavelength conversion process is required. A more complete discussion of the differences between instability wave generation by localized disturbances and by

1

naturally occurring disturbances can be found in Kerschen (1989).

Experimental investigations in the 1970s showed that receptivity can occur in the vicinity of the leading edge and in localized downstream regions. Reviews of these and more recent experiments are presented by Kachanov, Kozlov & Levchenko (1982) and Nishioka & Morkovin (1986). The experimental results stimulated theoretical investigations (Goldstein 1983, 1985) which showed that the wavelength conversion process takes place in regions of the boundary layer where the mean flow exhibits rapid changes in the streamwise direction. This occurs (a) near the body leading edge and (b) in any region farther downstream where some local feature forces the boundary layer to adjust on a short streamwise length scale. The rapid streamwise adjustment requires that nonparallel mean flow effects be included at leading order, in contrast to the parallel flow assumption of classical Orr–Sommerfeld stability theory. Reviews of receptivity are presented by Goldstein & Hultgren (1989) and Kerschen (1990). A discussion of the role of receptivity in transition prediction can be found in Heinrich, Choudhari & Kerschen (1988). Results for receptivity in localized downstream regions are presented in Kerschen, Choudhari & Heinrich (1989), Choudhari & Kerschen (1989, 1990) and Choudhari (1990), in addition to publications referenced above.

In this report, we present a theoretical analysis of receptivity in the leading-edge region. Previous theoretical studies of leading-edge receptivity have been restricted to the Blasius boundary layer on a semi-infinite, zero-thickness plate. The motion has been assumed incompressible and two-dimensional. Goldstein (1983) developed a high Reynolds number asymptotic analysis for this problem. The small parameter ϵ utilized in his analysis is defined as $\epsilon = (\omega \nu / U^2)^{-\frac{1}{6}}$, where ω is the frequency of the unsteady motion, ν is the kinematic viscosity of the fluid and U is the speed of the free stream. Note that ϵ^6 is the frequency parameter F of classical stability theory, which can also be interpreted as the inverse of a Reynolds number based on the convective wavelength U/ω of the unsteady motion.

Goldstein, Sockol & Sanz (1983) calculated the receptivity coefficient for an acoustic wave propagating downstream parallel to the surface of the flat plate. Heinrich & Kerschen (1989) calculated receptivity coefficients for a wide range of free-stream disturbances including obliquely incident acoustic waves, convected gusts (the linear representation of free-stream turbulence) of various orientations, and a von Karman vortex street passing above the plate surface. At low Mach numbers, the strong leading-edge diffraction field created by obliquely incident acoustic waves produces receptivity coefficients which are an order of magnitude larger than those for the other types of disturbances. The receptivity coefficient for oblique acoustic waves is proportional to $M^{-\frac{1}{2}}$ in the low Mach number limit, and the strongest receptivity occurs for acoustic waves propagating upstream toward the leading edge along one surface of the plate. Heinrich & Kerschen (1989) also examined the influence of wind tunnel walls on leading-edge receptivity to upstream propagating acoustic waves. A weakly damped oscillatory pattern as a function of frequency was found. The oscillations are related to the alternate cut-on of upstream and downstream traveling acoustic modes in the wind tunnel. For high frequencies, this pattern gradually approaches the isolated plate result. Various parts of Heinrich & Kerschen's results on leading-edge receptivity are summarized in publications referenced above; a full account can be found in Heinrich (1989).

The theoretical investigations of leading-edge receptivity discussed above have significantly advanced our understanding of the receptivity process. However, the results are

restricted to the incompressible, zero-pressure-gradient Blasius boundary layer on a plate of zero thickness. Bodies of practical interest generally have a leading edge with a finite radius of curvature, r_n, which enters the receptivity problem through the non-dimensional parameter $S = \omega r_n / U$. This parameter is typically $O(1)$ or larger in aerodynamic applications. Even in the case of laboratory experiments, S may be large enough to cause significant deviations from the zero-thickness model.

A second disadvantage of the zero-thickness geometry is that the influence of mean aerodynamic loading cannot be investigated, since any asymmetrical mean flow component in the vicinity of the leading edge leads to boundary-layer separation. It is well known that aerodynamic loading significantly influences both the mean development and the stability of the boundary layer. Hence, it is reasonable to anticipate that aerodynamic loading is an important parameter in the receptivity problem as well. In fact, in his laboratory experiments, P. Leehey found (private communication) that small changes in the 'angle of attack' of his plate produced dramatic changes in the receptivity to acoustic waves. Thus, in order to make predictions of relevance to practical applications, it is essential to incorporate both finite leading-edge thickness and mean aerodynamic loading into the receptivity theory.

In the present report, we extend the theory for leading-edge receptivity to address the effects of leading-edge thickness and mean aerodynamic loading. In chapter 2, a high Reynolds number asymptotic analysis ($\epsilon \ll 1$) of leading-edge receptivity is presented for the case of a symmetric mean flow past a parabolic leading edge. The nose radius parameter, $S = \omega r_n / U$, is assumed $O(1)$. We find that, when S reaches the value 0.3, the receptivity coefficient is reduced by an order of magnitude compared to the $S = 0$ case. The numerical results calculated under the assumption that $S = O(1)$ suggest that the receptivity coefficient is singular for small values of S. In chapter 3, the small-S behavior is investigated further by developing a small-S asymptotic theory. The leading term corresponding to $S = 0$ is found to agree with the flat-plate results of Heinrich and Kerschen (1989). For free-stream disturbances which produce a locally symmetric unsteady motion about the leading edge, the receptivity coefficient varies linearly for small S. However, for free-stream disturbances which induce an anti-symmetric component in the unsteady flow about the leading edge, the receptivity coefficient varies with $S^{\frac{1}{2}}$. This singular term leads to a sharp decrease in the amplitude of the receptivity coefficient relative to the flat-plate value. In chapter 4, the effects of mean aerodynamic loading are analyzed. The influence of aerodynamic loading enters through an effective angle-of-attack parameter μ, related to flow around the leading edge from the lower surface to the upper. Modest levels of aerodynamic loading are found to decrease the receptivity level for the upper surface of the airfoil, while the receptivity is increased for the lower surface. For larger angles of attack close to the critical angle for boundary layer separation, a local rise in the receptivity occurs for the upper surface, while on the lower surface the receptivity decreases. These effects are more pronounced at larger values of S. Conclusions of the study and recommendations for future work are summarized in chapter 5. This work has also been presented in Hammerton & Kerschen (1996, 1997, 1998).

Chapter 2

Receptivity for a leading edge with no aerodynamic loading

2.1   Introduction

The receptivity process through which free-stream disturbances generate instability waves in boundary layers was first discussed by Morkovin (1969). The transfer of energy from the free-stream disturbance to the instability wave generally comes about through non-parallel mean flow effects, which may arise either in the leading-edge region, or in a localized region farther downstream in the boundary layer (Goldstein & Hultgren 1989; Kerschen 1990).

Up to now, theoretical studies of leading-edge receptivity have been restricted to a semi-infinite, zero-thickness plate. Goldstein (1983) developed an asymptotic analysis for this problem; leading-edge receptivity coefficients for various free-stream disturbances were calculated by Goldstein et al. (1983) and Heinrich & Kerschen (1989). However, aerodynamic bodies designed for subsonic flow generally have finite thickness distributions with a parabolic leading edge. In the present chapter, we examine the influence of the thickness of a body on leading-edge receptivity. The body is assumed to be two-dimensional, with a symmetric cross-section and a parabolic leading edge. An asymptotic theory for the case of a symmetric mean flow is developed in this chapter. Results are presented for receptivity to acoustic waves in the free stream, incident on the body at arbitrary angle. Attention is focused on the variation of the receptivity level with the nose radius of the body and the incidence angle of the acoustic field.

In §2.2, a high Reynolds number asymptotic analysis ($\epsilon^6 = \nu\omega/U_e^2$; $\epsilon \ll 1$) is formulated for an incompressible, two-dimensional flow. This follows the approach of Goldstein (1983) but remains valid for a nose radius comparable to the free-stream disturbance length scale U_e/ω. Here U_e is an effective free-stream speed, defined in §2.2, which includes a correction to the free-stream velocity due to the flow perturbation created by downstream portions of the airfoil. Two streamwise regions enter the analysis, one region where the distance downstream is $O(U_e/\omega)$ and the disturbance is governed by the linearized unsteady boundary layer equation (LUBLE), and a second region at distances $O(\epsilon^{-2}U_e/\omega)$ where the disturbance is governed by the triple-deck structure, corresponding to the asymptotic form of the Orr-Sommerfeld equation (OSE) in the vicinity of the lower branch.

The structure of the solution in the LUBLE region is analyzed in §2.3. The inviscid

pressure field and slip velocity induced by the free-stream disturbance (analyzed in §2.4) drives the unsteady motion in the boundary layer. Far downstream in the LUBLE region, the solution consists of a Stokes wave, and a set of asymptotic eigensolutions that contain velocity but not pressure fluctuations. These asymptotic eigensolutions are equivalent to those obtained by Lam & Rott (1960) and Ackerberg & Phillips (1972), but modified to include the effects of the mean pressure gradient and surface curvature. The asymptotic analysis for distances far downstream determines the form of the eigenfunctions, but not their coefficients C_i. These coefficients can be found only through a full solution of the LUBLE, which must be determined by numerical methods. Lam & Rott (1993) have recently generalized their eigenfunctions to take account of arbitrary streamwise variation in the mean flow. The direct development in parabolic coordinates presented here is more convenient for our purposes, but it can be shown that our expressions for the eigenfunctions are in agreement with these more general results.

The wavelengths of the asymptotic eigenfunctions shorten progressively with distance downstream. Eventually, the self-induced pressure field associated with the displacement thickness of each asymptotic eigenfunction becomes significant, and the triple-deck structure replaces the LUBLE as the correct asymptotic approximation to the Navier-Stokes equation. The first asymptotic eigenfunction of the LUBLE matches on to the Tollmien-Schlichting wave solution of this triple-deck region. Thus, the form of the free-stream disturbance and the geometry close to the nose influence the amplitude of the Tollmien-Schlichting wave only through the coefficient C_1 of the first asymptotic eigenfunction. Therefore, we call C_1 the 'Receptivity Coefficient'. The primary objective of this chapter is to determine the Receptivity Coefficient as a function of leading-edge geometry and free-stream disturbance characteristics.

For the flat-plate case, it is not clear whether the set of eigensolutions obtained by Lam & Rott are complete. A second, very different set of eigensolutions was obtained by Brown & Stewartson (1973) which, they argue, better represent the physical properties of the flow. While the relationship between these two sets is a fundamental question which deserves further study, this must first be done in the context of the flat-plate problem. For a parabolic body, generalizations of the Brown & Stewartson eigensolutions should also exist, but we concentrate solely on the generalizations of the Lam-Rott solutions since it is demonstrated in Appendix B that they match naturally to the Orr-Sommerfeld modes further downstream.

In §2.4, the inviscid pressure field and slip velocity produced by the interaction of a free-stream acoustic wave with an airfoil are determined. The exact form of the unsteady slip velocity in the vicinity of the leading edge is determined by the global solution about the airfoil. This depends on the magnitude of the reduced acoustic frequency $k = \omega b/c$, where b is the airfoil semi-chord and c is the speed of sound. Here we present results for the limiting cases $k \ll 1$ and $k \gg 1$, when relatively simple expressions for the slip velocity can be obtained. Numerical solutions of the LUBLE are then carried out in §2.5, and comparisons with the asymptotic eigenfunctions of §2.3 are utilized to determine the Receptivity Coefficient C_1 as a function of $S = \omega r_n/U_e$ and characteristics of the free-stream acoustic wave. The analysis presented is for $S = O(1)$; the only restriction is that $S \ll \epsilon^{-2}$, so that the unsteady disturbance in the nose region is governed by the LUBLE.

2.2 Formulation
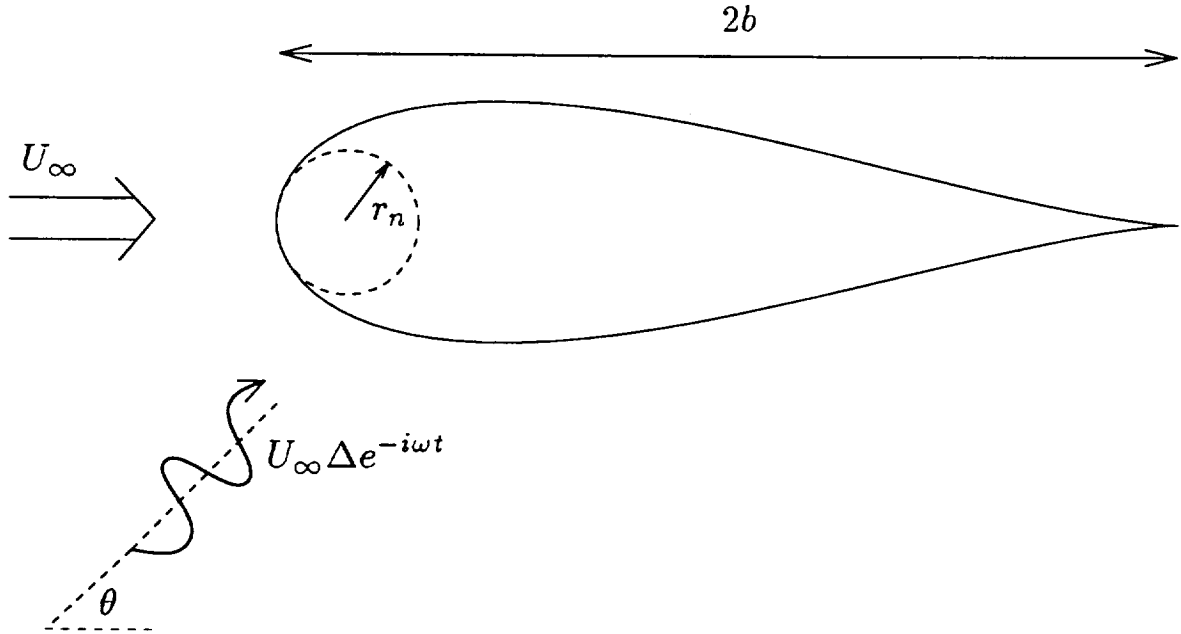
Figure 2.1: An illustration of the physical situation of interest: a thin, symmetric airfoil of chord $2b$ is at zero angle-of-attack in a uniform flow of speed U_∞, with a plane wave incident at an angle θ with respect to the airfoil chord.

We consider a thin, symmetric airfoil of chord $2b$ at zero angle-of-attack in a uniform flow of speed U_∞. A plane acoustic wave of frequency ω, propagating at an angle θ with respect to the airfoil chord, is assumed to be incident on the airfoil as illustrated in figure 2.1. Two-dimensional, low-Mach-number flow is considered. Since the Mach number is small, the mean flow can be analyzed using incompressible theory. For the unsteady component of the flow, most features of interest can also be analyzed with incompressible theory. The influence of compressibility on the unsteady component of the flow is discussed in §2.4. The Reynolds number is assumed large, so the flow field is inviscid and irrotational everywhere except in the vicinity of the airfoil surface.

2.2.1 Inviscid Outer Flow

Introducing Cartesian coordinates (x, y) normalized by the airfoil semi-chord b, with the origin located at the airfoil leading edge, the airfoil shape is given by

$$y = \pm \delta s\left(x\right), \qquad 0 \leq x \leq 2 \tag{2.1}$$

where $s\left(x\right)$ is the non-dimensional thickness distribution of the airfoil and the thickness parameter $\delta \ll 1$. The airfoil is assumed to have a rounded leading edge and a sharp trailing edge. The dimensional complex potential W for the steady, inviscid flow past

the airfoil is given by thin-airfoil theory,

$$W = U_\infty b \left[z + \delta \frac{1}{\pi} \int_0^2 \frac{ds}{dx_1} \ln\left(z - x_1\right) dx_1 + O\left(\delta^2\right) \right],$$ (2.2)

where $z = x + iy$ and the dimensional velocity (u, v) is given by $u - iv = b^{-1}dW/dz$.

For an airfoil with a rounded leading edge of radius r_n, the small argument expansion of the thickness distribution has the form

$$s\left(x\right) = s_1 x^{1/2} + s_2 x + s_3 x^{3/2} + O(x^2)$$ (2.3)

where $s_1 = (2r_n/\delta^2 b)^{1/2}$. The coefficient of the leading term in 2.3 must be $O\left(1\right)$, implying that $r_n = O(\delta^2 b)$. The thin-airfoil expansion 2.2 is invalid in the vicinity of the leading edge, and must be replaced by a local expansion (Van Dyke, 1964a: Chapter 4). The natural length scale for this local expansion is the airfoil nose radius r_n. Introducing a parabolic coordinate system $\left(\bar\xi, \bar\eta\right)$ in the local region, with r_n as the length scale,

$$x + iy = \frac{1}{2} \frac{r_n}{b} \left[\left(\bar\xi + i\bar\eta\right)^2 + 1 \right],$$ (2.4)

the airfoil surface is given by $\bar\eta = 1 + \frac{1}{2}\delta s_2 \bar\xi^3/(1 + \bar\xi^2) + O(\delta^2)$. Thus, at leading order in the local coordinates, the airfoil surface is defined by the parabola $\bar\eta = 1$.

The complex potential describing the leading approximation to the steady, inviscid flow in the vicinity of the airfoil nose is

$$W = \frac{1}{2}U_e r_n \left(\bar\xi + i\left(\bar\eta - 1\right)\right)^2,$$ (2.5)

leading to a slip velocity, $U_e \bar\xi/(\bar\xi^2 + 1)^{1/2}$, where the constant U_e is determined by matching with the thin airfoil expansion (2.2). For leading-edge shapes that contain a wedge component ($s_2 \neq 0$), the approximation (2.5) is valid only at $O(1)$ in the thickness parameter δ and matching with (2.2) then shows that $U_e = U_\infty$. However, for leading-edge shapes in which the $S^{\frac{1}{2}}$ multiplies a locally analytic function of x, the even coefficients in (2.3) vanish. The Joukowski airfoil is one example of such an airfoil. In this case the leading-edge region is also parabolic at $O(\delta)$, and the matching then gives

$$U_e = U_\infty + \frac{\delta}{\pi} \left\{ \frac{s_1}{2^{\frac{1}{2}}} - \int_0^2 \left[\frac{ds}{dx} - \frac{s_1}{2x^{\frac{1}{2}}} \right] \frac{dx}{x} \right\}.$$ (2.6)

The $O(\delta)$ term in (2.6) is essentially a correction to the 'free-stream speed' in the local leading-edge region, due to the flow perturbation created by downstream portions of the airfoil.

The scattering of the acoustic wave by the airfoil produces an unsteady perturbation to the inviscid, irrotational flow described above. This unsteady, inviscid perturbation is considered in §2.4. The slip velocity and pressure associated with the inviscid flow drive the viscous flow in the boundary layer adjacent to the airfoil surface.

2.2.2   Boundary-layer flow

The boundary-layer flow in the vicinity of the leading edge is also analyzed most conveniently in parabolic coordinates. Although the nose radius r_n is the most natural length scale for the steady flow, the length scale U_e/ω is more convenient for analysis of the unsteady flow. Thus, we introduce new coordinates,

$$\tilde{\xi} = S^{\frac{1}{2}}\,\bar{\xi}, \qquad \tilde{\eta} = S^{\frac{1}{2}}\,\bar{\eta}, \tag{2.7}$$

where

$$S = \frac{\omega r_n}{U_e} \tag{2.8}$$

is a Strouhal number based on the airfoil nose radius.

The flow around the body is analyzed in terms of the incompressible vorticity equation. Utilizing U_e for the velocity scale, U_e/ω for the length scale and ω^{-1} for the time scale, the non-dimensional form of the vorticity equation is

$$h^2\frac{\partial\tilde{\Omega}}{\partial t} + \frac{\partial(\tilde{\Omega},\tilde{\Psi})}{\partial(\tilde{\xi},\tilde{\eta})} = \epsilon^6\left(\frac{\partial^2\tilde{\Omega}}{\partial\tilde{\xi}^2} + \frac{\partial^2\tilde{\Omega}}{\partial\tilde{\eta}^2}\right), \tag{2.9}$$

where $\tilde{\Psi}$ is the streamfunction, the velocity is given by $\mathbf{v} = h^{-1}(\tilde{\Psi}_{\tilde{\eta}}\mathbf{e}_{\tilde{\xi}} - \tilde{\Psi}_{\tilde{\xi}}\mathbf{e}_{\tilde{\eta}})$, where $\mathbf{e}_{\tilde{\xi}}$ and $\mathbf{e}_{\tilde{\eta}}$ are unit vectors in the $\tilde{\xi}$ and $\tilde{\eta}$ coordinate directions, respectively, and the metric coefficient $h = (\tilde{\xi}^2 + \tilde{\eta}^2)^{\frac{1}{2}}$. The vorticity $-\tilde{\Omega}$ is related to the stream function by $\tilde{\Omega} = h^{-2}(\tilde{\Psi}_{\tilde{\xi}\tilde{\xi}} + \tilde{\Psi}_{\tilde{\eta}\tilde{\eta}})$. The small parameter

$$\epsilon^6 = \frac{\nu\omega}{U_e^2} \ll 1 \tag{2.10}$$

is the reciprocal of the Reynolds number based on the disturbance lengthscale. The flow satisfies the no-slip boundary conditions on the body surface,

$$\tilde{\Psi} = \tilde{\Psi}_{\tilde{\eta}} = 0, \qquad \text{on} \quad \tilde{\eta} = S^{\frac{1}{2}}, \tag{2.11}$$

where terms of higher order in δ have been neglected. The analysis presented here considers the small-ϵ limit but with $S = O(1)$.

Since the Reynolds number is assumed large, viscosity is important only in a thin boundary layer adjacent to the body surface. To analyze the boundary-layer flow, we set

$$\tilde{\eta} - S^{\frac{1}{2}} = \epsilon^3\eta, \qquad \tilde{\xi} = \xi, \qquad \tilde{\Psi} = \epsilon^3\Psi. \tag{2.12}$$

The incompressible vorticity equation, expressed in terms of the stream function, then becomes

$$\Psi_{\eta\eta t} + \frac{\partial(\Psi_{\eta\eta}/H^2,\Psi)}{\partial(\xi,\eta)} - \frac{\Psi_{\eta\eta\eta\eta}}{H^2} = \epsilon^6\left(\frac{\Psi_{\eta\eta\xi\xi}}{H^2} + \left[\frac{\Psi_{\eta\eta}}{H^2}\right]_{\xi\xi} - \frac{\partial(\Psi_{\xi\xi}/H^2,\Psi)}{\partial(\xi,\eta)} - \Psi_{\xi\xi t}\right)$$
$$+ \epsilon^{12}\left[\frac{\Psi_{\xi\xi}}{H^2}\right]_{\xi\xi}, \tag{2.13}$$

where $H = (\xi^2 + S)^{\frac{1}{2}}$. This equation is exact, except for the approximation that $h = H$ in the boundary layer. Careful consideration of the asymptotic structure, at all stages of the evolution of the disturbance, shows that the correction term $O(\epsilon^3\eta H^{-2})$ never becomes

significant and hence it is dropped throughout this presentation. At large values of η, the boundary-layer flow matches to the inviscid slip velocity,

$$H^{-1}\Psi_\eta \to U_s(\xi, t), \qquad \text{as} \quad \eta \to \infty. \tag{2.14}$$

For $O(1)$ values of ξ, the terms on the right side of (2.13) can be neglected, leading to the unsteady boundary-layer equation. The unsteady component of the flow, a small perturbation to the mean flow, then satisfies the linearized unsteady boundary layer equation (LUBLE). The LUBLE region is considered in the following section. However, the solution of the LUBLE contains components whose wavelengths progressively shorten with distance downstream. When $\xi = O(\epsilon^{-1})$, terms on the right hand side of (2.13) become significant and the correct asymptotic approximation to (2.13) has the triple-deck structure. The structure of the developing boundary layer is summarized in figure 2.2. The asymptotic matching of the two streamwise regions is discussed briefly at the end of §2.3.

2.3   Unsteady boundary-layer region

In this section, we consider (2.13) for $O(1)$ values of ξ in the limit $\epsilon \to 0$. Subsequently, the behavior of this solution at large values of ξ will be considered, in anticipation of matching with the Orr-Sommerfeld region that exists farther downstream in the boundary layer. For $\xi = O(1)$ and $\epsilon \to 0$, the terms on the right-hand side of (2.13) can be neglected. Integrating once with respect to η then gives the unsteady boundary-layer equation

$$H^2\Psi_{\eta t} + (\Psi_\eta\Psi_{\xi\eta} - \Psi_{\eta\eta}\Psi_\xi) - \xi H^{-2}\Psi_\eta{}^2 - \Psi_{\eta\eta\eta} = -H^2 P_\xi \tag{2.15}$$

where the pressure gradient $P_\xi(\xi, t)$ is obtained by matching to the outer (inviscid) flow,

$$P_\xi(\xi, t) = -H\frac{\partial U_s}{\partial t} - U_s\frac{\partial U_s}{\partial \xi}. \tag{2.16}$$

In this chapter, we consider uncambered airfoils at zero angle-of-attack to the mean flow. The slip velocity in the region of the parabolic nose is then given by

$$U_s(\xi, t) = \frac{\xi}{H} + \Delta\, u_s(\xi)e^{-it}, \tag{2.17}$$

where the steady contribution follows from (2.5), while the time-dependent perturbation depends on the particular form of the free-stream disturbance, as discussed in §2.4. Since the velocity field associated with an acoustic wave is of very small amplitude compared to the mean-flow speed, we assume that the amplitude scale factor $\Delta \ll 1$. The steady and unsteady components of the flow field can then be analyzed separately. Thus, the streamfunction within the boundary layer can be written in the corresponding form

$$\Psi = \xi\phi(\xi, \eta) + \Delta\, \psi(\xi, \eta)e^{-it}. \tag{2.18}$$

where extraction of the factor ξ from the mean-flow component is motivated by the form of (2.17). The function $\phi(\xi, \eta)$ describing the steady boundary-layer flow satisfies

$$\phi_{\eta\eta\eta} + \phi_{\eta\eta}\phi + \xi(\phi_{\eta\eta}\phi_\xi - \phi_\eta\phi_{\eta\xi}) - SH^{-2}(\phi_\eta{}^2 - 1) = 0, \tag{2.19}$$

U_∞ →

(iii)

(ii)

Outer edge of boundary
layer

(i)

$\eta = S^{1/2}$

η ξ

Orr-Sommerfeld Regime

LUBLE
Regime

Overlap
Region

$1 \ll \xi \ll \epsilon^{-1}$

S

$\xi = 0$

$\eta = 0$

U_∞ →
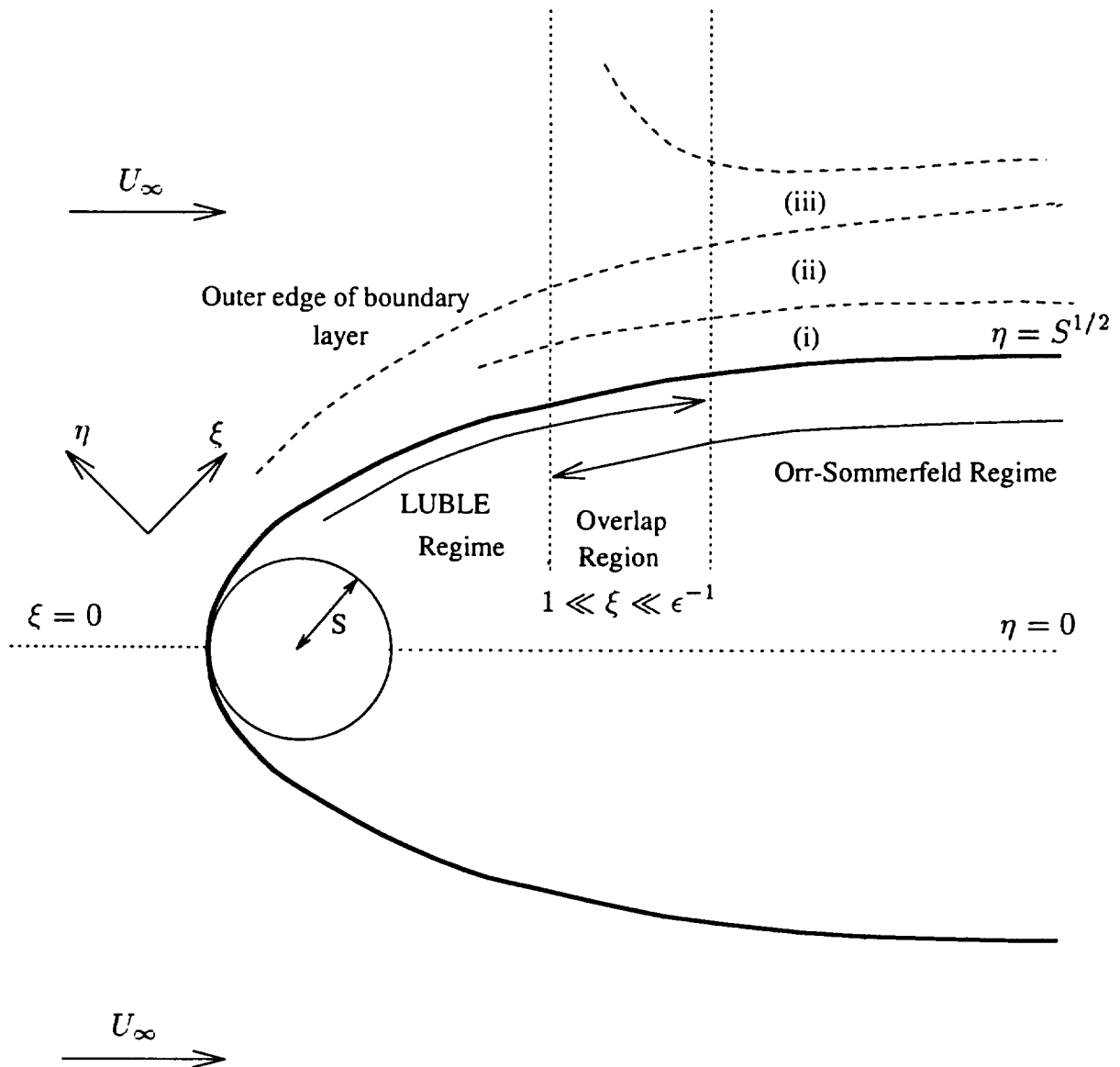
Figure 2.2: A schematic illustration of the boundary layer structure for a body with a parabolic leading-edge in a symmetric mean flow. The three decks in the Orr-Sommerfeld region are (i) the viscous wall layer; (ii) the main inviscid layer; and (iii) the outer irrotational layer.

with boundary conditions $\phi = \phi_\eta = 0$ at $\eta = 0$ and $\phi_\eta \to 1$ as $\eta \to \infty$. It may be observed that written in this form the steady equation involves S and hence it appears that the steady flow is dependent on ω, the frequency of the unsteady perturbation. However, ω also enters the scaling of the streamwise coordinate ξ. Re-writing (2.19) in terms of $\bar{\xi} = S^{-\frac{1}{2}}\xi$,

$$\phi_{\eta\eta\eta} + \phi_{\eta\eta}\phi + \bar{\xi}(\phi_{\eta\eta}\phi_{\bar{\xi}} - \phi_\eta\phi_{\eta\bar{\xi}}) - (1 + \bar{\xi}^2)^{-1}(\phi_\eta^2 - 1) = 0, \qquad (2.20)$$

it is seen that the steady flow is indeed independent of ω.

The time-dependent contribution to the boundary-layer flow satisfies the linearized unsteady boundary layer equation (LUBLE),

$$\left.\begin{array}{c} \mathcal{F}(\psi) = H^2\dfrac{\mathrm{d}p}{\mathrm{d}\xi}, \\[2mm] \mathcal{F}(\psi) \equiv \psi_{\eta\eta\eta} + (\phi + \xi\phi_\xi)\psi_{\eta\eta} + \left(iH^2 - \xi\phi_{\eta\xi} + \dfrac{\xi^2 - S}{H^2}\phi_\eta\right)\psi_\eta + \xi(\phi_{\eta\eta}\psi_\xi - \phi_\eta\psi_{\eta\xi}) \\[3mm] \dfrac{\mathrm{d}p}{\mathrm{d}\xi} = \left(iH - \dfrac{S}{H^3}\right)u_s - \dfrac{\xi}{H}\dfrac{\partial u_s}{\partial \xi}, \end{array}\right\} \tag{2.21}$$

with boundary conditions

$$\psi = \psi_\eta = 0 \quad \text{at} \quad \eta = 0 \quad \text{and} \quad \psi_\eta \to Hu_s \quad \text{as} \quad \eta \to \infty. \tag{2.22}$$

These equations must be solved numerically; the methods used are described in §2.5. However, as discussed in §2.1, we are primarily interested in the component of the unsteady field that, in the large-ξ limit, matches onto the Tollmien-Schlichting wave solution of the Orr-Sommerfeld equation. In the following two subsections, we develop large-ξ asymptotic solutions for the steady and unsteady components of the flow. For convenience, in the rest of this section we restrict attention to the upper surface of the body (*ie* $\xi > 0$). Corresponding results for $\xi < 0$ can be obtained by inspection.

2.3.1 Steady Boundary Layer Equation

In order to analyze the large-ξ behavior of the unsteady flow, the asymptotic form of the steady flow is required. The expansion for the steady flow is most naturally developed in terms of the streamwise coordinate scaled on the body nose radius, $\bar{\xi}$, as defined in (2.4). Far downstream of the nose ($\bar{\xi} \gg 1$), the pressure gradient for the steady flow past a parabola decays to zero and hence the mean flow approaches the flat-plate solution. The asymptotic form of the solution is given by Van Dyke (1964b),

$$\phi(\xi, \eta) \sim F(\eta) + A_1 G_1(\eta)\frac{\ln \bar{\xi}^2}{\bar{\xi}^2} + (B_1 G_1(\eta) + G_2(\eta))\frac{1}{\bar{\xi}^2}, \tag{2.23}$$

where $F(\eta)$ is the Blasius function, $G_1(\eta) = \eta F'(\eta) - F(\eta)$, A_1 and B_1 are as yet undetermined numerical constants, and $G_2(\eta)$ satisfies

$$G_2''' + FG_2'' + 2F'G_2' - F''G_2 = F'^2 - 1 + 2A_1FF'', \qquad G_2(0) = G_2'(0) = G_2''(0) = 0. \tag{2.24}$$

The value of A_1 is fixed by the physical requirement of exponential decay of vorticity at the outer edge of the boundary layer. Hence $G_2(\eta)$ must decay exponentially for large η, which gives $A_1 = 0.60115$. The value of B_1 cannot be determined by the large-ξ analysis since $\bar{\xi}^{-2}G_1(\eta)$ is an eigensolution of the perturbation equation. The next term in the expansion is $O(\bar{\xi}^{-\alpha})$, $\alpha \approx 3.774$, the fractional power arising as the next eigensolution of an infinite sequence (Libby & Fox, 1963). It appears that B_1, together with the set of similar constants appearing in higher-order terms, is dependent on conditions close to the nose of the body and hence can be determined only by numerical integration from $\bar{\xi} = 0$. This we discuss in §2.5. The next four ignored terms in the expansion are of order $\bar{\xi}^{-3.774}$, $\bar{\xi}^{-4}\ln^2\bar{\xi}$, $\bar{\xi}^{-4}\ln\bar{\xi}$ and $\bar{\xi}^{-4}$. As we will demonstrate in due course, the fact that these terms are of similar magnitude until $\bar{\xi}$ is extremely large poses certain problems in the numerical treatment of the problem.

In developing the solution to the LUBLE, the limiting behavior of the steady flow close to the surface is required. This is found to be

$$\phi \sim \frac{U_0'\eta^2}{2}\left(1 + A_1\frac{\ln\bar{\xi}^2}{\bar{\xi}^2} + B_1\frac{1}{\bar{\xi}^2}\right) - \frac{\eta^3}{6}\frac{1}{\bar{\xi}^2} - \frac{U_0'^2\eta^5}{5!} + O(\eta^2\bar{\xi}^{-3.774}, \eta^5\bar{\xi}^{-2}\ln\bar{\xi}), \quad (2.25)$$

where $U_0' \equiv F''(0) = 0.4696$.

2.3.2 Linearized Unsteady Boundary Layer Equation

We now consider the evolution of the unsteady perturbation to the mean flow, which is governed by (2.21). Far downstream ($\xi \gg 1$), the unsteady component of the stream-function consists of a particular solution, ψ_p, determined entirely by the local conditions far downstream, together with a set of asymptotic eigensolutions,

$$\psi(\eta, \xi; S) = \psi_p(\eta, \xi; S) + \sum_i C_i(S)\psi_i(\eta, \xi; S). \quad (2.26)$$

The particular solution is a generalization of the classical Stokes layer solution, driven by the local value of the unsteady pressure gradient (2.21), see Lighthill (1954) for details. The eigensolutions ψ_i depend on the geometry of the body far downstream, but are independent of the local free-stream disturbance. These eigensolutions are generalized forms of the eigenfunctions found by Lam & Rott (1960) for the flat-plate boundary layer, taking account of the non-Blasius mean flow. The coefficients C_i multiplying the asymptotic eigenfunctions are determined entirely by conditions close to the leading edge ($\xi = O(1)$). One of these eigensolutions, which we label ψ_1, matches on to the Tollmien-Schlichting wave in the Orr-Sommerfeld region farther downstream, where $\xi = O(\epsilon^{-1})$. Thus, it is only through the coefficient C_1 that the unsteady disturbances in the free stream influence the amplitude of the Tollmien-Schlichting wave.

Our primary interest is in the relationship between the free-stream disturbances and the amplitude of the Tollmien-Schlichting wave. Thus, we focus on the asymptotic eigensolutions of the LUBLE. Guided by the results for the flat-plate case (Goldstein, 1983), we anticipate the development of a two-layer structure for $\xi \gg 1$, consisting of a main layer where $\eta = O(1)$ and a new inner layer of width $O(\xi^{-1})$.

Inner layer

Introducing an inner variable $m = \xi\eta$, the homogeneous form of the LUBLE then becomes

$$\psi_{mmm} + i(1 + \frac{S}{\xi^2})\psi_m + \frac{U_0' m}{2\xi^3}(2\psi_m - m\psi_{mm}) + O\left(\frac{\ln\xi}{\xi^5}\right)$$

$$= \tag{2.27}$$

$$\frac{1}{\xi^2}\left\{ U_0'\,\gamma(\xi/S^{\frac{1}{2}})(m\psi_{m\xi} - \psi_\xi) - \frac{Sm}{2\xi^3}(m\psi_{m\xi} - 2\psi_\xi) - \frac{U_0'^2 m^3}{24\xi^3}(m\psi_{m\xi} - 4\psi_\xi)\right\}$$

where it follows from (2.23) that $\gamma(\bar\xi) = 1 + 2A_1\ln\bar\xi/\bar\xi^2 + B_1/\bar\xi^2 + O(\bar\xi^{-3.774})$. The regular perturbation solution to (2.28), for large ξ, leads to solutions related to the particular solution ψ_p. Thus, the asymptotic eigensolutions must arise as a balance between the highest m derivative (*i.e.* wall-normal derivative) and the terms involving ξ derivatives. It is then clear that the eigensolution must contain a factor $\exp(T(\xi))$ and it is for this reason that the higher order terms containing derivatives with respect to ξ have been retained in (2.28).

Writing $\psi = \exp(T(\xi))f(\xi, M)$, where a new boundary layer variable $M = m(1 + S/2\xi^2)$ has been introduced to simplify the solution, $f(\xi, M)$ satisfies

$$f_{MMM} + if_M - \frac{U_0'\Gamma(\xi/\sqrt{S})}{\xi^2}\frac{dT}{d\xi}(Mf_M - f) = \frac{1}{\xi^3}R + O(\frac{1}{\xi^4}), \tag{2.28}$$

where $\Gamma(\bar\xi) = \gamma(\bar\xi) - 3/2\bar\xi^2$ and

$$R = U_0'\xi(Mf_{M\xi} - f_\xi) + \frac{U_0'}{2}(M^2 f_{MM} - 2Mf_M)$$

$$-\frac{U_0'^2 M^3}{4!\,\xi^2}\frac{dT}{d\xi}(Mf_M - 4f) - \frac{SM}{2\xi^2}\frac{dT}{d\xi}(Mf_M - 2f). \tag{2.29}$$

If $dT/d\xi$ is set equal to $-\lambda\xi^2/U_0'\Gamma$, where λ is an eigenvalue to be determined subsequently, solution to the leading order equation immediately follows using separation of variables,

$$\psi \sim D\xi^{2\tau}e^{T(\xi)}[p(M) + \xi^{-3}q(M) + \ldots]. \tag{2.30}$$

Here D is an arbitrary constant whose value is chosen for convenience later, and τ is a constant that is determined at a later stage of the analysis. The exponent $T(\xi)$ is then determined by integrating the large-ξ expansion of $\xi^2/\Gamma(\xi/S^{\frac{1}{2}})$. This exponent can be separated into two components, $T = T^{(0)} + T^{(1)}$, where

$$T^{(0)}(\xi) = -\frac{\lambda\xi^3}{U_0'}\left\{\frac{1}{3} - A_1 S\frac{\ln(\xi^2/S)}{\xi^2} + (2A_1 + 3/2 - B_1)\frac{S}{\xi^2}\right\} \tag{2.31}$$

is large for large ξ and hence must be included in the leading-order form of the eigensolution, while the terms in $T^{(1)}(\xi)$ are small for $\xi \gg 1$ and thus could be considered as algebraic correction terms rather than as exponential amplitude functions. The first few terms in $T^{(1)}$ are of the form

$$T^{(1)}(\xi) = b_1 S^{1.887}\frac{1}{\xi^{0.774}} + b_2 S^2\frac{\ln^2(\xi^2/S)}{\xi} + b_3 S^2\frac{\ln(\xi^2/S)}{\xi} + b_4 S^2\frac{1}{\xi} + O\left(\xi^{-2.635}\right). \tag{2.32}$$

13

where the coefficients b_i are determined by the higher order terms of (2.25).

The leading-order mode-shape function $p(M)$ satisfies the differential equation

$$\mathcal{L}(p) = 0, \qquad (2.33)$$

where the operator $\mathcal{L}$ is defined by

$$\mathcal{L}(p) \equiv p''' + \mathrm{i}p' + \lambda(Mp' - p), \qquad (2.34)$$

with $p' \equiv p_M$, etc. The boundary conditions at the wall are

$$p(0) = p'(0) = 0, \qquad (2.35)$$

and matching to the main layer requires that $p'' \to 0$ as $M \to \infty$ so as to avoid exponential growth of the inner solution. The differential operator and boundary conditions are homogeneous and thus form an eigenvalue problem for λ. In fact, the leading-order equation is identical to the flat-plate equation, the effect of curvature having been absorbed into the boundary-layer variable M. Thus $p(M)$ and the value of the eigenvalue $\lambda = \mathrm{e}^{-\frac{1}{4}\mathrm{i}\pi}\rho^{-\frac{3}{2}}$ can be obtained immediately from Goldstein (1983) as

$$p(M) = \frac{U_0' \int_0^M (M - \tilde{M})\mathrm{Ai}(\tilde{z})\mathrm{d}\tilde{M}}{\int_0^\infty \mathrm{Ai}(\tilde{z})\mathrm{d}\tilde{M}}, \qquad \tilde{z} = \mathrm{e}^{\frac{1}{4}\mathrm{i}\pi}\rho^{-\frac{1}{2}}\tilde{M} - \rho, \qquad (2.36)$$

where ρ is a solution of $\mathrm{Ai}'(-\rho) = 0$. An infinite set of such roots ($\rho_i > 0$) exists, with corresponding mode-shape functions $p_i(M)$.

The value of τ for each eigensolution, ψ, is then determined by a solvability condition on the $O(\xi^{-3})$ correction to the mode shape, $q(M)$. This function satisfies

$$\mathcal{L}(q) = \mathcal{R}(p), \qquad (2.37)$$

where

$$\mathcal{R}(p) \equiv 2\tau U_0'(Mp' - p) + \frac{U_0'}{2}(M^2 p'' - 2Mp') - \frac{U_0' M^3}{4!}(Mp' - 4p) + \frac{S\lambda M}{2U_0'}(Mp' - 2p). \qquad (2.38)$$

The boundary conditions at the wall and the matching condition to the main layer are the same as for $p(M)$. Integrating by parts and using the boundary/matching conditions on p and q gives the relation

$$\int_0^\infty p''' \mathcal{L}(q)\mathrm{d}M = \int_0^\infty q''' \mathcal{L}(p)\mathrm{d}M, \qquad (2.39)$$

the right hand side vanishing by virtue of (2.33). Hence τ is determined by the condition

$$\int_0^\infty p''' \mathcal{R}(p)\mathrm{d}M = 0. \qquad (2.40)$$

This gives $\tau = \tau^{(0)} + S\tau^{(1)}$, where $\tau^{(0)}$ is the flat-plate value and

$$\tau^{(1)} = -\frac{\mathrm{e}^{-\frac{1}{4}\mathrm{i}\pi}}{4U_0'^2 \rho^{\frac{3}{2}}} \frac{\int_0^\infty Mp'''(Mp' - 2p)\mathrm{d}M}{\int_0^\infty p'''(Mp' - p)\mathrm{d}M}. \qquad (2.41)$$

14

It should be noted that this result does not involve linearization in S, but is valid for $S = O(1)$. By suitable change of variables, this can be re-cast into the form

$$\tau^{(1)} = \frac{\mathrm{i}}{4U_0'^2 \rho} \frac{J_2 - 2\mathrm{Ai}^2(-\rho)}{J_1},$$

$$= \frac{8\rho^3 - 27}{40 U_0'^2 \rho^3} \mathrm{i} \qquad (2.42)$$

where expressions for the integrals $J_n = \int_{-\rho}^{\infty} (z + \rho)^n [\mathrm{Ai}(z)]^2 \mathrm{d}z$ are given in Appendix A. Similarly, the expression for $\tau^{(0)}$ (Goldstein, 1983) can be expressed in terms of ρ, avoiding the need for numerical evaluation of the integrals,

$$\tau^{(0)} = \frac{1}{4}\left(-3 + \frac{1}{12}\frac{J_4}{J_1}\right) = -\frac{889 - 16\rho^3}{1260}. \qquad (2.43)$$

The value of τ_i for each eigensolution is obtained by substituting ρ_i into (2.42) and (2.43). Finally, we set the value of the arbitrary constant in (2.30) to $D = 2^{-\tau}$ so that, in the limit $S \rightarrow 0$, our expression for the asymptotic eigenfunction reduces to the result given by Goldstein (1983).

Main layer

In the main part of the boundary layer, where $\eta = O(1)$, the unsteady motion is essentially an inviscid response, driven by the displacement thickness of the inner layer. Setting $\psi = (\xi^2/2)^\tau \exp(T(\xi))g(\xi, \eta)$ and substituting into the homogeneous form of the LUBLE, $g(\xi, \eta)$ is found to satisfy

$$\phi_{\eta\eta} g - \phi_\eta g_\eta = \mathrm{e}^{\frac{1}{4}\mathrm{i}\pi} \rho^{\frac{3}{2}} U_0' \left(\frac{\mathrm{i}g_\eta}{\xi} + \frac{(\phi_{\eta\eta} g_\xi - \phi_\eta g_{\eta\xi})}{\xi^2}\right) + O(\xi^{-3}). \qquad (2.44)$$

Solving, and matching to the inner layer then gives

$$g = \xi\left(F'(\eta) + \frac{\mathrm{e}^{\frac{3}{4}\mathrm{i}\pi} \rho^{\frac{3}{2}} U_0'}{\xi} + O(\xi^{-2})\right). \qquad (2.45)$$

Large-ξ matching

In Appendix B it is shown that it is the first asymptotic eigensolution which matches on to the Tollmien-Schlichting wave that becomes unstable farther downstream. In §2.5, numerical solutions of the LUBLE are compared to the first asymptotic eigenfunction, in order to extract the receptivity coefficient C_1. The two most convenient points of comparison are the wall shear and the displacement thickness of the boundary layer. The wall shear is determined by the solution in the inner layer. However, for comparison with numerical solutions, it is most convenient to express the wall shear in terms of a derivative with respect to η. Rewriting (2.30) in terms of η and evaluating $\psi_{\eta\eta}$ at $\eta = 0$, the contribution to the wall shear due to the asymptotic eigensolution ψ_i is

$$\psi_i''(\eta = 0) = \left(\frac{\xi^2}{2}\right)^{\tau_i} \mathrm{e}^{T_i(\xi)} \xi^2 \frac{U_0' \rho_i^{-\frac{1}{2}} \mathrm{e}^{\frac{1}{4}\mathrm{i}\pi}}{\int_0^\infty \mathrm{Ai}(z - \rho_i)\, \mathrm{d}z}(1 + O(\xi^{-2})). \qquad (2.46)$$

15

Taking the first root of $\mathrm{Ai}'(-\rho) = 0$, namely $\rho_1 = 1.01879$, and evaluating the numerical coefficient, the wall shear for the first asymptotic eigensolution is

$$\psi_1''(\eta = 0) = 0.4356(1 + \mathrm{i})\mathrm{e}^{T_1^{(0)}(\xi)} \left(\frac{\xi^2}{2}\right)^{\tau_1+1} \mathrm{e}^{T_1^{(1)}(\xi)} \left(1 + O(\xi^{-2})\right), \qquad (2.47)$$

where $T_1^{(0)}(\xi)$ is given by (2.31), $T_1^{(1)}(\xi)$ is a small correction term given by (2.32) and

$$\tau_1 = -0.69213 - S\,1.9878\,\mathrm{i}. \qquad (2.48)$$

The contribution to the displacement thickness due to an asymptotic eigensolution is obtained from the solution in the main layer,

$$\psi_i(\eta \to \infty) \sim \left(\frac{\xi^2}{2}\right)^{\tau_i} \mathrm{e}^{T_i(\xi)}\xi \left(1 + \frac{\mathrm{e}^{\frac{3}{4}\mathrm{i}\pi}\rho_i^{\frac{3}{2}}U_0'}{\xi} + O(\xi^{-2})\right), \qquad (2.49)$$

where the result for the first asymptotic eigensolution ψ_1 follows by substituting ρ_1 and τ_1.

Since $T \propto \xi^3$ at leading order, the wavelengths of the asymptotic eigenfunctions decrease with distance downstream, increasing the importance of longitudinal derivatives. The LUBLE (2.15) is obtained from (2.13) by neglecting higher-order derivatives with respect to ξ. Thus, although the asymptotic eigensolutions derived in this section are uniformly valid solutions of the LUBLE as $\xi \to \infty$, they are not uniformly valid solutions of the full linearized Navier-Stokes equation.

Terms on the right side of (2.13), which were neglected in the LUBLE, become significant when $\xi = O(\epsilon^{-1})$. An irrotational layer outside the mean boundary layer, driven by the oscillating displacement thickness of the eigensolutions, must then be considered, and the associated pressure gradient appears in the leading-order equations governing the inner layer. This coupled viscous-inviscid interaction has the triple-deck structure, corresponding to the small-ϵ asymptotic approximation to the Orr-Sommerfeld equation in the vicinity of the lower branch. The development of the boundary layer structure was summarized in figure 2.2. A complete treatment of the linear development of the instability would require an asymptotic solution for the Tollmien-Schlichting wave of the Orr-Sommerfeld equation, taking account of the surface curvature and non-zero pressure gradient. This Tollmien-Schlichting wave solution could then be matched to the first Lam-Rott asymptotic eigensolution of the LUBLE, as was done by Goldstein (1983) for the flat-plate case. However, for $O(1)$ values of S, with ϵ and δ of the same order, the Orr-Sommerfeld region is influenced by the full airfoil thickness distribution, necessitating a general development that does not seem justified in the present context. For flow around a semi-infinite parabolic body, we verify in Appendix B that the eigensolutions obtained here do indeed match on to the Tollmien-Schlichting wave.

In this chapter we restrict ourselves to examining only the receptivity process, that is, the determination of the coefficient C_1 of the first eigensolution, which matches to the unstable Tollmien-Schlichting mode. The remainder of the chapter is concerned with obtaining the Receptivity Coefficient for different free-stream disturbances. This is accomplished by comparing numerical solutions with the asymptotic solutions obtained above.

16

2.4 Free-stream Disturbances

In this section we consider the inviscid flow field produced by the interaction of a free-stream acoustic wave with the airfoil. The acoustic wave is assumed to be incident on the airfoil at an angle θ with respect to the airfoil chord, as illustrated in figure 2.1. The slip velocity and surface pressure fields generated by this interaction drive the unsteady motion in the boundary layer, leading to the generation of a Tollmien-Schlichting wave.

For a low Mach number flow, the acoustic wavelength $2\pi c/\omega$ is long compared to the hydrodynamic length scale U_∞/ω. Thus, outside the boundary layer, the unsteady flow in the vicinity of the leading edge is incompressible and irrotational. Potential flow theory then shows that this local flow has the form

$$u_s(\xi) = \kappa_s(\theta)\frac{\xi}{H} + \kappa_a(\theta)\frac{1}{H}. \tag{2.50}$$

Here ξ/H and $1/H$ correspond to purely symmetric and anti-symmetric flow about the leading edge, respectively. The coefficients κ_s and κ_a multiplying these eigenfunctions are independent of the nose geometry, but depend on the free-stream disturbance, being determined by global features of the unsteady flow. Substituting (2.50) into (2.21) gives

$$\mathcal{F}(\psi) = \kappa_s\xi\left(iH^2 - \frac{2S}{H^2}\right) + \kappa_a\left(iH^2 + \frac{\xi^2 - S}{H^2}\right). \tag{2.51}$$

Hence, writing $\psi = \kappa_s\psi_s + \kappa_a\psi_a$, it follows that the Receptivity Coefficient for the upper surface is given by

$$C_1(S) = \kappa_s(\theta)\,C_s(S) + \kappa_a(\theta)\,C_a(S), \tag{2.52}$$

where C_s and C_a are extracted from the solutions of

$$\left.\begin{aligned}
\mathcal{F}(\psi_s) &= \xi\left(iH^2 - \frac{2S}{H^2}\right) \\
\mathcal{F}(\psi_a) &= iH^2 + \frac{\xi^2 - S}{H^2}
\end{aligned}\right\} \tag{2.53}$$

respectively. The corresponding Receptivity Coefficient for the lower surface is obtained by replacing θ by $-\theta$.

The remainder of this section is concerned with calculating $\kappa_s(\theta)$ and $\kappa_a(\theta)$, the coefficients of symmetric and anti-symmetric flow about the nose. These coefficients are found by asymptotic matching of the local solution (2.50) for the unsteady slip velocity with an appropriate global solution. The nature of this solution depends upon the magnitude of the reduced acoustic frequency $k = \omega b/c$, where c is the speed of sound in the undisturbed medium. Calculation of the velocity field about a thin wing, including compressibility effects, is described in Sedov (1965: Chapter 2, pp 87–107). In general no simple expression for the slip velocity can be obtained. Here we consider two cases that do lead to relatively simple results. The first case is that of extremely low Mach numbers, such that the acoustic wavelength is long not only compared to the hydrodynamic length scale, U_∞/ω, but also compared to the airfoil chord, i.e., $k \ll 1$. In this situation the unsteady interaction of the acoustic wave with the airfoil can be analyzed using the classical unsteady airfoil theory for incompressible flow. The second

17

case is that of acoustic wavelengths long compared to U_∞/ω but short compared to the airfoil chord, i.e., $k \gg 1$. In this case acoustic diffraction theory can be used to analyze the interaction.

First consider the case $k \ll 1$, where incompressible, unsteady airfoil theory applies (see for example, Garrick, 1957). Since the airfoil semi-chord is the relevant length scale for the unsteady aerodynamic interaction, the airfoil thickness can be ignored (except in the region of the leading-edge, where (2.50) is applicable). Thus, the airfoil reduces to a zero-thickness flat plate, and the solution consists of two potential flow components, a non-circulatory component, plus a component due to the vorticity shed from the sharp trailing edge. The shed vorticity is convected downstream by the mean flow and hence takes the form $\gamma(x,t) = \hat{\gamma}e^{i(ax-t)}$ where $a = \omega b/U_e$ is the aerodynamic reduced frequency. The non-dimensional complex potential for this unsteady flow is given by

$$w = \frac{e^{-it}}{2}\left(e^{-i\theta}\zeta + \frac{e^{i\theta}}{\zeta}\right) - \frac{i\hat{\gamma}e^{-it}}{2\pi}\int_2^\infty e^{iax_0}\ln\left(\frac{\zeta - \zeta_0}{\zeta - 1/\zeta_0}\right)dx_0, \qquad (2.54)$$

where $\zeta(z) = z - 1 + \sqrt{z(z-2)}$ and $\zeta_0 = \zeta(x_0)$. Applying the unsteady Kutta condition then fixes the strength of the shed vorticity,

$$\hat{\gamma} = \frac{2\pi\sin\theta}{\int_2^\infty e^{iax_0}\left(\frac{x_0}{x_0-2}\right)^{\frac{1}{2}}dx_0}. \qquad (2.55)$$

For matching with the local solution (2.50), the small-x expansion of the velocity on the airfoil surface is required. We find

$$u(x,0\pm) \sim \left\{\pm\frac{\sin\theta}{2^{\frac{1}{2}}}(1 + J(a))\,x^{-\frac{1}{2}} + \cos\theta + O(x^{\frac{1}{2}})\right\}e^{-it} \qquad \text{as} \quad x \to 0, \qquad (2.56)$$

where $J(a)$ represents the effect of the shed vorticity,

$$J(a) = -\frac{\int_2^\infty e^{iax_0}\left(\frac{x_0-2}{x_0}\right)^{\frac{1}{2}}dx_0}{\int_2^\infty e^{iax_0}\left(\frac{x_0}{x_0-2}\right)^{\frac{1}{2}}dx_0} = O\left(\frac{1}{a}\right), \qquad \text{as} \quad a \to \infty. \qquad (2.57)$$

Thus for the high reduced aerodynamic frequencies of interest in the present study, the effect of shed vorticity on the unsteady flow in the vicinity of the leading edge is smaller than the contribution due to the non-circulatory component, by a factor of $O(1/a)$. Matching with the large ξ limit of the local leading-edge solution (2.50) then gives

$$\kappa_s = \cos\theta, \qquad \kappa_a = a^{\frac{1}{2}}\sin\theta. \qquad (2.58)$$

The symmetric and anti-symmetric components of the local flow past the leading edge are seen to be in phase, owing to the incompressible nature of the unsteady interaction. Except for values of θ near 0 and π, the slip velocity near the leading edge is dominated by the anti-symmetric component of (2.50), which reaches a peak value $(b/r_n)^{1/2}\sin\theta$ at the nose of the airfoil. Note also that, in this limit, the flow about the nose (and hence the Receptivity Coefficient) is the same for an airfoil with sharp trailing edge as for a body with a rounded trailing edge.

18

Next consider the opposite limiting case, $k \gg 1$. The acoustic wavelength is then short compared to the airfoil chord, and the interaction of the acoustic wave with the leading edge can be analyzed by taking the airfoil chord to be semi-infinite. As in the first case, on the scale of the acoustic wavelength, the airfoil appears at leading order as a zero-thickness plate and the problem reduces to the classical Sommerfeld diffraction problem (Noble, 1958). The velocity potential for the unsteady flow is given by

$$\phi(x,y) = \left\{ -\frac{i}{k}e^{ik(x\cos\theta + y\sin\theta)} - \sin\tfrac{1}{2}\theta\frac{sgn(y)}{\pi(2k)^{\frac{1}{2}}} \int_{-\infty}^{\infty} \frac{\exp(-(\lambda^2 - k^2)^{\frac{1}{2}}|y| - i\lambda x)}{(\lambda + k\cos\theta)(\lambda + k)^{\frac{1}{2}}}d\lambda \right\} e^{-it},$$

(2.59)

which leads to a slip velocity

$$u(x,0\pm) = \left\{ \cos\theta e^{ik\cos\theta}(1 \mp \mathrm{erf}\Phi) \pm \sin\tfrac{1}{2}\theta\frac{2^{\frac{1}{2}}e^{\frac{1}{4}i\pi}}{(\pi k)^{\frac{1}{2}}}x^{-\frac{1}{2}} \right\} e^{-it},$$

(2.60)

where $\Phi = e^{-\frac{1}{4}i\pi}(2kx)^{\frac{1}{2}}\sin\tfrac{1}{2}\theta$. Hence, as $x \to 0$,

$$u(x,0\pm) \sim \left\{ \pm \sin\tfrac{1}{2}\theta\frac{2^{\frac{1}{2}}e^{-\frac{1}{4}i\pi}}{(\pi k)^{\frac{1}{2}}}x^{-\frac{1}{2}} + \cos\theta + O(x^{\frac{1}{2}}) \right\} e^{-it}.$$

(2.61)

Matching the slip velocity on the upper surface to the local solution in the vicinity of the leading edge, then gives

$$\kappa_s = \cos\theta, \qquad \kappa_a = \frac{2e^{-\frac{1}{4}i\pi}}{(\pi M_e)^{\frac{1}{2}}}\sin(\tfrac{1}{2}\theta),$$

(2.62)

where $M_e = U_e/c$ is the Mach number of the mean flow, which has been assumed small. The anti-symmetric component of the local flow past the leading edge lags the incident field (and the symmetric component) by a phase angle $\pi/4$, owing to the influence of compressibility. The anti-symmetric component again dominates the symmetric component, except for values of θ near zero. However, the dependence on the incidence angle θ is fundamentally different than for the case of small k. The anti-symmetric component of the slip velocity has a peak value $2e^{i\pi/4}(c/\pi\omega r_n)^{\frac{1}{2}}\sin\tfrac{1}{2}\theta$ at the nose, a result that depends only on the compressibility of the fluid and not on the airfoil semi-chord b.

In the next section, the symmetric and anti-symmetric components, $C_s(S)$ and $C_a(S)$, of the Receptivity Coefficient are calculated, and sample results are presented illustrating the dependence of the Receptivity Coefficient $C_1(S)$ on the incidence angle θ of the acoustic wave in the limits $k \ll 1$ and $k \gg 1$.

2.5   Numerical Results

In §2.3, we utilized asymptotic methods to obtain the non-Blasius generalizations of the Lam-Rott asymptotic eigenfunctions, the first of which is the precursor of the Tollmien-Schlichting wave. The asymptotic analysis determines the form of these eigenfunctions, but not their coefficients C_i. It appears that the Receptivity Coefficient C_1 for a particular free-stream disturbance can be determined only by numerically solving the LUBLE over the full range of ξ and examining the behavior for large ξ.

19
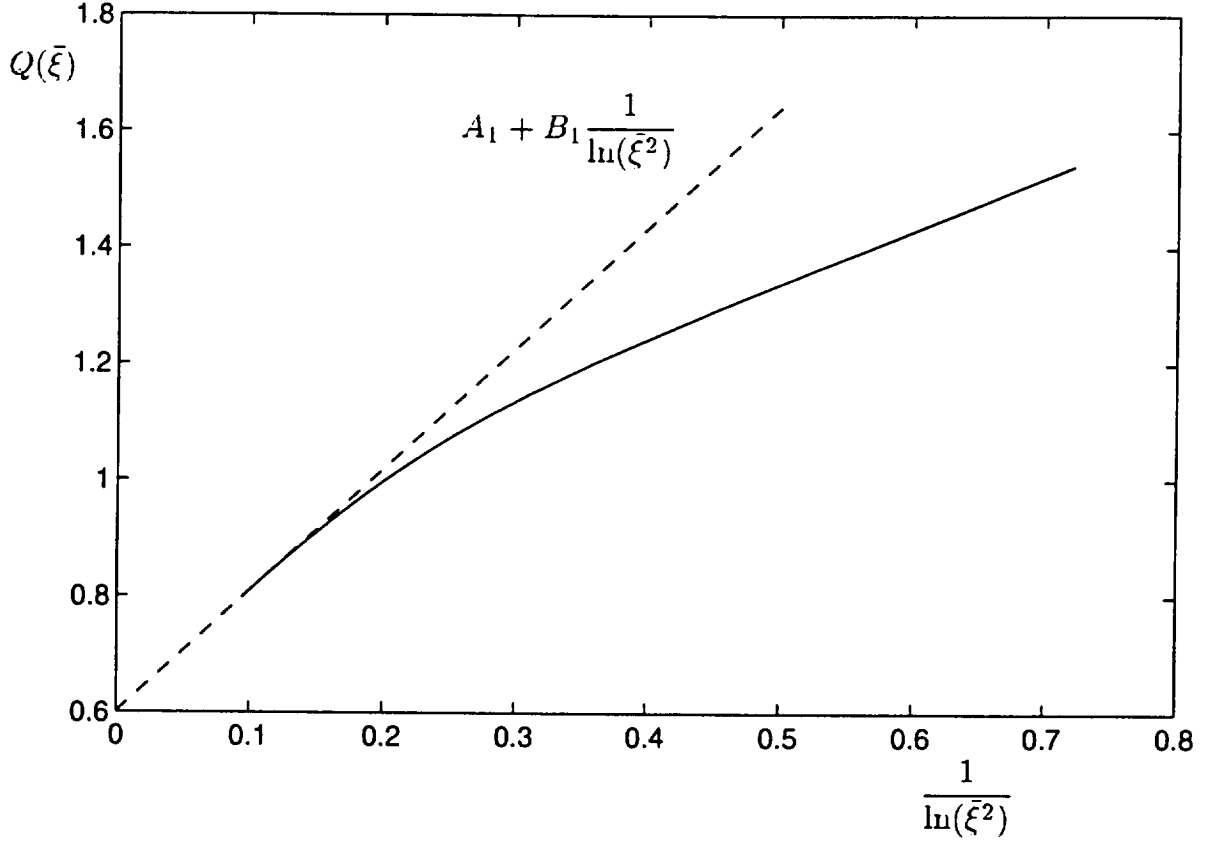
Figure 2.3: Plot of $Q(\bar\xi) = (\ln\bar\xi^2)^{-1}\bar\xi^2([\phi'' - F'']/F'')_{\eta=0}$ against $(\ln\bar\xi^2)^{-1}$. Comparison with the large $\bar\xi$ asymptotic form, (2.23) yields $B_1 \approx 2.08$.

In contrast to the flat-plate studies of previous authors, where the mean flow is known throughout, in the present study the mean flow, governed by (2.19), must be computed as well as the unsteady disturbance, governed by (2.21). The initial conditions at $\xi = 0$, which correspond to the steady Hiemenz flow and its quasi-steady linear perturbation, take the form of ODEs in η, which were solved using a fourth-order Runge-Kutta method. The solution was then obtained by marching downstream using a Keller Box scheme (Keller & Cebeci, 1970) for both the mean flow, given by a nonlinear PDE (2.19), and the linearized disturbance equations for symmetric and anti-symmetric components, (2.53). From the asymptotic form of the eigensolutions, it is clear that the growth or decay of the disturbance is very sensitive to the mean flow. For this reason, the departure of the mean flow away from the Blasius solution was calculated rather than the mean flow directly. The value of the unknown coefficient B_1 in (2.23) can then be extracted from the wall shear. From the asymptotic expansion for the mean flow close to the wall (2.25),

$$\left(\frac{\bar\xi^2[\phi - F]_{\eta\eta}}{(\ln\bar\xi^2)F_{\eta\eta}}\right)_{\eta=0} \sim A_1 + \frac{B_1}{\ln\bar\xi^2} + O(\bar\xi^{-1.774}(\ln\bar\xi)^{-1}). \tag{2.63}$$

From figure 2.3, where the above quantity is plotted for real $\bar\xi$, comparison of the numerical result with this asymptotic form gives $B_1 \approx 2.08$. This is somewhat higher than the value suggested by Van Dyke (1964b), who estimated $B_1 \approx 1.6 - 1.9$ based on

20

coarse numerical results and on numerical patching of the asymptotic series valid near the nose to the series valid far downstream. The computations undertaken in the present work extend to much higher values of $\bar{\xi}$, allowing much more accurate extrapolation to fix B_1. In addition, the magnitude of the next term in the asymptotic series can be estimated from figure 2.3. By considering the magnitude of the correction term at $\bar{\xi}^2 = 30$, the coefficient of the next term in expansion (2.63) is estimated to be approximately 10, which probably explains the under-estimation of Van Dyke.

We turn now to the solution for the disturbance. Since the real part of $T(\xi)$ is negative, the first Lam-Rott eigensolution becomes exponentially small far downstream, compared to the Stokes wave. Moreover, since the eigenvalues are inversely ordered, the first eigensolution is also exponentially small compared to all the other eigensolutions. Thus, it is very difficult to extract the coefficient of the eigensolution by *direct* numerical solution of the LUBLE. A way round this difficulty is to move the integration off the real line into the complex ξ-plane in such a way that the eigensolution will *grow* exponentially (Goldstein *et al*, 1983). This will occur if the streamwise variable ξ is chosen such that $-5\pi/12 < \arg \xi < -\pi/12$. The inverse ordering of the eigensolutions is also rectified by this process, the first eigenfunction becoming exponentially dominant for $|\xi| \gg 1$. 'Peeling off' the exponentially growing part of the first eigensolution, that is solving for $f = \psi e^{-T_1^{(0)}}$ rather than ψ, allows the numerical solution to be continued much further downstream while retaining accuracy (Heinrich & Kerschen, 1989).

There are essentially two ways of obtaining the Receptivity Coefficient C_1, one based on the wall shear and the other based on the oscillating boundary-layer thickness. The latter method was used by Goldstein *et al* (1983) and Heinrich & Kerschen (1989) for the flat-plate analysis. In the present work the two methods gave virtually identical results, small differences only arising due to the difference in large-ξ extrapolation procedure in the two cases. Using the wall shear as the basis for comparison, we define

$$C(S,\xi) = \frac{f''_{\text{Num}}(\eta = 0)}{f''_0}, \qquad (2.64)$$

where $f''_0 = 0.4356(1 + i)\,(\xi^2/2)^{n+1}$. Since the argument of ξ was chosen so that the first eigensolution dominates other components of the solution, $f \sim C_1 \psi_1 e^{-T_1^{(0)}(\xi)}$, and hence

$$C \sim C_1 \left[1 + b_1 S^{1.887} \frac{1}{\xi^{0.774}} + b_2 S^2 \frac{\ln^2(\xi^2/S)}{\xi} + b_3 S^2 \frac{\ln(\xi^2/S)}{\xi} + b_4 S^2 \frac{1}{\xi} + \dots \right], \qquad (2.65)$$

as $\xi \to \infty$. Thus in principle, C_1 can be extrapolated by plotting the numerically obtained value of $C(S,\xi)$ against $\xi^{-0.774}$. However, this method has serious limitations as far as obtaining highly accurate estimates for C_1. Until ξ is extremely large, the sizes of the next three terms in the expansion are very close to that of the leading order correction, with the relative magnitudes depending also on S. In addition, the analysis of the base flow suggests that b_1 is quite large, so for larger values of S the exponential term cannot be expanded out until ξ is very large. Due to these difficulties, the Receptivity Coefficient for non-zero S cannot be calculated to the same accuracy as for the flat plate, the inaccuracy increasing as S increases. In our calculations, we usually chose $\arg \xi = -\pi/4$ which ensures that the rate of growth of the first Lam-Rott eigensolution is maximized. In addition, for this angle any error in the numerically determined value of B_1 enters only the phase of C_1 and not the magnitude. For some values of S, the solution for

arg $\xi = -\pi/3$ was also obtained and the extrapolated value of C_1 was virtually identical, further verifying the numerical work as well as the functional form of the eigensolution. The solution was integrated up to $|\xi| = 15$, except for the larger values of S where it was continued up to $|\xi| = 20$ in an attempt to improve the extrapolation. Computation to larger values of ξ becomes progressively more expensive due to the presence of the viscous wall layer, the relative thickness of which decreases downstream.

In figure 2.4, the numerically obtained value of the Receptivity Coefficient for acoustic waves propagating parallel to the airfoil chord, C_s, is plotted for several values of S. In figure 2.4a it is seen that the magnitude of the Receptivity Coefficient increases slightly for very small S, but decreases rapidly as the nose radius increases further. For $S = 0.3$, the receptivity is reduced to approximately 15% of that for a flat plate. The decay of $|C_s|$ appears to be exponential in S, though this has not been verified analytically. For $S \le 0.1$, the results for $|C_s|$ are estimated as accurate to 2%, while the accuracy for $S = 0.3$ is only about 10%, due to the difficulties discussed above. However, the large relative uncertainty for the latter case is of little practical importance, since the receptivity is so low by this stage. The small increase in the parallel-wave receptivity seen for very small values of S is in agreement with small-S asymptotic theory which will be reported elsewhere (Hammerton & Kerschen 1996a). Figure 2.4b shows the change in the phase of the Receptivity Coefficient as S increases. The increase in $\arg(C_s)$ corresponds to a lag in phase of the instability wave.

As we have already noted, computation must be carried out to large values of ξ for accurate determination of the Receptivity Coefficient, since the eigensolution tends to its asymptotic limit slowly. However, the ratio of Receptivity Coefficients for different free-stream disturbances can be evaluated accurately at only moderately large values of ξ, since the same asymptotic behavior of the eigensolution arises whatever the form of the free-stream disturbance. In the present chapter, we consider only the effect of acoustic waves at oblique angles. In figure 2.5, the receptivity due to the symmetric and anti-symmetric components of the free-stream disturbance is compared for different nose radii. We define $\Lambda = C_a/C_s$, where C_a is the Receptivity Coefficient related to the anti-symmetric component of (2.50). In figure 2.5a, $|\Lambda|$ is plotted as a function of S. We see that $|C_a|$ is larger than $|C_s|$ by approximately a factor of six in the flat-plate limit $S \to 0$, where the anti-symmetric component of the slip velocity has a square-root singularity at the leading edge. The value of $|\Lambda|$ decreases rapidly as a finite nose radius is introduced, relieving the singularity at the leading edge. Thus, the behavior of C_a for very small S is quite different from that of C_s, where a small rise in magnitude was seen. The sharp change in Λ for small S suggests the appearance of singular behavior in the small-S expansion, in contrast to the behavior seen in figure 2.4 for the parallel-wave case. Beyond $S = 0.05$ the decline in $|\Lambda|$ becomes more gradual, the value of $|\Lambda|$ remaining above 2.5 right out to $S = 0.3$. For all values of S examined, the anti-symmetric component of the slip velocity was found to be more effective than the symmetric component in generating a Tollmien-Schlichting wave.

The phase difference between the C_a and C_s is plotted in figure 2.5b. It is interesting to note that as $S \to 0$, arg $\Lambda \to \pi/4$. For reasons given above, Λ can be calculated very accurately, and this result is true to an accuracy better than 0.1%. However, the fundamental reason for this result is not clear. Arg(Λ) initially drops rapidly as a finite nose radius is introduced, then remains roughly constant from $S = 0.05$ out to $S = 0.3$. The positive values of arg(Λ) correspond to a phase lag for the contribution from the
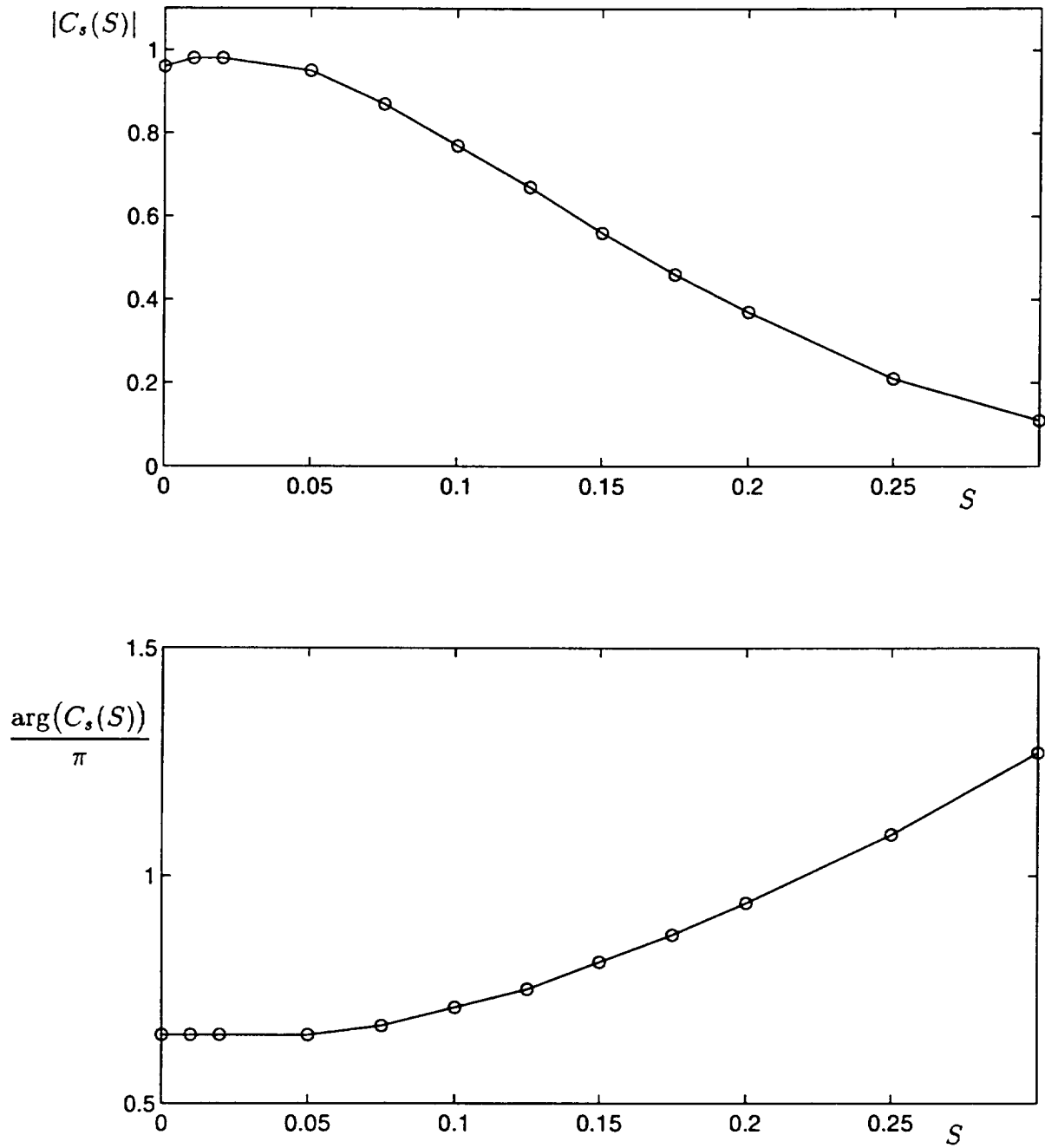
Figure 2.4: Variation of the receptivity coefficient as a function of Strouhal number, S, for an acoustic wave in the free stream propagating parallel to the body axis: (a) the amplitude of the receptivity coefficient $|C_s(S)|$; (b) the phase of the receptivity coefficient $\arg(C_s)/\pi$.
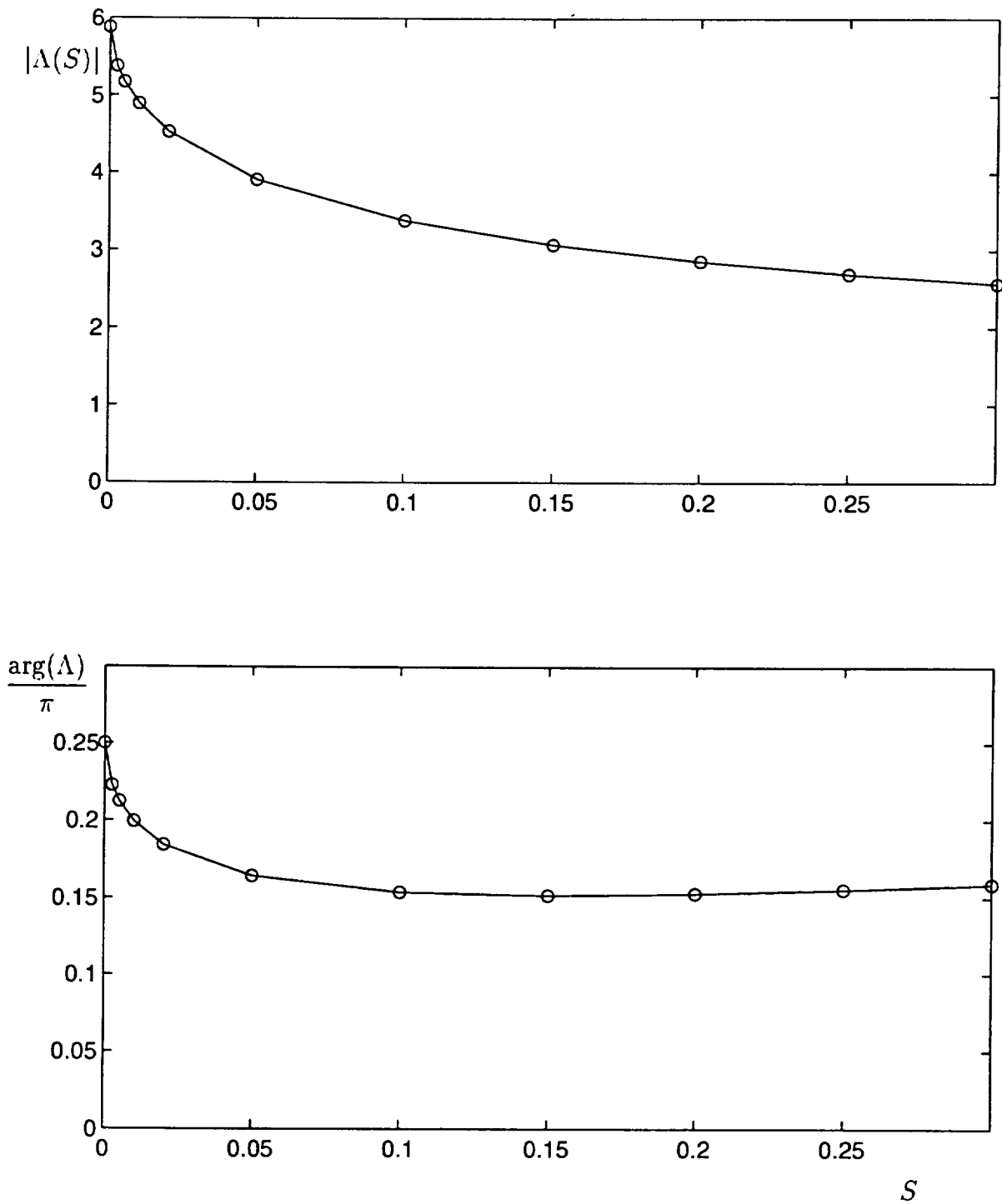
Figure 2.5: Comparison of the relative receptivity due to symmetric and asymmetric components of an oblique acoustic wave, $\Lambda = C_a/C_s$: (a) the magnitude of the relative receptivity, $|\Lambda|$; (b) the phase, $\arg(\Lambda)$.
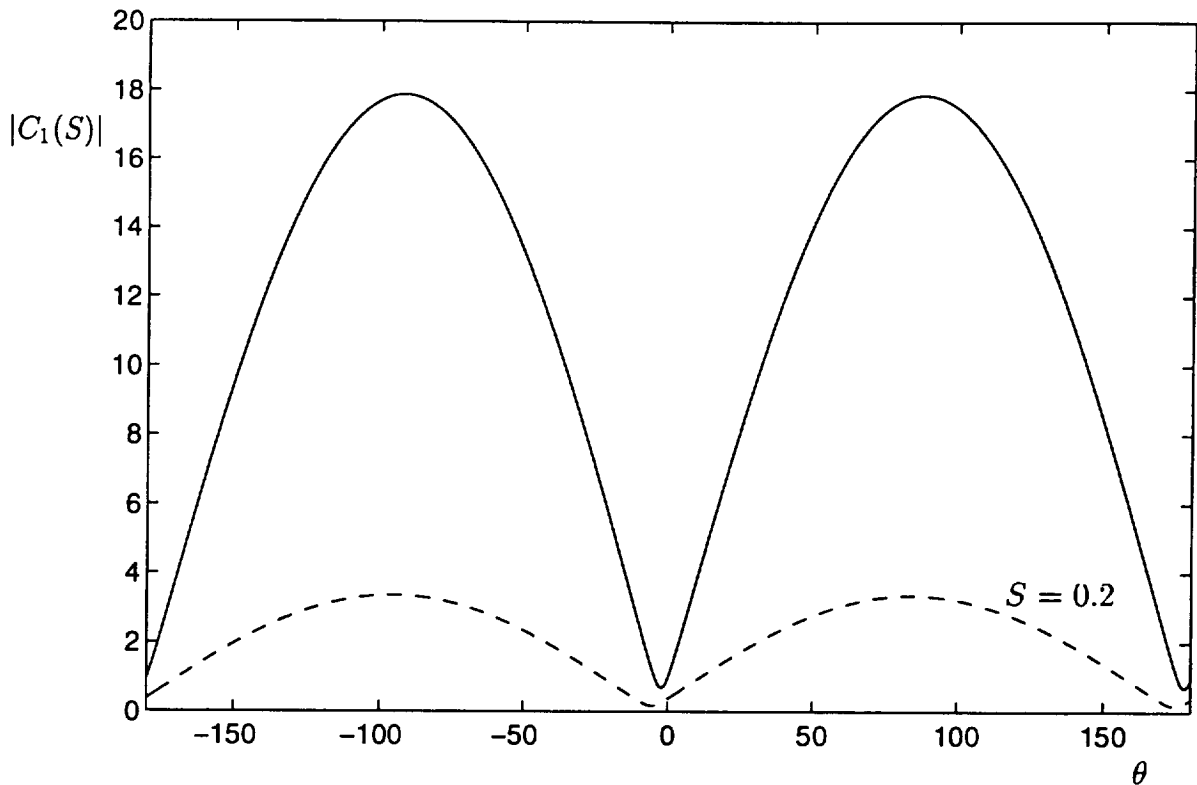
Figure 2.6: Variation of $|C_1|$ with acoustic incidence angle θ, for $k \ll 1$ and non-dimensional airfoil chord length $a = 10$. The solid line is for $S = 0.0$, the dotted line $S = 0.2$.

anti-symmetric component of slip velocity, relative to the contribution from the symmetric component. This phase lag may be related to the fact that the anti-symmetric component of the slip velocity takes on its largest values near the nose, while the symmetric component takes on its largest value farther downstream. The concentration of the anti-symmetric component near the leading edge is particularly pronounced in the limit $S \to 0$, where $\arg(\Lambda)$ takes on its largest value, the slip velocity being singular at $\xi = 0$ in this case.

The variation of the total Receptivity Coefficient C_1 with acoustic wave incidence angle is illustrated for the case $k \ll 1$ in figure 2.6. A representative aerodynamic reduced frequency, $a = 10$, has been chosen, and results are plotted for two nose radii, $S = 0$ and 0.2. The receptivity for the flat-plate case ($S = 0$) is dominated by the contribution from the anti-symmetric component, causing the shape of the plot for $|C_1|$ to be quite close to $\sin\theta$, except in the vicinity of $\theta = 0^o$ and 180° where the level is determined by the symmetric component. The case $a = 10$, $S = 0.2$ corresponds to a typical airfoil design. The overall receptivity level for $S = 0.2$ is smaller than for the flat plate, due to decreases in both $|C_s|$ and $|C_a|$. Since the finite nose radius causes a larger decrease in C_s than C_a, the influence of the symmetric component of the free-stream disturbance is somewhat larger in this case. The peak receptivity for $S = 0.2$ is roughly one-fifth that for the flat-plate.

The variation of the total Receptivity Coefficient C_1 with incidence angle is illustrated
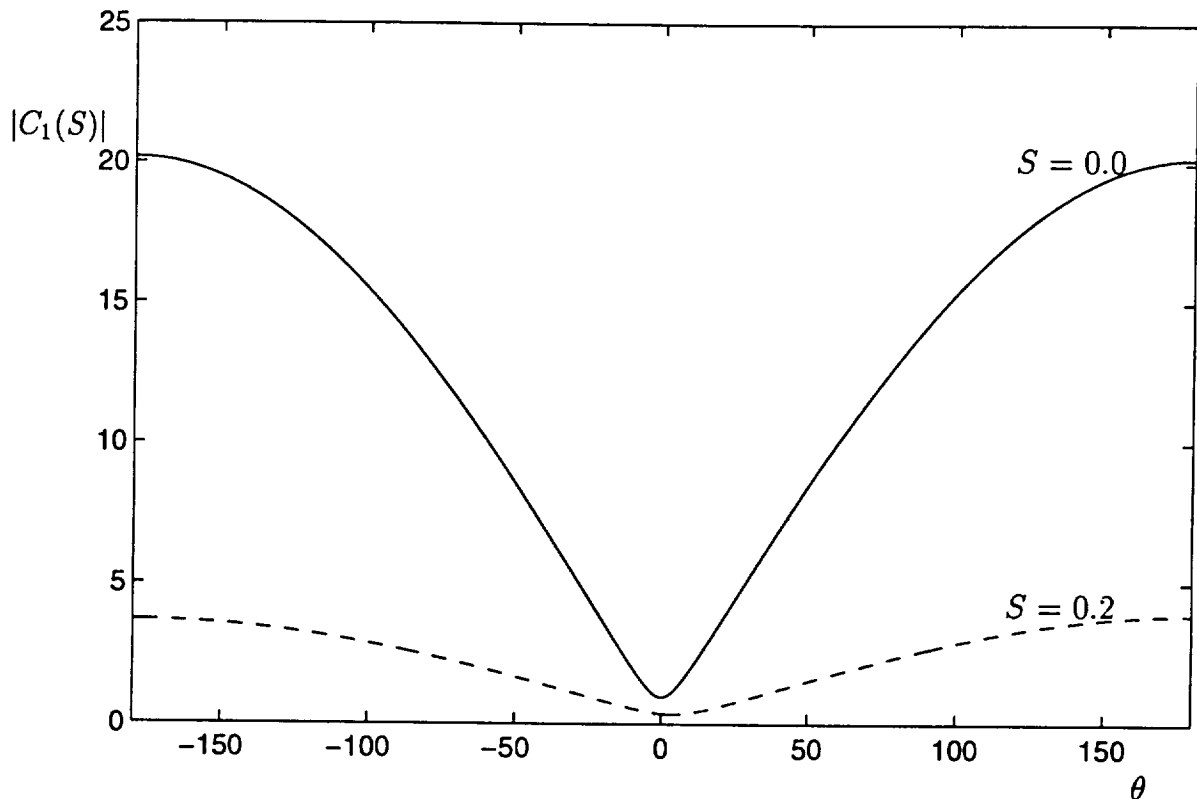
Figure 2.7: Variation of $|C_1|$ with acoustic incidence angle θ, for $k \gg 1$ and $M = 0.1$, and the same values of S plotted in figure 2.6.

for the case $k \gg 1$ in figure 2.7. A representative Mach number $M_e = 0.1$, has been chosen. The dependence of the receptivity level on acoustic wave incidence angle is very different from the case $k \ll 1$ illustrated in figure 2.6. The flat-plate result is again dominated by the contribution from the anti-symmetric component of the free-stream disturbance, but the plot-shape resembles $\sin \frac{1}{2}\theta$, except near $\theta = 0^0$ where the symmetric component determines the level. As before, for $S = 0.2$ the overall receptivity level is decreased, but the relative contribution from the symmetric component of the disturbance is somewhat larger.

2.6 Conclusion

Boundary layer transition is influenced both by the stability properties of the boundary layer, and by the characteristics of the free-stream disturbances and the receptivity of the boundary layer to these disturbances. The present work has examined the influence on leading-edge receptivity of the nose radius of an uncambered airfoil symmetric mean flow, in the low Mach number limit.

Leading-edge receptivity involves a gradual evolution of the boundary-layer disturbances with downstream distance, eventually leading to a growing Tollmien-Schlichting wave. The Receptivity Coefficient is essentially the amplitude of the asymptotic eigenfunction which is the precursor of the Tollmien-Schlichting wave. It is the Receptivity

Coefficient which contains all the relevant information about the free-stream disturbance. The decay rate of the asymptotic eigenfunction, like that of the Tollmien-Schlichting wave, is influenced only by the mean flow. One of the most important properties is the pressure gradient parameter, β. For symmetric flow past a parabola,

$$\beta = \frac{S}{\xi^2 + S},$$ (2.66)

where S is the Strouhal number, $S = \omega r_n/U_e$. Thus, the pressure gradient is everywhere favorable, decreasing monotonically from its maximum value at the stagnation point and approaching zero far downstream. Well downstream of the nose, the favorable pressure gradient has a stabilizing influence on the boundary layer, leading to increased damping of the Tollmien-Schlichting waves and of the precursor disturbances. In addition, the stronger pressure gradient close to the nose has an effect on the Receptivity Coefficient. As the nose radius of the body is increased (*i.e.* S increased), the strongly favorable pressure gradient near the nose extends over a larger number of disturbance wavelengths, and this additional stabilizing influence is likely to result in a decrease in the Receptivity Coefficient. Numerical calculations show that the symmetric component C_s of the Receptivity Coefficient decreases rapidly with increasing S, dropping to approximately 12% of the flat-plate value when $S = 0.3$. The anti-symmetric component C_a decreases even more rapidly, dropping to 5% of flat-plate value when $S = 0.3$. The total Receptivity Coefficient C_1 is much larger for oblique acoustic waves than for parallel acoustic waves, since the coefficient $\kappa_a(\theta)$ that multiplies the anti-symmetric component C_a is large compared to the coefficient $\kappa_s(\theta)$ that multiplies the anti-symmetric component C_s.

While the detailed asymptotic analysis depends on the exact geometry of the leading edge, the rapid decrease in receptivity with increasing nose radius should also be valid for other streamlined bodies. However, symmetric mean flows past leading edges less streamlined often involve regions of adverse as well as favorable pressure gradient close to the nose. For such bodies, it is possible that an increase in leading edge thickness could lead to an increase in the Receptivity Coefficient. For an airfoil at an angle of attack, both favorable and adverse pressure gradients exist in the neighborhood of the nose. Analysis of the receptivity in this case will be presented in chapter 3.

Comparing the asymptotic analysis presented here with numerical and experimental results is difficult. Numerical work by Murdock (1981) for a parabola in a flow with a parallel acoustic wave also showed a decrease in receptivity as the nose radius was increased. The computations of Lin *et al.* (1992) were for parallel acoustic waves incident on half-ellipse leading edges connected to a flat plate and for super-ellipse leading edges (which avoid the discontinuity in curvature), geometries chosen to match the experiments of Saric *et al.* (1994). For both these geometries there are regions of adverse pressure gradient near the leading edge, as well as the possibility of additional localized receptivity mechanisms (Goldstein, 1985); hence no direct comparisons can be made with the present results. In addition, the receptivity level 'seen' in experiments and full Navier-Stokes calculations is a combination of the receptivity process described in the current chapter, and the stability characteristics farther downstream. For the flat-plate, Goldstein (1983) provided the asymptotic analysis of the triple-deck region and thus (in theory) could calculate the disturbance amplitude at the lower branch. Reproducing such an analysis for a general airfoil surface would provide little additional physical insight concerning the receptivity process. By restricting attention to the region in which forcing by the

free-stream disturbance occurs, the process of receptivity is isolated from the instability phenomena that occur farther downstream. For a global picture of the transition process, the current analysis provides an upstream boundary condition for linear stability analyses.

Chapter 3

Low frequency theory for a leading edge with no aerodynamic loading

3.1　Introduction

The receptivity process through which free-stream disturbances generate instability waves in boundary layers generally comes about through non-parallel mean flow effects, which may arise either in the leading-edge region, or in a localized region farther downstream in the boundary layer (Goldstein & Hultgren 1989; Kerschen 1990).

In Goldstein (1983), an asymptotic analysis was developed for leading-edge receptivity on a semi-infinite zero-thickness plate. Leading-edge receptivity coefficients for various free-stream disturbances were calculated by Goldstein, Sockol & Sanz (1983) and Heinrich & Kerschen (1989). However, aerodynamic bodies designed for subsonic flow generally have finite thickness distributions with a parabolic leading edge. In chapter 2, the influence of the thickness of a body was examined. The situation considered was a thin, symmetric airfoil of chord $2b$ at zero angle-of-attack in a uniform flow of speed U. A plane acoustic wave of frequency ω, propagating at an angle θ with respect to the airfoil chord, was assumed to be incident on the airfoil as illustrated in figure 3.1. A high Reynolds number asymptotic analysis ($\epsilon^6 = \nu\omega/U^2$; $\epsilon \ll 1$) was formulated for an incompressible, two-dimensional flow. The nose radius of the leading edge, r_n, enters through a Strouhal number,

$$S = \frac{\omega r_n}{U} \tag{3.1}$$

which is the ratio of the nose radius and the hydrodynamic length scale, U/ω.

When $S = O(1)$, two streamwise regions enter the analysis, one region where the distance downstream is $O(U/\omega)$ and the disturbance is governed by the linearized unsteady boundary layer equation (LUBLE), and a second region at distances $O(\epsilon^{-2}U/\omega)$ where the disturbance is governed by the triple-deck structure, corresponding to the asymptotic form of the Orr–Sommerfeld equation (OSE) in the vicinity of the lower branch. In the LUBLE region, the inviscid pressure field and slip velocity induced by the free-stream disturbance drives the unsteady motion in the boundary layer. Far downstream in the LUBLE region, the solution consists of a generalized Stokes wave, and a set of asymptotic eigensolutions. The wavelengths of these eigenfunctions shorten progressively with distance downstream. Eventually, the self-induced pressure field associated with the displacement thickness of each asymptotic eigenfunction becomes significant, and the
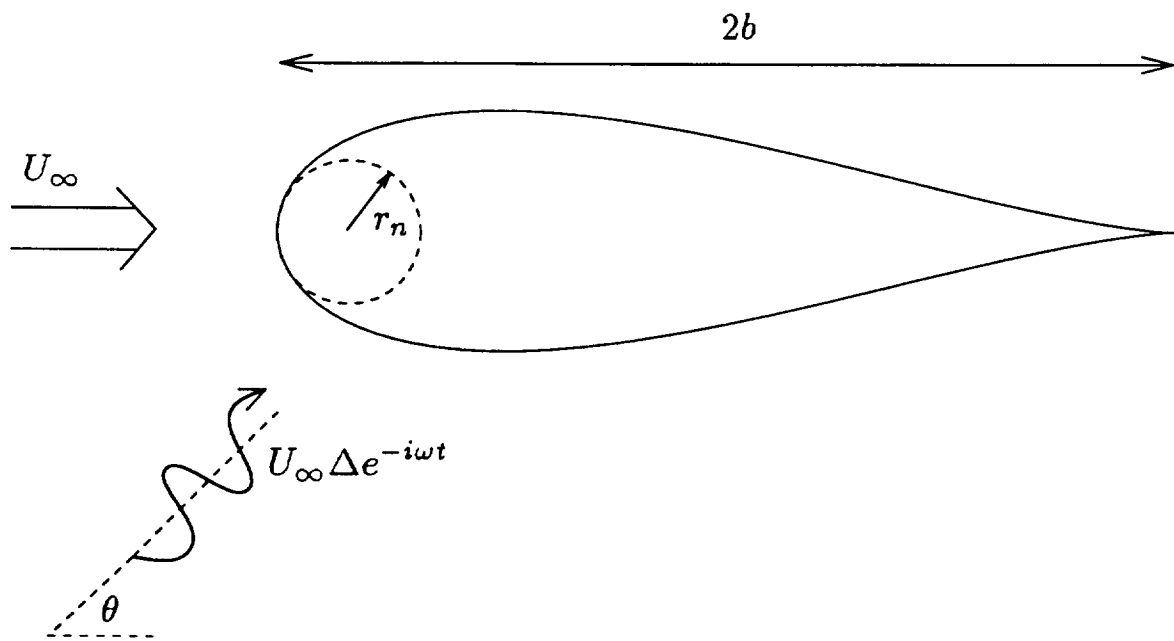
Figure 3.1: An illustration of the physical situation of interest: a thin, symmetric airfoil of chord $2b$ is at zero angle-of-attack in a uniform flow of speed U, with a plane acoustic wave incident at an angle θ with respect to the airfoil chord.

triple-deck structure replaces the LUBLE as the correct asymptotic approximation to the Navier–Stokes equation. It can be shown that the first asymptotic eigenfunction of the LUBLE matches on to the Tollmien–Schlichting wave solution of this triple-deck region. Thus, the form of the free-stream disturbance and the geometry close to the nose influence the amplitude of the Tollmien–Schlichting wave only through the coefficient C_1 of the first asymptotic eigenfunction. Therefore, we call C_1 the 'receptivity coefficient'. The asymptotic analysis far downstream in the LUBLE region determined the form of the eigenfunctions, but not their coefficients C_i. These coefficients can be found only through a full solution of the LUBLE, which must be determined by numerical methods.

Theory for $S = O(1)$ was developed in chapter 2, where associated numerical results were also presented. These results showed that the receptivity associated with a symmetric free-stream disturbance increases slightly with S, for small S (figure 2.4a), but the receptivity associated with a free-stream disturbance that is anti-symmetric about the leading edge decreases sharply with S (figure 2.5a). In the present chapter, a small-S asymptotic theory is developed. In this limit, the streamwise development of the boundary layer can be divided into three regimes. In the nose region, where the distance downstream is $O(r_n)$, the unsteady motion in the boundary layer is quasi-steady at leading order. In the LUBLE region, where the downstream distance is $O(U/\omega)$, the unsteady terms enter at leading order in the disturbance equations, but the mean pressure gradient is small so that the mean boundary layer flow approaches the flat-plate solution. In the OSE region further still downstream, a triple-deck structure arises as before. In the small-S asymptotic analysis presented in this chapter, we focus on the nose and LUBLE regions. The subsequent asymptotic matching to the OSE region follows that discussed in chapter 2. Our analysis involves two small parameters, S and ϵ. Formally, we take $\epsilon \to 0$ and then consider the small-S limit, obtaining correction terms of $O(S^{1/2}, S)$. We require the boundary-layer approximation to be valid in the nose region $x_d = O(r_n)$, which is true if the Reynolds number based on nose radius is large,

$$\frac{U r_n}{\nu} = \frac{S}{\epsilon^6} \gg 1. \tag{3.2}$$

This condition is also equivalent to the requirement that the perturbation in the receptivity coefficient due to finite Reynolds number is smaller than that due to geometric effects. Thus the asymptotic theory is more relevant to the limit $\omega \to 0$ rather than $r_n \to 0$.

In §3.2, the equations governing the mean flow and the time dependent perturbation in the boundary layer are obtained. The small-S asymptotic structure of the unsteady flow in the boundary layer, produced by the symmetric and anti-symmetric components of the free-stream disturbance, is analyzed in §§3.3 and 3.4 respectively. In §3.5, numerical solutions of the asymptotic equations are presented, and the resulting asymptotic expressions for the receptivity coefficient are compared with the numerical results of chapter 2. Finally in §3.6, the results are summarized and brief comparisons with experiments are made.

3.2 Formulation

Full details of the derivation of the equations governing the boundary layer flow are given in chapter 2, together with interpretation of the evolution of the unsteady disturbances

that eventually lead to instability. Here we provide only the key equations necessary to illustrate the small Strouhal number limit which is the subject of the present chapter.

The streamfunction Ψ in the boundary layer, non-dimensionalized by the quantity $U\nu^{\frac{1}{2}}/\omega^{\frac{1}{2}}$, is expressed in the form

$$\Psi = \xi\phi + \psi e^{-it} \tag{3.3}$$

where the unsteady component ψ is assumed small compared to the mean flow component $\xi\phi$. We use parabolic coordinates (ξ, η) defined by

$$x_d + iy_d = \frac{1}{2}\frac{U}{\omega}\left(\left[\xi + i(S^{1/2} + \epsilon^3\eta)\right]^2 + S\right), \tag{3.4}$$

where x_d, y_d are (dimensional) Cartesian coordinates centered on the airfoil leading edge. The parabolic coordinate ξ along the airfoil surface has been non-dimensionalized by the square root of the disturbance length U/ω. For the parabolic coordinate η in the normal direction, the origin has been shifted to the airfoil surface, and the additional factor ϵ^3 in (3.4) corresponds to non-dimensionalized by the quantity $(\nu/U)^{\frac{1}{2}}$. Thus η corresponds to the conventional normal coordinate for the mean boundary layer.

3.2.1 Steady flow

The steady boundary-layer flow is most naturally expressed in terms of a streamwise variable scaled on the nose radius,

$$\bar{\xi} = \xi/S^{1/2}. \tag{3.5}$$

The function $\phi(\bar{\xi}, \eta)$ describing the steady boundary-layer flow then satisfies the differential equation

$$\phi_{\eta\eta\eta} + \phi_{\eta\eta}\phi + \bar{\xi}(\phi_{\eta\eta}\phi_{\bar{\xi}} - \phi_{\eta}\phi_{\eta\bar{\xi}}) - \frac{1}{1+\bar{\xi}^2}(\phi_{\eta}^2 - 1) = 0, \tag{3.6}$$

with boundary conditions

$$\phi = \phi_{\eta} = 0 \quad \text{at} \quad \eta = 0 \quad \text{and} \quad \phi_{\eta} \to 1 \quad \text{exponentially as} \quad \eta \to \infty. \tag{3.7}$$

For large $\bar{\xi}$, ϕ takes the form (Van Dyke, 1964)

$$\phi(\bar{\xi}, \eta) \sim F(\eta) + \overline{G}_1(\eta)\frac{\ln\bar{\xi}^2}{\bar{\xi}^2} + \overline{G}_2(\eta)\frac{1}{\bar{\xi}^2} + O\left(\frac{1}{\bar{\xi}^{\gamma_2}}\right), \qquad \gamma_2 \approx 3.774, \tag{3.8}$$

where the order of the next higher order term is discussed below. In this expansion, $F(\eta)$ is the Blasius function, and the functions $\overline{G}_i(\eta)$ satisfy homogeneous boundary conditions

$$\overline{G}_i(0) = \overline{G}_i'(0) = 0, \qquad \overline{G}_i' \to 0 \quad \text{exponentially as} \quad \eta \to \infty, \tag{3.9}$$

with governing equations

$$\mathcal{G}_2(\overline{G}_1) = 0, \qquad \mathcal{G}_2(\overline{G}_2) = F'^2 - 1 + 2(F''\overline{G}_1 - F'\overline{G}_1'), \tag{3.10}$$

32

where we define the set of operators $\mathcal{G}_\gamma$ by

$$\mathcal{G}_\gamma(f) \equiv f''' + Ff'' + \gamma F'f' + (1 - \gamma)F''f. \tag{3.11}$$

In the first perturbation term of the large-$\bar{\xi}$ expansion we have $\overline{G}_1 = A_1 G_1$, where

$$G_1 = \eta F'(\eta) - F(\eta), \tag{3.12}$$

which arises as an eigenfunction of $\mathcal{G}_\gamma$ for $\gamma = 2$. The coefficient A_1 remains undetermined at this order. However, the equation for $\overline{G}_2(\eta)$ then takes the form

$$\mathcal{G}_2(\overline{G}_2) = F'^2 - 1 + 2A_1 FF''. \tag{3.13}$$

Since the Blasius function F is the solution to the adjoint of $\mathcal{G}_2$, the value of A_1 is fixed by the solvability condition for $\overline{G}_2(\eta)$ which leads to

$$\int_0^\infty F(F'^2 - 1 + 2A_1 FF'')d\eta = 0, \tag{3.14}$$

and gives $A_1 = 0.60115$.

The equation for $\overline{G}_2(\eta)$ involves the same operator $\mathcal{G}_2$ and hence contains the same eigenfunction. Thus, $\overline{G}_2 = B_1 G_1 + G_2$, where $G_2(\eta)$ satisfies (3.13), with boundary conditions (3.9) and $G_2''(0) = 0$. Since $\bar{\xi}^{-2}G_1$ is an eigensolution of the boundary-layer perturbation equation, the value of the coefficient B_1 appearing in the $O(\bar{\xi}^{-2})$ term can not be determined by the large-ξ analysis and therefore depends on conditions close to the nose of the body. Numerical integration of (3.6) from $\bar{\xi} = 0$ gives $B_1 \approx 2.08$ (chapter 2). For all $\gamma > 0$, $\mathcal{G}_\gamma$ has solutions which decay algebraically as $\eta \to \infty$, but only for certain γ do solutions exist which decay exponentially at infinity. Libby & Fox (1963) give the first 10 eigenvalues. The first such eigenvalue, $\gamma_1 = 2$ has already been discussed. The next eigenvalue, $\gamma_2 \approx 3.774$, leads to the next higher order term in the large-$\bar{\xi}$ expansion (3.8).

3.2.2 Unsteady flow

The time-dependent contribution to the boundary-layer flow satisfies the linearized unsteady boundary layer equation (LUBLE),

$$\left. \begin{aligned} \mathcal{F}(\psi) &= (S + \xi^2)^{1/2}\left[\left(i(S+\xi^2) - \frac{S}{S+\xi^2}\right)u_s - \xi\frac{\partial u_s}{\partial \xi}\right], \\ \mathcal{F}(\psi) &\equiv \psi_{\eta\eta\eta} + [\phi + \xi\phi_\xi]\psi_{\eta\eta} + \left[i(S+\xi^2) - \xi\phi_{\eta\xi} - \frac{S-\xi^2}{S+\xi^2}\phi_\eta\right]\psi_\eta \\ &\quad + \xi(\phi_{\eta\eta}\psi_\xi - \phi_\eta\psi_{\eta\xi}), \end{aligned} \right\} \tag{3.15}$$

with boundary conditions

$$\psi = \psi_\eta = 0 \quad \text{at} \quad \eta = 0 \quad \text{and} \quad \psi_\eta \to (S + \xi^2)^{1/2}\,u_s \quad \text{as} \quad \eta \to \infty. \tag{3.16}$$

Here, $u_s(\xi)$ is the slip velocity induced on the outer edge of the boundary layer by the free-stream disturbance. Note that this equation is written in terms of ξ, the streamwise coordinate scaled on the disturbance length scale U/ω, and hence ϕ must be expressed in terms of ξ.

The development of the solution ψ is described in detail in chapter 2. Far downstream $(\xi \gg 1)$, ψ consists of a particular solution, ψ_p, driven by the local value of the unsteady pressure gradient, together with an infinite set of asymptotic eigensolutions,

$$\psi(\eta, \xi; S) = \psi_p(\eta, \xi; S) + \sum_i C_i(S)\psi_i(\eta, \xi; S). \tag{3.17}$$

The eigensolutions, ψ_i, depend on the geometry of the body far downstream, but are independent of the local free-stream disturbance. In this chapter, where we are concerned with the generation of instability waves in the boundary layer, we consider eigensolutions which are generalized forms of the Lam & Rott (1960) eigenfunctions. Another set of eigensolutions could also be calculated, corresponding to generalizations of the functions derived by Brown & Stewartson (1973) for a flat plate. The role of these two sets of eigensolutions is discussed in chapter 2. The coefficients C_i multiplying the asymptotic eigenfunctions are determined entirely by conditions close to the leading edge $(\xi = O(1))$. One of these eigensolutions, which we label ψ_1, matches on to the Tollmien–Schlichting wave in the Orr–Sommerfeld region farther downstream, where $\xi = O(\epsilon^{-1})$. Thus, it is only through the coefficient C_1 that the unsteady disturbances in the free stream influence the amplitude of the Tollmien–Schlichting wave. Our primary interest is in the relationship between the free-stream disturbances and the amplitude of the Tollmien–Schlichting wave, as a function of Strouhal number S. Thus, we focus on the asymptotic eigensolutions of the LUBLE, which develop a two-layer structure for $\xi \gg 1$. From chapter 2, equations (2.31), (2.48) and (2.49), at the outer edge of the boundary layer $(\eta \to \infty)$, the first asymptotic eigenfunction takes the form

$$\left.\begin{array}{l} \psi_1 \sim \xi \left(\frac{\xi^2}{2}\right)^{\tau_1^{(0)}+S\tau_1^{(1)}} \exp\left(T_1^{(0)}\right) (1 + O(\xi^{-0.774})), \\[2mm] \tau_1^{(0)} = -0.69213, \qquad \tau_1^{(1)} = -1.9878\,\mathrm{i}, \\[2mm] T_1^{(0)}(\xi) = -\lambda\xi^3 \left\{\frac{1}{3} - A_1 S \frac{\ln(\xi^2/S)}{\xi^2} + (2A_1 + \frac{3}{2} - B_1)\frac{S}{\xi^2}\right\} \end{array}\right\} \tag{3.18}$$

where $\lambda = e^{-\frac{1}{4}i\pi}/(\rho_1^{3/2} U_0')$. Here $\rho_1 \approx 1.0187$, the first root of $\mathrm{Ai}'(-\rho) = 0$, and $U_0' \equiv F''(0) \approx 0.4696$. The numerical constants A_1 and B_1 arise from the asymptotic form of the mean boundary-layer flow far downstream, (3.8).

For a low Mach number flow, outside the boundary layer the unsteady flow in the vicinity of the leading edge is incompressible and irrotational. Potential flow theory then shows that this local flow consists of symmetric and antisymmetric components of the form

$$u_s(\xi) = \kappa_s \frac{\xi}{(S + \xi^2)^{1/2}} + \kappa_a \frac{1}{(S + \xi^2)^{1/2}}. \tag{3.19}$$

Here $\xi/(S+\xi^2)^{1/2}$ and $1/(S+\xi^2)^{1/2}$ correspond to purely symmetric and anti-symmetric flow about the leading edge, respectively. The coefficients $\kappa_s(\theta)$ and $\kappa_a(\theta)$ multiplying the symmetric and antisymmetric components are independent of the nose geometry, but depend on the free-stream disturbance, being determined by global features of the unsteady flow. When the unsteady disturbance velocity is parallel to the mean flow, (i.e. $\theta = 0$), the forcing is entirely symmetric and $\kappa_s = 0$. For oblique $(\theta \neq 0)$ disturbances, the unsteady flow will have both symmetric and anti-symmetric components. Calculation of the coefficients κ_s and κ_a for different free-stream disturbances is discussed in §2.4. Writing $\psi = \kappa_s\psi_s + \kappa_a\psi_a$, and substituting into (3.15), it follows that the receptivity

coefficient can be decomposed into contributions from the symmetric and anti-symmetric components of the unsteady outer flow,

$$C_1(S) = \kappa_s \, C_s(S) + \kappa_a \, C_a(S),$$

(3.20)

where C_s and C_a are obtained from the solutions of

$$\mathcal{F}(\psi_s) = \xi \left(\mathrm{i}(S + \xi^2) - \frac{2S}{S + \xi^2} \right),$$

(3.21a)

$$\mathcal{F}(\psi_a) = \mathrm{i}(S + \xi^2) - \frac{S - \xi^2}{S + \xi^2},$$

(3.21b)

respectively. The numerical methods used to obtain values of $C_a(S)$ and $C_s(S)$ for fixed S are described in chapter 2. The remainder of this chapter is concerned with the asymptotic expansions of $C_a(S)$ and $C_s(S)$ as $S \to 0$.

In the nose region, $\bar{\xi} = O(1)$, the mean pressure gradient decreases with distance downstream, and the mean flow approaches the flat-plate limit as $\bar{\xi} \to \infty$. In the small-S limit, the nose-region is quasi-steady at leading order; the linearized boundary layer equations only become fully unsteady when $\xi = O(1)$, i.e. $\bar{\xi} = O(S^{-\frac{1}{2}})$. Thus in the receptivity region $\xi = O(1)$, the mean flow is close to the Blasius solution, and the receptivity coefficient is calculated as a perturbation away from the flat-plate value. Receptivity to the symmetric and anti-symmetric components of the unsteady free-stream disturbance is analyzed in §§3.3 and 3.4, respectively. In each case the solutions in the nose and receptivity regions are asymptotically matched, and then the large-ξ behavior in the receptivity region is compared to (3.18) in order to extract the receptivity coefficient, C_s or C_a.

3.3 Receptivity to symmetric forcing

For symmetric forcing, (3.21a) suggests that for small S the unsteady perturbation in the nose region, $\bar{\xi} = O(1)$, is quasi-steady at leading order and takes the form

$$\psi_s = S^{\frac{1}{2}} \bar{\xi} \left(\theta_0(\bar{\xi}, \eta) + S \, \theta_1(\bar{\xi}, \eta) + O(S^2) \right),$$

(3.22)

where the functions θ_0 and θ_1 satisfy

$$\begin{aligned} \mathcal{M}_s(\theta_0) &= -\frac{2}{1 + \bar{\xi}^2}, \\ \mathcal{M}_s(\theta_1) &= \mathrm{i}(1 + \bar{\xi}^2)(1 - (\theta_0)_\eta), \end{aligned} \Bigg\}$$

(3.23)

and

$$\mathcal{M}_s(p) \equiv p_{\eta\eta\eta} + (\phi + \bar{\xi}\phi_{\bar{\xi}})p_{\eta\eta} + \left(-\bar{\xi}\phi_{\eta\bar{\xi}} - \frac{2}{1 + \bar{\xi}^2}\phi_\eta \right) p_\eta + \phi_{\eta\eta}p + \bar{\xi}(\phi_{\eta\eta}p_{\bar{\xi}} - \phi_\eta p_{\eta\bar{\xi}}). \quad (3.24)$$

The factor $S^{\frac{1}{2}}\bar{\xi}$ is extracted from ψ_s in (3.22) to simplify the boundary conditions, which become

$$\begin{array}{llll} \theta_0 = \dfrac{\partial \theta_0}{\partial \eta} = 0 & \theta_1 = \dfrac{\partial \theta_1}{\partial \eta} = 0 & \text{on} \quad \eta = 0 \\[2mm] \dfrac{\partial \theta_0}{\partial \eta} \to 1 & \dfrac{\partial \theta_1}{\partial \eta} \to 0 & \text{exponentially as} \quad \eta \to \infty. \end{array} \Bigg\}$$

(3.25)

Here we are interested in the solution in the large-$\bar{\xi}$ limit, in order to provide upstream boundary conditions for the receptivity region $\xi = O(1)$. In this limit, the mean flow is given by (3.8) and the unsteady perturbation takes the form,

$$
\left.
\begin{aligned}
\theta_0 &\sim H_0(\eta) + \frac{\ln(\bar{\xi}^2)}{\bar{\xi}^2} H_3(\eta) + \frac{1}{\bar{\xi}^2} H_4(\eta) + O(\bar{\xi}^{-\gamma_2}), \\
\theta_1 &\sim \bar{\xi}^2 \widehat{H}_0(\eta) + \ln(\bar{\xi}^2)\widehat{H}_3(\eta) + \widehat{H}_4(\eta) + O(\bar{\xi}^{(2-\gamma_2)}),
\end{aligned}
\right\}
\tag{3.26}
$$

where we have adopted this rather unusual labeling notation in order to retain consistency with the notation used in §3.4. The set of functions $H_i(\eta)$ and $\widehat{H}_i(\eta)$ satisfy

$$
\left.
\begin{aligned}
\mathcal{G}_0(H_0) &= 0, & \mathcal{G}_{-2}(\widehat{H}_0) &= i(1 - H_0'), \\
\mathcal{G}_2(H_3) &= \mathcal{R}_{2,1}^{(3)}(H_0), & \mathcal{G}_0(\widehat{H}_3) &= -iH_3' + \mathcal{R}_{0,3}^{(3)}(\widehat{H}_0), \\
\mathcal{G}_2(H_4) &= -2 - \mathcal{R}_{2,1}^{(4)}(H_0) & \mathcal{G}_0(\widehat{H}_4) &= i(1 - H_0' - H_4') - \mathcal{R}_{0,3}^{(4)}(\widehat{H}_0) \\
&\quad + 2F'H_3' - 2F''H_3, & &\quad + 2F'\widehat{H}_3' - 2F''\widehat{H}_3,
\end{aligned}
\right\}
\tag{3.27}
$$

subject to boundary conditions

$$
\left.
\begin{aligned}
H_i = H_i' &= 0, & \widehat{H}_i = \widehat{H}_i' &= 0, & \text{on } \eta &= 0, \\
H_0' \to 1, \quad H_{i\geq 1}' &\to 0, & \widehat{H}_i' &\to 0, & \text{as } \eta &\to \infty,
\end{aligned}
\right\}
\tag{3.28}
$$

where the decay is exponential as $\eta \to \infty$. Here the operator $\mathcal{G}_\gamma$ is defined in (3.11) and the operators $\mathcal{R}_{\beta,\gamma}^{(i)}$ are defined in Appendix C. As was noted in §3.2, $\mathcal{G}_2$ has an eigensolution (i.e. a solution of $\mathcal{G}_2(H) = 0$ with homogeneous boundary conditions). Thus H_3 and H_4 can not be determined entirely by the large-$\bar{\xi}$ asymptotic analysis, but require knowledge of the full solution in the nose region. However, for the symmetric case considered in this section, the leading-order term in the small-S expansion can be determined exactly in terms of the steady flow (Lighthill 1954). In the notation of the present chapter this gives the quasi-steady solution as $\theta_0 = \frac{1}{2}(\eta\phi_\eta + \phi)$ and hence,

$$
H_0 = \tfrac{1}{2}(\eta F' + F), \qquad H_3 = \tfrac{1}{2}(\eta \overline{G}_1' + \overline{G}_1), \qquad H_4 = \tfrac{1}{2}(\eta \overline{G}_2' + \overline{G}_2),
\tag{3.29}
$$

where $\overline{G}_1(\eta)$, $\overline{G}_2(\eta)$ are defined in (3.12, 3.13). Solutions for $\widehat{H}_i$ are obtained using a fourth-order Runge-Kutta method, shooting from $\eta = 0$ and using the requirement of exponential decay as $\eta \to \infty$.

It is clear from (3.26) that the small-S expansion (3.22) breaks down when $S\bar{\xi}^2 = O(1)$, which is to be expected since when $\xi = O(1)$ we have reached the receptivity regime where unsteadiness enters at leading order. Within the receptivity region, we are interested only in the coefficient of the first eigensolution. We therefore anticipate the large-ξ form (3.18) by setting $\psi = \xi w(\xi, \eta) e^{-\lambda \xi^3/3}$, where $\lambda = e^{-\frac{1}{4}i\pi}/(\rho_1^{3/2}U_0')$ as before. From (3.21a), w is given by

$$
\left.
\begin{aligned}
\mathcal{N}_s(w) &= \left[i(S + \xi^2) - \frac{2S}{S + \xi^2} \right] e^{\lambda\xi^3/3}, \\
\mathcal{N}_s(w) &\equiv w_{\eta\eta} + [\phi + \xi\phi_\xi]w_\eta + \left[i(S + \xi^2) - \xi\phi_{\eta\xi} + \left(\lambda\xi^3 - \frac{2S}{S + \xi^2} \right) \phi_\eta \right] w_\eta \\
&\quad + (1 - \lambda\xi^3)\phi_{\eta\eta}w + \xi(\phi_{\eta\eta}w_\xi - \phi_\eta w_{\eta\xi}).
\end{aligned}
\right\}
\tag{3.30}
$$

36

Using the large-$\bar{\xi}$ form of ϕ (3.8), we see that the coefficients which appear in $\mathcal{N}_s(w)$ involve terms in $(\xi^2/S)^{-1} \ln(\xi^2/S)$ and $(\xi^2/S)^{-1}$, and hence we can expand $\mathcal{N}_s$ as an asymptotic series in S,

$$\mathcal{N}_s(w) \sim \mathcal{N}_{0,1}^{(0)}(w) + S \ln S \mathcal{N}_{2,1}^{(3)}(w) + S \mathcal{N}_{2,1}^{(4)}(w) + O(S^{\gamma_2/2}), \qquad (3.31)$$

where the partial differential operators $\mathcal{N}_{\beta,\gamma}^{(i)}(w)$ are defined in Appendix C. Now writing

$$w(\xi, \eta; S) \sim w_0 + S \ln S w_3 + S w_4 + O(S^{\gamma_2/2}), \qquad (3.32)$$

and expanding the right side of (3.30), we obtain a set of equations governing the evolution of $w_i(\xi, \eta)$,

$$\left.\begin{aligned}
\mathcal{N}_{0,1}^{(0)}(w_0) &= i\xi^2 e^{\lambda\xi^3/3}, \\
\mathcal{N}_{0,1}^{(0)}(w_3) &= -\mathcal{N}_{2,1}^{(3)}(w_0), \\
\mathcal{N}_{0,1}^{(0)}(w_4) &= (i - 2/\xi^2)e^{\lambda\xi^3/3} - \mathcal{N}_{2,1}^{(4)}(w_0).
\end{aligned}\right\} \qquad (3.33)$$

Matching back to (3.26) we see that as $\xi \to 0$,

$$\left.\begin{aligned}
w_0 &\sim H_0 + \xi^2 \widehat{H}_0, \\
w_3 &\sim -\frac{1}{\xi^2}H_3 - \widehat{H}_3, \\
w_4 &\sim \frac{\ln(\xi^2)}{\xi^2}H_3 + \frac{1}{\xi^2}H_4 + \ln(\xi^2)\widehat{H}_3 + \widehat{H}_4.
\end{aligned}\right\} \qquad (3.34)$$

Thus we write

$$\left.\begin{aligned}
w_0 &= e^{\lambda\xi^3/3}H_0 + \xi^2 q_0, \\
w_3 &= -\frac{1}{\xi^2}e^{\lambda\xi^3/3}H_3 + q_3, \\
w_4 &= -\ln(\xi^2)w_3 + \frac{1}{\xi^2}e^{\lambda\xi^3/3}H_4 + q_4,
\end{aligned}\right\} \qquad (3.35)$$

and it can be shown after some algebraic manipulation that

$$\left.\begin{aligned}
\mathcal{N}_{-2,3}^{(0)}(q_0) &= ie^{\lambda\xi^3/3}(1 - H_0'), \\
\mathcal{N}_{0,1}^{(0)}(q_3) &= ie^{\lambda\xi^3/3}H_3' - \overline{\mathcal{N}}_{0,3}^{(3)}(q_0), \\
\mathcal{N}_{0,1}^{(0)}(q_4) &= ie^{\lambda\xi^3/3}(1 - H_0' - H_4') - i\xi^2 q_0' - \overline{\mathcal{N}}_{0,3}^{(4)}(q_0) + 2F''q_3 - 2F'q_3',
\end{aligned}\right\} \qquad (3.36)$$

where q_i' denotes the partial derivative of $q_i(\xi, \eta)$ with respect to η. From (3.34), the functions q_i satisfy initial conditions

$$q_0(0, \eta) = \widehat{H}_0, \qquad q_3(0, \eta) = -\widehat{H}_3(\eta), \qquad q_4(0, \eta) = \widehat{H}_4(\eta), \qquad (3.37)$$

and homogeneous boundary conditions, $q_i(\xi, 0) = q_i'(\xi, 0) = 0$, $q_i' \to 0$ exponentially as $\eta \to \infty$. The differential operators $\overline{\mathcal{N}}_{\beta,\gamma}^{(i)}$, related to the operators $\mathcal{N}_{\beta,\gamma}^{(i)}$, are defined in Appendix C. Thus the evolution of the $O(S^0)$, $O(S \ln S)$ and $O(S)$ components of the unsteady flow has been cast in a form suitable for accurate numerical computation. Numerical solutions of (3.36) are discussed in §3.5.

3.4 Receptivity to antisymmetric forcing

At first sight, the analysis of the receptivity in the anti-symmetric case appears to follow very similarly to the symmetric case. However, a subtle difference is seen in the structure of the solution. Motivated by the anti-symmetric forcing (3.21b), we write the small-S expansion of the unsteady perturbation in the nose region, $\bar{\xi} = O(1)$, as

$$\psi_a = \psi_0(\bar{\xi}, \eta) + S\,\psi_1(\bar{\xi}, \eta) + O(S^2). \tag{3.38}$$

The perturbation is again quasi-steady at leading order in the nose region, with

$$\left.\begin{array}{rcl}
\mathcal{M}_a(\psi_0) &=& \dfrac{\bar{\xi}^2 - 1}{\bar{\xi}^2 + 1}, \\[2mm]
\mathcal{M}_a(\psi_1) &=& \mathrm{i}(1 + \bar{\xi}^2)(1 - (\psi_0)_\eta),
\end{array}\right\} \tag{3.39}$$

where

$$\mathcal{M}_a(p) \equiv \mathcal{M}_s(p) + \phi_\eta p_\eta - \phi_{\eta\eta} p. \tag{3.40}$$

However, in contrast to the symmetric case, the large-$\bar{\xi}$ limit for the unsteady flow now takes the form

$$\left.\begin{array}{rcl}
\psi_0 &\sim& J_0(\eta) + \dfrac{\ln(\bar{\xi}^2)}{\bar{\xi}} J_1(\eta) + \dfrac{1}{\bar{\xi}} J_2(\eta) + \dfrac{\ln(\bar{\xi}^2)}{\bar{\xi}^2} J_3(\eta) + \dfrac{1}{\bar{\xi}^2} J_4(\eta) + O(\bar{\xi}^{(1-\gamma_2)}) \\[3mm]
\psi_1 &\sim& \bar{\xi}^2 \hat{J}_0(\eta) + \bar{\xi}\ln(\bar{\xi}^2)\hat{J}_1(\eta) + \bar{\xi}\hat{J}_2(\eta) + \ln(\bar{\xi}^2)\hat{J}_3(\eta) + \hat{J}_4(\eta) + O(\bar{\xi}^{(3-\gamma_2)})
\end{array}\right\} \tag{3.41}$$

where the functions $J_i(\eta)$ and $\hat{J}_i(\eta)$ satisfy

$$\left.\begin{array}{rclcrcl}
\mathcal{G}_1(J_0) &=& 1, & \quad & \mathcal{G}_{-1}(\hat{J}_0) &=& \mathrm{i}(1 - J_0'), \\[1mm]
\mathcal{G}_2(J_1) &=& 0, & & \mathcal{G}_0(\hat{J}_1) &=& -\mathrm{i}J_1', \\[1mm]
\mathcal{G}_2(J_2) &=& 2F'J_1' - 2F''J_1, & & \mathcal{G}_0(\hat{J}_2) &=& -\mathrm{i}J_2' + 2F'\hat{J}_1' - 2F''\hat{J}_1, \\[1mm]
\mathcal{G}_3(J_3) &=& \mathcal{R}_{3,0}^{(3)}(J_0), & & \mathcal{G}_1(\hat{J}_3) &=& -\mathrm{i}J_3' + \mathcal{R}_{1,2}^{(3)}(\hat{J}_0), \\[1mm]
\mathcal{G}_3(J_4) &=& -2 - \mathcal{R}_{3,0}^{(4)}(J_0) & & \mathcal{G}_1(\hat{J}_4) &=& \mathrm{i}(1 - J_0' - J_4') - \mathcal{R}_{1,2}^{(4)}(\hat{J}_0) \\[1mm]
& & +2F'J_3' - 2F''J_3, & & & & +2F'\hat{J}_3' - 2F''\hat{J}_3,
\end{array}\right\} \tag{3.42}$$

with boundary conditions

$$\left.\begin{array}{rclcrclcll}
J_i &=& J_i' &=& 0 & \quad \hat{J}_i = \hat{J}_i' = 0 & \quad & \text{on} & \eta = 0 \\[1mm]
J_0' \to 1, & & J_{i\geq 1}' &\to& 0 & \quad \hat{J}_i' \to 0 & & \text{as} & \eta \to \infty.
\end{array}\right\} \tag{3.43}$$

Compared to the expansion for the symmetric case (3.26), the additional terms in $\ln(\bar{\xi}^2)/\bar{\xi}$ and $1/\bar{\xi}$ are included in the large-$\bar{\xi}$ expansion of ψ_0 because the operator $\mathcal{G}_2$ possesses an eigensolution. Thus $J_1(\eta) = P_1(\eta F' - F)$, where the numerical constant P_1 can be determined from the solvability condition for J_2. As noted in §3.2, the Blasius function F is the solution to the adjoint of $\mathcal{G}_2$ and we see that

$$\begin{aligned}
0 &= \int_0^\infty F(F'J_1' - F''J_1)\,\mathrm{d}\eta = 2P_1 \int_0^\infty F^2 F''\,\mathrm{d}\eta \\
&= P_1.
\end{aligned} \tag{3.44}$$

Hence $J_1 \equiv 0$ and it follows that $\hat{J}_1 \equiv 0$, and $J_2(\eta) = P_2(\eta F' - F)$, where P_2 is a numerical constant. Solutions to the set of equations (3.42) are obtained by shooting, as

described in §3.3, but the value of the constant P_2 in the expression for J_2 can only be determined by comparison with numerical solutions of ψ_0 obtained by integrating (3.39) forward from $\bar{\xi} = 0$. Comparing the computed wall shear $\psi_0''(\bar{\xi}, 0)$, with the asymptotic form (3.41) gives

$$P_2 \approx 6.07, \tag{3.45}$$

but accurate extrapolation is difficult due to the presence of higher-order terms in the expansion (3.41). The numerical results suggest that the coefficients of these terms are in fact relatively large. This is discussed further in §3.5.

In the receptivity region $\xi = O(1)$ where unsteadiness enters at leading order, we again anticipate the large-ξ form of the eigensolution by setting $\psi_a = v e^{-\lambda \xi^3/3}$. The function $v(\xi, \eta; S)$ then satisfies

$$\left. \begin{aligned} \mathcal{N}_a(v) &= \left[i(S + \xi^2) - \frac{S - \xi^2}{S + \xi^2} \right] e^{\lambda \xi^3/3}, \\ \mathcal{N}_a(v) &\equiv \mathcal{N}_s(v) + \phi_\eta v_\eta - \phi_{\eta\eta} v, \end{aligned} \right\} \tag{3.46}$$

where $\mathcal{N}_s(v)$ was defined in §3.3. As for the symmetric case, we expand the operator as an asymptotic series in S,

$$\mathcal{N}_a(v) \sim \mathcal{N}_{1,0}^{(0)}(v) + S \ln S \mathcal{N}_{3,0}^{(3)}(v) + S \mathcal{N}_{3,0}^{(4)}(v) + O(S^{\gamma_2/2}), \tag{3.47}$$

but in this case, guided by the asymptotic form (3.41) in the nose region, we expand $v(\xi, \eta; S)$ as

$$v \sim v_0 + S^{1/2} v_2 + S \ln S v_3 + S v_4 + O(S^{(\gamma_2 - 1)/2}). \tag{3.48}$$

Matching back to the nose region then suggests that we set

$$\left. \begin{aligned} v_0 &= e^{\lambda \xi^3/3} J_0 + \xi^2 p_0, \\ v_2 &= \frac{1}{\xi} e^{\lambda \xi^3/3} J_2 + \xi p_2, \\ v_3 &= -\frac{1}{\xi^2} e^{\lambda \xi^3/3} J_3 + p_3, \\ v_4 &= -\ln(\xi^2) v_3 + \frac{1}{\xi^2} e^{\lambda \xi^3/3} J_4 + p_4. \end{aligned} \right\} \tag{3.49}$$

This finally leads to the set of equations

$$\left. \begin{aligned} \mathcal{N}_{-1,2}^{(0)}(p_0) &= i e^{\lambda \xi^3/3} (1 - J_0'), \\ \mathcal{N}_{0,1}^{(0)}(p_2) &= -i e^{\lambda \xi^3/3} J_2', \\ \mathcal{N}_{1,0}^{(0)}(p_3) &= i e^{\lambda \xi^3/3} J_3' - \overline{\mathcal{N}}_{1,2}^{(3)}(p_0), \\ \mathcal{N}_{1,0}^{(0)}(p_4) &= i e^{\lambda \xi^3/3} (1 - J_0' - J_4') - i \xi^2 p_0' - \overline{\mathcal{N}}_{1,2}^{(4)}(p_0) + 2 F'' p_3 - 2 F' p_3', \end{aligned} \right\} \tag{3.50}$$

with initial conditions

$$p_0(0, \eta) = \hat{J}_0, \qquad p_2(0, \eta) = \hat{J}_2, \qquad p_3(0, \eta) = -\hat{J}_3(\eta), \qquad p_4(0, \eta) = \hat{J}_4(\eta), \tag{3.51}$$

and the homogeneous boundary conditions, $p_i(\xi, 0) = p_i'(\xi, 0) = 0$, $p_i' \to 0$ exponentially as $\eta \to \infty$. As in §3.3, we use p_i' to denote the partial derivative of $p_i(\xi, \eta)$ with respect to η. Numerical solutions to this set of equations are discussed in the next section.

39

3.5 Numerical Results

Having obtained expressions for the evolution of the unsteady flow in the form of an asymptotic expansion for small S, we now carry out the numerical integration required to obtain the corresponding asymptotic expansion for the receptivity coefficient $C_1(S)$. As explained in chapter 2, in order to reliably extract the coefficient $C_1(S)$ of the first asymptotic eigensolution from the numerical results, it is necessary to carry out the integration in the complex-ξ plane, in the region $-5\pi/12 < \arg(\xi) < -\pi/12$ where the first eigensolution of the LUBLE exhibits exponential growth and is the dominant component of the solution at large ξ. The sets of equations (3.36) and (3.50) were integrated forward in ξ, from $\xi = 0$ to $|\xi| = 10$ using a Keller Box scheme (Keller & Cebeci (1970)), with $\arg(\xi)$ chosen as either $-\pi/3$ or $-\pi/4$ to ensure the dominance of the first eigensolution.

For large ξ, the first asymptotic eigensolution is given by (3.18). Expanding the expression for the first eigensolution (3.18) for small S, and writing the receptivity coefficient, $C_a(S)$ or $C_s(S)$, as an expansion for small S,

$$C(S) \sim C(0)(1 + c_2 S^{1/2} + c_3 S \ln S + c_4 S + \ldots), \tag{3.52}$$

we see that as $\xi \to \infty$ in the region of the complex plane of interest,

$$\begin{aligned}
\psi \sim \psi_0(1 &+ c_2 S^{1/2} + [c_3 - \lambda A_1 \xi]S \ln S + \\
&[c_4 + \tau_1 \ln(\xi^2/2) - \lambda\xi(2A_1 + \tfrac{3}{2} - B_1 - A_1 \ln(\xi^2))]S),
\end{aligned} \tag{3.53}$$

where ψ_0 is the first eigensolution for the flat-plate case (Goldstein 1983). The coefficients $C(0)$, c_2, c_3 and c_4 can then be obtained by comparison with the numerical solution either at the outer edge of the boundary layer or at the wall.

For the symmetric case clearly $c_2^{(s)} = 0$, while $C_s(0)$, $c_3^{(s)}$, $c_4^{(s)}$ are extracted from the limiting forms

$$\left.\begin{aligned}
w_0 &\sim C_s(0)\,(\xi^2/2)^{\tau_1^{(0)}}\,[1 + O(\xi^{-1})], \\
w_3/w_0 &\sim c_3^{(s)} - \lambda A_1 \xi, \\
w_4/w_0 &\sim c_4^{(s)} + \tau_1^{(1)} \ln(\xi^2/2) - \lambda\xi(2A_1 + \tfrac{3}{2} - B_1 - A_1 \ln(\xi^2)),
\end{aligned}\right\} \tag{3.54}$$

as $\eta, \xi \to \infty$. The evolution of w_0 is the flat-plate case described by Goldstein and gives

$$C_s(0) = -0.441 + 0.841\,\mathrm{i} \tag{3.55}$$

as the receptivity coefficient for a flat plate, in agreement with earlier results (Goldstein et al. 1983; Heinrich & Kerschen 1989). Using $\arg(\xi) = -\pi/4$, the corrections taking account of small nose radius effects are calculated to be

$$c_3^{(s)} \approx 0, \qquad c_4^{(s)} \approx 3.12 - 2.37\,\mathrm{i}. \tag{3.56}$$

Integration using $\arg(\xi) = -\pi/3$ gives a difference of less than 2% in the estimate for $c_4^{(s)}$. Hence

$$\left.\begin{aligned}
\mathrm{Re}(C_s(S)) &\sim -0.441 + 0.62\,S + O(S^{\alpha_1}) \\
\mathrm{Im}(C_s(S)) &\sim 0.841 + 3.67\,S + O(S^{\alpha_1}), \quad \alpha_1 = \tfrac{1}{2}\gamma_2 \approx 1.887.
\end{aligned}\right\} \tag{3.57}$$

In figure 3.2 asymptotic results (3.56) are compared with the results of the full integration
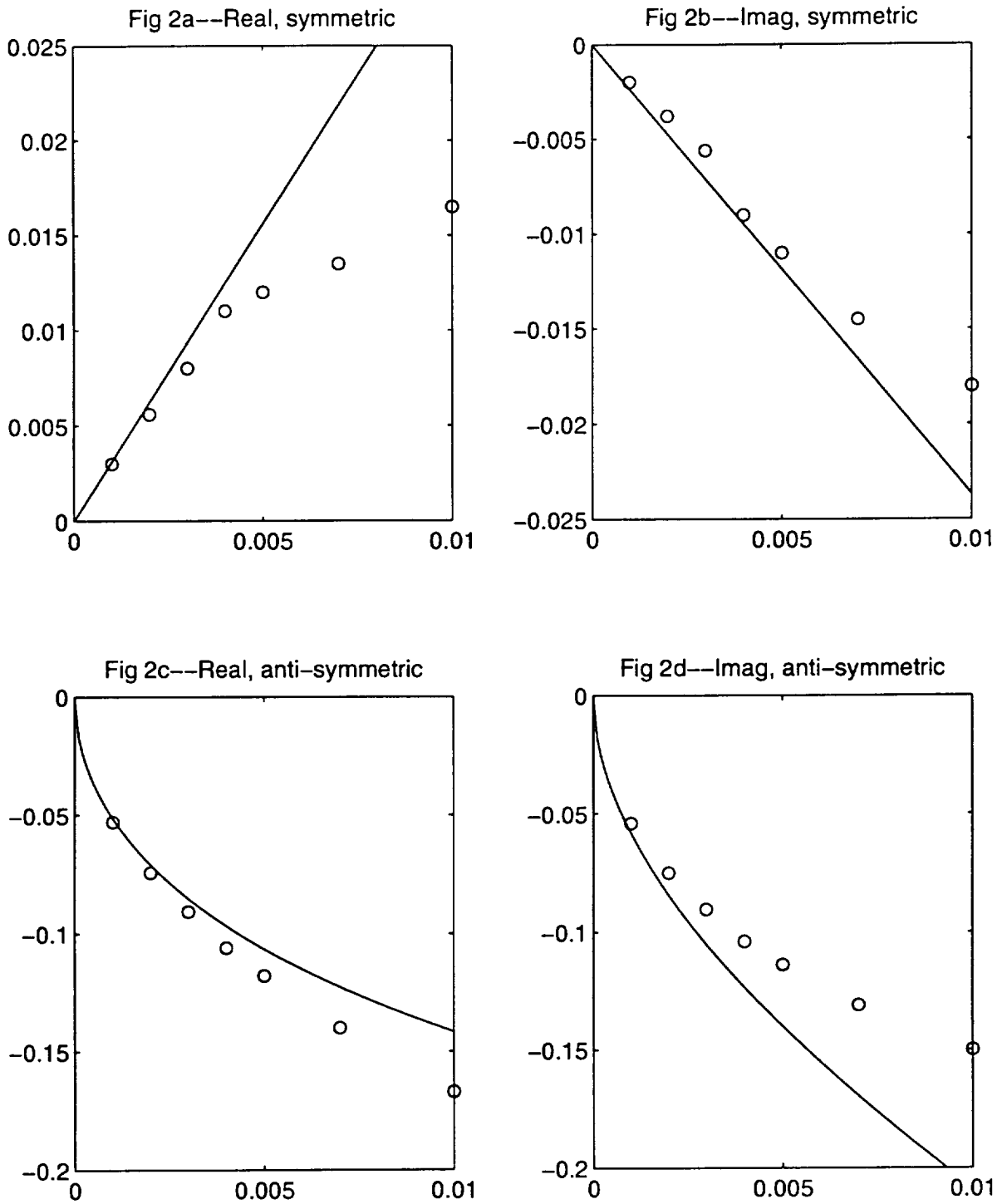
Figure 3.2: Comparison of numerical and asymptotic results for the receptivity due to symmetric and anti-symmetric disturbances. Numerical results for the perturbation $f(S) = (C(S) - C(0))/C(0)$ (see text) are denoted by o, asymptotic theory is marked by the solid line. Results for $\mathrm{Re}(f_s)$ and $\mathrm{Im}(f_s)$ are illustrated in (a) and (b), respectively, and $\mathrm{Re}(f_a)$ and $\mathrm{Im}(f_a)$ are illustrated in (c) and (d).

41

for small-S presented in chapter 2. To make the comparisons as clear as possible, we plot the perturbation from the flat plate result $f(S) = (C(S) - C(0))/C(0)$ as a function of S and compare this with the asymptotic form (3.52). In figure 3.2a and b, comparisons are made for the symmetric case, making it clear that the leading-order behavior for the symmetric receptivity coefficient is indeed described by (3.57). The small discrepancy between numerical results and asymptotic theory is likely to be due either to numerical uncertainty in extrapolating $C(S)$ from large-ξ calculations (as explained in chapter 2), or to the higher-order terms in (3.57).

For the anti-symmetric case,

$$\left.\begin{aligned}
v_0 &\sim C_a(0)\xi\,(\xi^2/2)^{\tau_1^{(0)}}\,[1 + O(\xi^{-1})], \\
v_2/v_0 &\sim c_2^{(a)}, \\
v_3/v_0 &\sim c_3^{(a)} - \lambda A_1\xi, \\
v_4/v_0 &\sim c_4^{(a)} + \tau_1^{(1)}\ln(\xi^2/2) - \lambda\xi(2A_1 + \tfrac{3}{2} - B_1 - A_1\ln(\xi^2)),
\end{aligned}\right\} \tag{3.58}$$

as $\eta, \xi \to \infty$. Comparing these large-ξ asymptotic forms with numerical results gives

$$C_a(0) \approx -5.33 + 1.66\,\mathrm{i}, \tag{3.59}$$

as the flat-plate solution, with small-S corrections

$$c_2^{(a)} \approx -1.728 - 1.728\,\mathrm{i}, \qquad c_3^{(a)} \approx 0, \qquad c_4^{(a)} \approx 3.12 - 3.57\,\mathrm{i}. \tag{3.60}$$

Again there is no significant difference in these results if $\arg(\xi)$ is varied. Hence

$$\left.\begin{aligned}
\mathrm{Re}(C_a(S)) &\sim -5.33 \;+12.08\,S^{1/2} \;-10.7\,S \;+O(S^{\alpha_2}) \\
\mathrm{Im}(C_a(S)) &\sim 1.66 \;+\; 6.34\,S^{1/2} \;+24.2\,S \;+O(S^{\alpha_2}), \quad \alpha_2 = \frac{1}{2}(\gamma_2 - 1) \approx 1.387
\end{aligned}\right\} \tag{3.61}$$

In figure 3.2c and d the asymptotic results (3.60) are compared with the results of the full integration for small-S presented in chapter 2. It is clear that the coefficient of the $S^{\frac{1}{2}}$ term in (3.61) is correct. While it is not possible to be certain from these results that the $O(S)$ terms are also correct, the divergence of the asymptotic results from numerical results arises at similar values of S to the symmetric case, when the $O(S)$ terms were seen to be correct. In addition, it should be noted that the next higher order term in (3.61) is $O(S^{\alpha_2})$, $\alpha_2 \approx 1.387$ which is very close in magnitude to the $O(S)$ term retained. Comparison of numerical results and asymptotic solutions in the nose region suggests that the coefficient of the next term in the expansion (3.41) is fairly large, further suggesting that the $O(S^{\alpha_2})$ in (3.61) is indeed significant, even for small S. Hence figure 3.2c and d shows that the asymptotic form (3.61) is at least consistent with numerical results.

The absence of any $S \ln S$ term in the expansions of the symmetric and anti-symmetric receptivity coefficients is somewhat surprising. However, further insight can be gained by considering the case $\arg(\xi) = -\pi/4$ in more detail. In this special case, the operators $\mathcal{N}^{(0)}, \overline{\mathcal{N}}^{(3)}$ and $\overline{\mathcal{N}}^{(4)}$ defined in Appendix C are real. Noting that the set of functions $\widehat{H}(\eta)$ are purely imaginary, equations (3.36) show that the functions $q_i(\xi, \eta)$ are also wholly imaginary. Hence in the limit $|\xi| \to \infty$, w_3/w_0 is imaginary and $\mathrm{Re}(c_3^{(s)}) = 0$. That is, if there is a $S \ln S$ term in the small-S expansion of $C_s(S)$, then it is wholly imaginary. Furthermore, we can show from the large-ξ limit of w_4/w_0, that

$$\mathrm{Re}(c_4^{(s)}) = -\frac{\pi}{2}\mathrm{Im}(\tau_1^{(1)} + c_3^{(s)}). \tag{3.62}$$

These results are in agreement with the numerical results. The same results also apply to the anti-symmetric case. Further consideration of the large-ξ limit of w_0 and v_0 for $\arg(\xi) = -\pi/4$ proves that

$$\arg(C_s(0)) = -\frac{\pi}{2}(1 + \tau_1^{(0)}), \qquad \arg(C_a(0)) = -\frac{\pi}{2}(\tfrac{1}{2} + \tau_1^{(0)}) \qquad (3.63)$$

which confirms the numerics, and also explains the $\pi/4$ difference in phase between flat-plate receptivity coefficients for symmetric and anti-symmetric forcing noted in chapter 2.

3.6   Summary

In §3.5, the small-S expansions of the real and imaginary parts of the receptivity coefficients for symmetric and anti-symmetric forcing were compared with numerical results. From a practical standpoint, the most important quantity is the modulus of the receptivity coefficient, since it is the variation of this that is likely to influence the position of the transition point. In figure 3.3, the asymptotic prediction for the modulus of the receptivity coefficient is compared to numerical results, for symmetric and anti-symmetric forcing. For oblique acoustic waves ($\theta \neq 0$), the coefficient κ_a in (3.20) is often large compared to κ_s (see chapter 2). Moreover, as $S \to 0$ the anti-symmetric receptivity coefficient C_a is approximately five times larger than C_s, the symmetric receptivity coefficient. Hence $C_a(S)$ is much more important than $C_s(S)$ in determining the behavior of the total receptivity coefficient $C_1(S)$. In this chapter, we have shown that $C_a(S)$ has a singular structure for small S, varying as $S^{\frac{1}{2}}$, so that small changes in this parameter have a significant influence on the receptivity. Moreover, the exact form of this leading-order behavior has been accurately calculated. The rather small range of validity of the asymptotic expansions at first appears somewhat disappointing. However, numerical results show that the maximum receptivity occurs for small S and hence the behavior in this limit is of most interest for practical applications. For $S < 0.005$, excellent agreement is seen between asymptotic theory and numerical results, so in this parameter range the asymptotic expansions developed in this chapter are of quantitative as well as qualitative value.

The small-S limit is also of interest when considering the experimental results of Saric *et al.* (1995). In these wind-tunnel tests, a leading edge consisting of a machined super-ellipse of either 1:20 or 1:40 aspect ratio is attached to a flat plate. By considering a super-ellipse profile rather than an ellipse for the leading-edge section, localized receptivity due to a discontinuity in surface curvature at the join with the flat plate (Goldstein 1985) is eliminated. The region of dominant receptivity should then be the leading edge. Measurements were made for free-stream speeds $8\text{ms}^{-1} < U < 21\text{ms}^{-1}$, corresponding to nose radius Reynolds numbers $Re_n = Ur_n/\nu$ in the range $130 < Re_n < 670$, consistent with the assumption $Re_n \gg 1$ used in our analysis. Acoustic forcing at non-dimensional frequencies in the range $30 \times 10^{-6} < \epsilon^6 < 90 \times 10^{-6}$ was considered, leading to a Strouhal number range $0.004 < S < 0.060$. Our small-S theory is clearly relevant to the lower end of this Strouhal number range. The results of the present analysis show that, despite the small values of the nose radius in these experiments, there can be significant departures from the flat-plate results. Many of the detailed measurements of Saric *et al.* are for a Strouhal number of 0.01. For this value of S, symmetric disturbances lead to receptivity
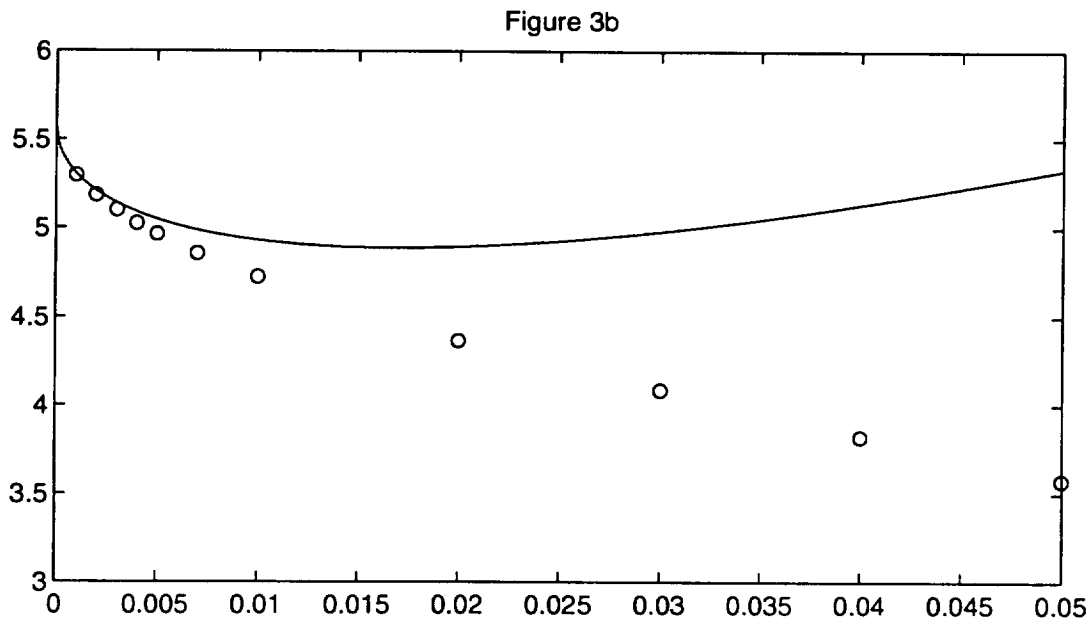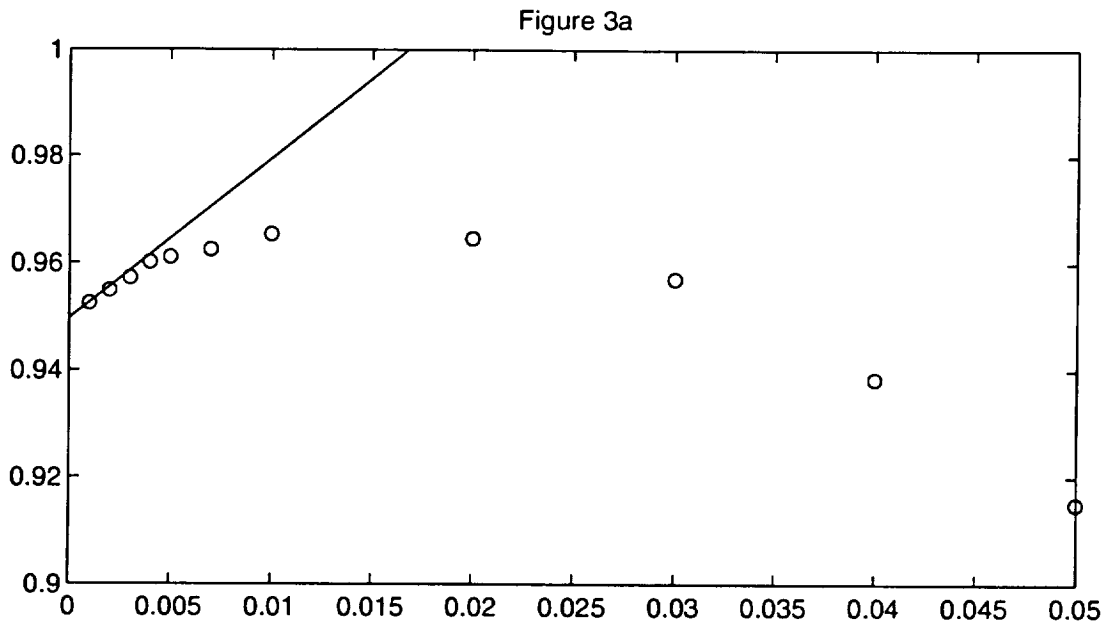
Figure 3.3: Comparison of numerical and asymptotic results for the modulus of the receptivity coefficient for *(a)* symmetric forcing, $|C_s|$ vs. S, and *(b)* anti-symmetric forcing, $|C_a|$ vs. S. Numeric results are denoted by o, asymptotic theory is marked by the solid line.

2% greater than the flat plate value, but for anti-symmetric forcing there is a 15% reduction compared to the flat-plate result. As noted earlier, despite the small numerical values of S, by $S = 0.01$ the computed value of the receptivity coefficient has already begun to diverge from the asymptotic results.

For leading-edge receptivity, various measures of receptivity can be considered. We have chosen to define C_1, the coefficient of the first Lam–Rott asymptotic eigenfunction, as the 'receptivity coefficient'. Alternative definitions of receptivity level that have been considered in computations and experiments are values based on the Tollmien–Schlichting wave amplitude at the lower neutral-stability point (branch I), or on an extrapolation of the Tollmien–Schlichting wave amplitude back to the leading edge. Extrapolation of the Tollmien–Schlichting wave amplitude back to the leading edge is not advisable, since the Tollmien–Schlichting wave is not a valid solution of the disturbance equations near the leading edge. In fact, in extrapolating back to the leading edge the slowly varying amplitude $A(\xi)$ multiplying the mode-shape function of the Tollmien–Schlichting wave should be considered, and $A(\xi)$ becomes infinite at the leading edge, the streamwise velocity fluctuation behaving as $\xi^{2\tau_1}$ where $\tau_1 = \tau_1^{(0)} + S\tau_1^{(1)}$ is given by (3.18).

A receptivity level defined in terms of the Tollmien–Schlichting wave amplitude at the lower branch neutral-stability point does allow easy comparison with experiments or computations, but has the disadvantage that the results depend on the frequency and Reynolds number, making presentation of the results much less compact. However, there is a need to relate receptivity levels defined in terms of C_1 to levels expressed in terms of branch I amplitudes. In the asymptotic theory, this is achieved by developing the asymptotic expression for the Tollmien–Schlichting wave in the OSE region and matching this expression to the first generalized Lam–Rott asymptotic eigensolution (3.18). This procedure is discussed by Goldstein (1983) for the flat-plate case, and the extension to non-zero S is discussed briefly in chapter 2. However, the asymptotic analysis is quite laborious, especially for the determination of $A(\xi)$. An alternative approach is the numerical solution of the disturbance equations, using the Lam–Rott asymptotic eigensolution as a starting condition and continuing downstream to branch I.

From a theoretical standpoint, the most attractive measure of receptivity is the coefficient C_1 of the first Lam–Rott asymptotic eigenfunction. This Lam–Rott eigenfunction evolves into the unstable Tollmien–Schlichting wave farther downstream so that, when appropriate scaling factors related to the asymptotic matching of the LUBLE and OSE regions are introduced, C_1 is also the coefficient of the Tollmien–Schlichting wave. An extremely attractive feature of this receptivity measure is that C_1 is independent of the physical frequency and the (asymptotically large) Reynolds number, thus providing the receptivity results in the simplest dimensionless form. The quantity C_1 is determined by the unsteady flow behavior upstream of the region of instability and therefore focuses on the receptivity aspect of the unsteady flow development, with less influence from the global stability properties of the flow. Also, for fixed values of the frequency and Reynolds number, variations in the receptivity coefficient C_1 with changes in the free-stream disturbance characteristics translate directly into variations in the Tollmien–Schlichting wave amplitude.

Chapter 4

Receptivity for a leading edge with aerodynamic loading

4.1 Introduction

The transition of a boundary-layer flow from laminar to turbulent is strongly influenced by free-stream disturbances. The process by which free-stream disturbances generate instability waves in the boundary layer is known as receptivity (Morkovin 1969). Energy is transferred from long-wavelength disturbances in the free stream to the much shorter wavelength Tollmien–Schlichting waves in the boundary layer. This transfer requires a wavelength conversion mechanism, which is usually produced by non-parallel mean flow effects due to short-scale streamwise variations in the mean flow. These streamwise gradients may arise from slow, viscous boundary-layer growth associated with the leading-edge region (Goldstein 1983, Hammerton & Kerschen 1996, 1997), or from localized regions farther downstream in the boundary layer, such as regions with sudden changes in surface geometry (Goldstein 1985, Choudhari and Kerschen 1990) or marginally separated regions (Goldstein, Leib & Cowley 1987). Additional background information on receptivity can be found in Goldstein & Hultgren (1989) and Kerschen (1990).

Leading-edge receptivity was first considered for the Blasius boundary layer on a flat plate (Goldstein 1983). A high Reynolds number asymptotic analysis was formulated for an incompressible, two-dimensional flow of free-stream speed U_∞, together with a small-amplitude time-harmonic perturbation of frequency ω, equivalent to the incompressible limit of an acoustic wave propagating parallel to the mean flow. Two streamwise regions enter the analysis, one region of $O(U_\infty/\omega)$, where the inviscid pressure field and slip velocity induced by the free-stream disturbance drives the unsteady motion in the boundary layer, and a second region farther downstream at distance $O((\nu\omega/U_\infty^2)^{-\frac{1}{3}} U_\infty/\omega)$, where the disturbance is governed by the triple-deck structure, corresponding to the high Reynolds number asymptotic form of the Orr-Sommerfeld equation (OSE) in the vicinity of the lower branch.

In the first region of Goldstein's analysis, assuming that the amplitude of the unsteady disturbances in the free-stream is small compared with the mean flow, the unsteady disturbance in the boundary layer is governed by the linearized unsteady boundary layer equation (LUBLE). Far downstream in the LUBLE region, the solution consists of a Stokes wave, and a set of asymptotic eigenfunctions that contain velocity but not pressure fluctuations. These asymptotic eigenfunctions are equivalent to those obtained by Lam &

Rott (1960, 1993) and Ackerberg & Phillips (1972). The asymptotic analysis for distances far downstream determines the form of the eigenfunctions, but not their coefficients C_i.

The wavelengths of the asymptotic eigenfunctions shorten progressively with distance downstream. Eventually, the self-induced pressure field associated with the displacement thickness of each asymptotic eigenfunction becomes significant, and the triple-deck structure replaces the LUBLE as the correct asymptotic approximation to the Navier-Stokes equation. The first asymptotic eigenfunction of the LUBLE matches on to the Tollmien-Schlichting wave solution of this triple-deck region. Thus, the form of the free-stream disturbance and the geometry close to the nose influence the amplitude of the Tollmien-Schlichting wave only through the coefficient C_1 of the first asymptotic eigenfunction. For this reason, C_1 is known as the 'receptivity coefficient'. The numerical value of the receptivity coefficient can not be determined by asymptotic methods. Instead it must be extracted from numerical solutions of the LUBLE, by comparison with the asymptotic form far downstream in the LUBLE. This was accomplished for the flat-plate case by Goldstein, Sockol & Sanz (1983) and Heinrich & Kerschen (1989).

The analysis of Goldstein for a flat plate was the first theoretical description of the fundamental mechanisms of leading-edge receptivity. However, aerodynamic bodies designed for subsonic flow generally have finite thickness distributions with a parabolic leading edge. Hammerton & Kerschen (1996, 1997) considered a thin, symmetric airfoil at zero angle of attack with a plane acoustic wave incident at arbitrary angle, and examined the influence of the leading-edge geometry of the body on receptivity. The structure of the development of the instability remains similar to that for a flat-plate; the asymptotic eigenfunctions of the LUBLE are modifications of the Lam-Rott eigenfunctions which take account of the effects of mean pressure gradient and surface curvature. Attention was focused on the variation of the receptivity level with the nose radius of the body and the incidence angle of the acoustic field. The radius of curvature of the leading-edge of the airfoil, r_n, enters the analysis as a Strouhal number, $S = \omega r_n / U_\infty$. The results revealed that, for disturbances parallel to the mean flow, a small increase in the receptivity for very small S is followed by a rapid decrease in the level of receptivity so that, when $S = 0.3$, the receptivity is reduced to approximately 15% of the flat-plate value. In addition, for unsteady disturbances propagating at an angle to the mean flow, the overall level of receptivity is dominated by the response to the component of unsteady slip velocity which is anti-symmetric about the leading-edge. Inclusion of thickness effects goes some way towards modeling experimental investigations (Saric, Wei, Rasmussen & Krutckoff 1995; Saric & White 1998) and allowing comparisons with related numerical simulations (Reed & Lyttle 1998). In wind tunnel tests reflections of acoustic waves from the side walls can lead to significant anti-symmetric flow about the leading edge (see Kerschen 1990 and Saric & White 1998).

In this chapter the receptivity of a cambered airfoil at an angle of attack to a mean flow is considered. The receptivity problem for this physical situation is considerably more intricate than the examples analyzed up to this time. First, there is receptivity associated with the mean stagnation point on the lower surface, as well as receptivity due to the strongly non-parallel flow around the leading edge. Moreover, at non-zero angles of attack a minimum appears in the steady wall shear on the upper surface. As the angle of attack of the airfoil is increased, the value of the minimum wall shear decreases until at some critical angle the minimum wall shear reaches zero, which for a two-dimensional flow corresponds to flow separation. Hence a regime exists where the angle of attack

is close to the critical angle and there is a region of marginal separation on the upper surface of the airfoil. Here the receptivity mechanism analyzed by Goldstein *et al* (1987) is relevant.

The structure of the chapter is as follows. In §4.2 a high Reynolds number asymptotic analysis ($\epsilon^6 = \nu\omega/U_c^2$; $\epsilon \ll 1$) is formulated for an incompressible, two-dimensional flow about a thin, cambered airfoil. In §4.2.1, the steady slip velocity on the airfoil surface is determined using thin-airfoil theory, followed in §4.2.2 by the derivation of the equation governing the unsteady boundary-layer flow in terms of suitable coordinates. Assuming that the unsteady perturbations in the free-stream are small, and letting $\epsilon \to 0$, the unsteady disturbances in the boundary layer are governed by the LUBLE.

The structure of the solution in the LUBLE region is analyzed in §4.3. When considering the subsequent development of instabilities in the boundary-layer flow, the asymptotic form of the unsteady solution far downstream in the LUBLE region is required. The derivation of the asymptotic form of both the steady and unsteady components of the solution is a necessary part of the presentation, but details are given in Appendices D and E instead of the body of the chapter in order to avoid interrupting the description of the evolution of the boundary-layer disturbance.

In §4.4, the inviscid pressure field and slip velocity produced by the interaction of a free-stream acoustic wave with an airfoil are determined, in order to allow calculation of the interaction between the free-stream and the boundary layer. The exact form of the unsteady slip velocity in the vicinity of the leading edge is determined by the global solution about the airfoil. This depends on the magnitude of the reduced acoustic frequency $k = \omega b/c$, where b is the airfoil semi-chord and c is the speed of sound. Here we present results for the limiting cases $k \ll 1$ and $k \gg 1$, when relatively simple expressions for the slip velocity can be obtained. The definition of the receptivity coefficient for this particular geometry is also provided. Finally in §4.5, numerical solutions of the steady boundary layer equation and the LUBLE are obtained, and compared with the asymptotic eigenfunctions of §4.3. This allows determination of the receptivity coefficient as a function of leading-edge geometry, airfoil shape and angle of attack, and of the characteristics of the free-stream acoustic wave.

4.2 Formulation

We consider a thin, cambered airfoil of chord $2b$ at an angle of attack $\hat{\alpha}$ to a uniform flow of speed U_∞. A plane acoustic wave of frequency ω, propagating at an angle θ, is assumed to be incident on the airfoil as illustrated in figure 4.1. Two-dimensional, low Mach number flow is considered. Since the Mach number is small, the mean flow can be analyzed using incompressible theory. For the unsteady component of the flow, most features of interest can also be analyzed using incompressible theory. The influence of compressibility on the unsteady component of the flow is discussed in §4.4. The Reynolds number is assumed large, so the flow field is inviscid and irrotational everywhere except in the vicinity of the airfoil surface. The behavior of the flow in the boundary layer adjacent to the airfoil surface depends crucially on the pressure gradient imposed by the outer inviscid flow. Therefore, relevant features of the inviscid mean flow are presented in §4.2.1. The equations governing the boundary-layer flow are formulated in §4.2.2.
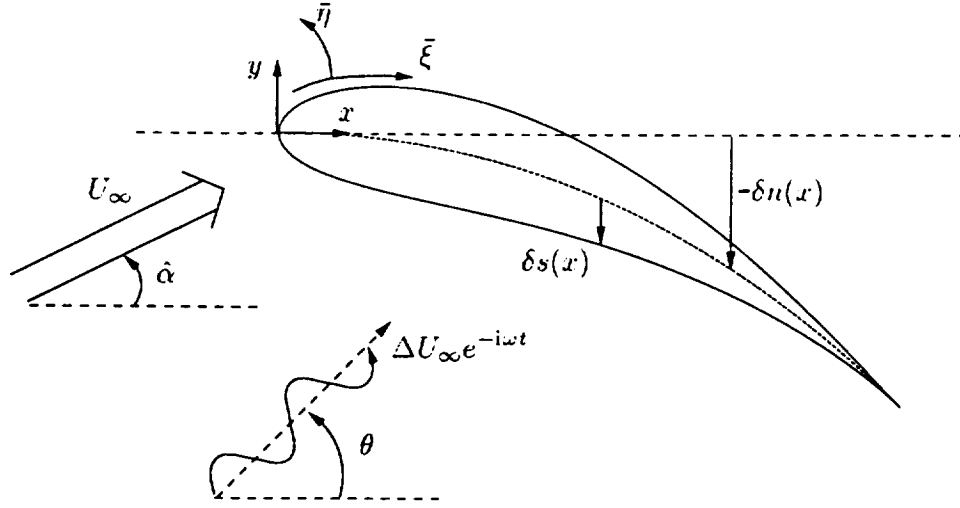
Figure 4.1: An illustration of the physical situation of interest: a thin, cambered airfoil of chord $2b$ is at angle $\hat{\alpha}$ to a uniform flow of speed U_∞, with a plane acoustic wave incident at an angle θ.

4.2.1 Inviscid Mean Flow

We introduce Cartesian coordinates (x, y) normalized by the airfoil semi-chord b, with the origin located at the airfoil leading edge and the x- and y-coordinate axes parallel and normal to the airfoil chord line at the leading edge, as illustrated in figure 4.1. This particular choice of coordinate system proves convenient for the present analysis, in which attention is focused on the leading-edge region. The camber and thickness of the airfoil are assumed of $O(\delta)$ where $\delta \ll 1$. Explicitly factoring out the scaling parameter δ, the airfoil surface is defined by

$$y = \delta(-n(x) \pm s(x)), \qquad 0 \le x \le 2, \tag{4.1}$$

where the $\pm$ sign applies on the upper and lower surface, respectively, and the camber and thickness functions $n(x)$ and $s(x)$ are defined in figure 4.1. The angle of attack $\hat{\alpha}$, measured with respect to the axes defined above, is also assumed to be small (to avoid separation) and to be comparable to the thickness and camber; hence we write $\hat{\alpha} = \delta\alpha$. The inviscid mean flow past the airfoil can then be calculated using thin-airfoil theory. Specifically, the no-penetration boundary condition on the upper and lower surfaces of the airfoil can be linearized and transferred to $y = 0^\pm$, respectively. The mean-flow perturbation due to the presence of the airfoil is found to have the y-components

$$U_\infty\delta(-\alpha + n'(x) \pm s'(x)) \qquad \text{on} \qquad 0 \le x \le 2, \quad y = 0^\pm, \tag{4.2}$$

where $n'(x)$ and $s'(x)$ denote the derivatives of these functions with respect to x. The mean slip velocity on the airfoil surface, U_s, immediately follows (Cheng & Rott 1954),

$$\frac{U_s(x)}{U_\infty} = 1 - \frac{\delta}{\pi}\left(\int_0^2 \frac{s'(x_1)}{x_1 - x}dx_1 + \left[\frac{2 - x}{x}\right]^{\frac{1}{2}}\int_0^2 \left[\frac{x_1}{2 - x_1}\right]^{\frac{1}{2}}\frac{n'(x_1) - \alpha}{x_1 - x}dx_1\right) + O(\delta^2). \tag{4.3}$$

49

A circulatory component has been included in (4.3), its magnitude fixed by the Kutta condition at the trailing edge.

The thin-airfoil expansion (4.3) is invalid in the vicinity of the leading edge, and must be supplemented by a local expansion. For an airfoil with a rounded leading edge of (dimensional) radius r_n, the small argument expansion of the thickness distribution has the form

$$s(x) = s_1 x^{1/2} + s_2 x + s_3 x^{3/2} + O(x^2) \qquad (4.4)$$

where $s_1 = (2r_n/\delta^2 b)^{1/2}$. The coefficient of the leading term in (4.4) must be $O(1)$, implying that $r_n = O(\delta^2 b)$. The airfoil nose radius r_n is the natural length scale in the leading-edge region. We therefore introduce a parabolic coordinate system $(\bar{\xi}, \bar{\eta})$ based on this length scale. The relationship between the (x, y) and $(\bar{\xi}, \bar{\eta})$ coordinates is

$$x + iy = \frac{1}{2}\frac{r_n}{b}\left[\left(\bar{\xi} + i\bar{\eta}\right)^2 + 1\right]. \qquad (4.5)$$

In terms of these new coordinates, the airfoil surface is given by $\bar{\eta} = 1 + \frac{1}{2}\delta s_2 \bar{\xi}^3/(1 + \bar{\xi}^2) + O(\delta^2)$. Thus, at leading order in the local coordinates, the airfoil surface is defined by the parabola $\bar{\eta} = 1$. The inviscid flow in the vicinity of the parabolic nose can be obtained in the form of a complex potential by means of conformal mappings, giving a slip velocity

$$U_s(\bar{\xi}) = U_e \left(\frac{\bar{\xi}}{(\bar{\xi}^2 + 1)^{1/2}} + \mu\frac{1}{(\bar{\xi}^2 + 1)^{1/2}}\right). \qquad (4.6)$$

The first term of (4.6) corresponds to symmetric flow past the nose, while the second term is an antisymmetric flow around the nose, from the lower surface to the upper, when the parameter μ is positive. The parameters U_e and μ in (4.6) are determined by matching with the thin-airfoil expression (4.3).

In order to match (4.3) and (4.6), the small-x behavior of (4.3) and the large-$\bar{\xi}$ behavior of (4.6) must be determined. For $x \ll 1$, (4.3) takes the form

$$\frac{U_s(x)}{U_\infty} = 1 + \frac{\delta}{\pi}\left(\pm\pi\alpha_e\sqrt{2}x^{-1/2} - s_2\ln x + \frac{s_1}{\sqrt{2}} + s_2\ln 2\right.$$
$$\left. - \int_0^2 \left[\frac{ds}{dx_1} - \frac{s_1}{2x_1^{1/2}} - s_2\right]\frac{dx_1}{x_1} + O(x^{1/2})\right) \qquad (4.7)$$

where α_e, the effective angle of attack for the leading-edge region taking into account the camber of the entire airfoil, is given by

$$\alpha_e = \alpha - \frac{1}{\pi}\int_0^2 \frac{n'(x)}{[x_1(2 - x_1)]^{1/2}}dx_1. \qquad (4.8)$$

For $\bar{\xi} \gg 1$, (4.6) takes the form $U_s(\bar{\xi}) = U_e + U_e\mu/\bar{\xi} + O(1/\bar{\xi}^2)$. The matching of the symmetric components of these expressions is identical to that discussed in chapter 2. For leading-edge shapes that contain a wedge component ($s_2 \neq 0$), the approximation (4.6) is valid only at $O(1)$ in the thickness parameter δ and the matching then shows that $U_e = U_\infty$. For leading-edge shapes, such as that of a Joukowski airfoil, where the even coefficients in (4.4) vanish, the leading-edge region is also parabolic at $O(\delta)$, and the matching then gives

$$U_e = U_\infty \left(1 + \frac{\delta}{\pi}\left[\frac{s_1}{\sqrt{2}} - \int_0^2 \left(\frac{ds}{dx} - \frac{s_1}{2x^{1/2}}\right)\frac{dx}{x}\right]\right). \qquad (4.9)$$

50

The $O(\delta)$ term in (4.9) is essentially a correction to the 'free-stream speed' in the local leading-edge region, due to the flow perturbation created by the thickness distribution of the entire airfoil. Next, matching of the antisymmetric components of the local and thin-airfoil expansions then gives the angle-of-attack parameter

$$\mu = 2\alpha_e \sqrt{\frac{\delta^2 b}{r_n}}, \qquad (4.10)$$

which is $O(1)$ since $r_n = O(\delta^2 b)$. The stagnation point on the lower surface is given by $\bar{\xi} = -\mu$, which corresponds to $x = 2(\delta\alpha_e)^2$, a familiar result for thin bodies.

4.2.2 Boundary-layer flow

The boundary-layer flow in the vicinity of the leading edge is also analyzed most conveniently in parabolic coordinates. For the mean boundary layer, the nose radius r_n remains the appropriate length scale in the streamwise direction. However, for the unsteady flow, a second streamwise length scale, U_e/ω, is also relevant. Specifically, Goldstein's (1983) analysis of leading-edge receptivity for the flat-plate boundary layer showed that the receptivity process takes place in a region where the distance from the leading edge is $O(U_e/\omega)$. To focus on this region, we introduce new coordinates,

$$\tilde{\xi} = S^{\frac{1}{2}}\bar{\xi}, \qquad \tilde{\eta} = S^{\frac{1}{2}}\bar{\eta}, \qquad (4.11)$$

where

$$S = \frac{\omega r_n}{U_e} \qquad (4.12)$$

is a Strouhal number based on the airfoil nose radius.

Since the Reynolds number is assumed large, viscosity is important only in a thin boundary layer adjacent to the body surface. To analyze the boundary-layer flow, we set

$$\tilde{\xi} = \xi, \qquad \tilde{\eta} - S^{\frac{1}{2}} = \epsilon^3 \eta, \qquad (4.13)$$

where the small parameter

$$\epsilon^6 = \frac{\nu\omega}{U_e^2} \ll 1 \qquad (4.14)$$

is the reciprocal of the Reynolds number based on the disturbance length scale U_e/ω. The analysis presented here considers the small-ϵ limit but with $S = O(1)$. The non-dimensional vorticity equation, expressed in terms of the streamfunction Ψ (which has been normalized by $\epsilon^3 U_e^2/\omega$), then becomes

$$\Psi_{\eta t} + \frac{\partial(\Psi_{\eta\eta}/H^2, \Psi)}{\partial(\xi, \eta)} - \frac{\Psi_{\eta\eta\eta}}{H^2} = \epsilon^6 \left(\frac{\Psi_{\eta\eta\xi\xi}}{H^2} + \left[\frac{\Psi_{\eta\eta}}{H^2}\right]_{\xi\xi} - \frac{\partial(\Psi_{\xi\xi}/H^2, \Psi)}{\partial(\xi, \eta)} - \Psi_{\xi\xi t} \right)$$
$$+ \epsilon^{12} \left[\frac{\Psi_{\xi\xi}}{H^2}\right]_{\xi\xi}, \qquad (4.15)$$

where $H = (\xi^2 + S)^{\frac{1}{2}}$. The streamfunction Ψ contains both the mean and time-dependent components of the flow. Equation (4.15) is exact, except for approximation of the metric coefficient $(\bar{\xi}^2 + \bar{\eta}^2)$ by H. The viscous flow satisfies the no-slip boundary conditions on the body surface,

$$\Psi = \Psi_\eta = 0, \qquad \text{on} \quad \eta = 0. \qquad (4.16)$$

51

At the outer edge of the boundary layer, the viscous flow matches to the inviscid slip velocity (non-dimensionalized by U_e),

$$H^{-1}\Psi_\eta \to \tilde{U}_s(\xi, t), \qquad \text{as} \quad \eta \to \infty. \tag{4.17}$$

For $O(1)$ values of ξ, the terms on the right-hand side of (4.15) can be neglected, leading to the unsteady boundary-layer equation. The unsteady component of the flow, a small perturbation to the mean flow, then satisfies the linearized unsteady boundary-layer equation (LUBLE). It is shown in §4.3 that the solution of the LUBLE contains components whose wavelengths progressively shorten with distance downstream. Thus, for the unsteady component of the flow, terms on the right-hand side of (4.15) become significant when $\xi = O(\epsilon^{-1})$, and the correct asymptotic approximation to (4.15) then takes on the triple-deck structure. The asymptotic matching of these two streamwise regions is discussed briefly at the end of §4.3.

4.3 Analysis of receptivity region

In this section, we consider the region of the boundary layer where the receptivity takes place. The streamwise length scale for this region is U_e/ω. Thus, the development of the viscous flow in this region is governed by the form of (4.15) corresponding to the limit $\epsilon \to 0$, $\xi = O(1)$. Subsequently, the behavior of this solution at large values of ξ will be considered, in anticipation of matching with the Orr–Sommerfeld region that exists farther downstream in the boundary layer. For $\xi = O(1)$ and $\epsilon \to 0$, terms on the right-hand side of (4.15) can be ignored. Integrating once with respect to η then gives the unsteady boundary-layer equation,

$$H^2\Psi_{\eta t} + (\Psi_\eta \Psi_{\xi\eta} - \Psi_{\eta\eta}\Psi_\xi) - \xi H^{-2}\Psi_\eta{}^2 - \Psi_{\eta\eta\eta} = -H^2 P_\xi, \tag{4.18}$$

where the pressure gradient $P_\xi(\xi, t)$ is obtained by matching to the outer (inviscid) flow,

$$P_\xi(\xi, t) = -H\frac{\partial \tilde{U}_s}{\partial t} - U_s\frac{\partial \tilde{U}_s}{\partial \xi}. \tag{4.19}$$

Up to this point our analysis has paralleled that of chapter 2, utilizing nearly the same notation. For the symmetric mean flow case considered by chapter 2, the unsteady boundary-layer region was analyzed using the streamwise coordinate ξ (which is based on the length scale U_e/ω). This allowed easy comparison with the flat-plate analysis of Goldstein (1983). However, for the non-zero angle-of-attack case considered here, no corresponding flat-plate analysis is possible because the boundary layer would separate at the leading edge. In addition, the presence of airfoil thickness, camber and angle-of-attack significantly complicates the algebra. The analysis of the mean flow is most naturally carried out in terms of a streamwise coordinate based on the nose radius r_n. Noting the parabolic nature of the governing equations, one can see that the mean-flow stagnation point is the natural origin for the streamwise coordinate. Thus we introduce the new streamwise coordinate,

$$w = \overline{\xi} + \mu = S^{-\frac{1}{2}}\xi + \mu, \tag{4.20}$$

where μ is the angle-of-attack parameter defined in (4.10). The mean-flow stagnation point is now given by $w = 0$, the nose corresponds to $w = \mu$ and w is scaled on the nose radius r_n rather than the disturbance length scale U_e/ω.

Because the mean flow is expressed most simply in terms of the streamwise coordinate w, it turns out that w is also the most convenient coordinate for analysis of the unsteady flow. Our analysis assumes $S = O(1)$, so that $w = O(1)$ also corresponds to $\xi = O(1)$. Later in this section we analyze the behavior of the solution for large ξ, in order to examine the development of the Lam–Rott asymptotic eigenfunctions ψ_i, and the eventual evolution of the first eigenfunction ψ_1 into the Tollmien–Schlichting wave when $\xi = O(1/\epsilon)$. This large-ξ analysis will be presented in terms of large w for algebraic simplicity, but we emphasize that it is the quantity $S^{1/2}w$ which is required to be large.

For typical values of the camber distribution and angle of attack, the mean aerodynamic loading parameter μ is usually positive. We examine the influence of mean aerodynamic loading on the receptivity for both surfaces of the airfoil. However, rather than considering the cases $w > 0$ (upper surface) and $w < 0$ (lower surface) separately, the analysis can be presented more concisely by considering w to be positive and taking $\mu > 0$ to give upper surface results and $\mu < 0$ for lower surface results.

For a cambered airfoil at non-zero angle-of-attack, the slip velocity is given in terms of the new coordinate w by

$$\tilde{U}_s(w, t) = \frac{w}{h} + \Delta\, u_s e^{-it}, \qquad (4.21)$$

where $h^2 = 1 + (w - \mu)^2$. Here the steady contribution $U_s = w/h$ follows from (4.6), while the time-dependent component $u_s(w)$ depends on the particular form of the free-stream disturbance, as discussed in §4.4. Since we are concerned only with small-amplitude free-stream disturbances, that is $\Delta \ll 1$, the steady and unsteady components of the flow field can be analyzed separately. Thus, the streamfunction within the boundary layer can be written in the corresponding form

$$\Psi(w, \eta) = S^{\frac{1}{2}} w \phi(w, \eta) + \Delta \psi(w, \eta) e^{-it}, \qquad (4.22)$$

where the factor $S^{\frac{1}{2}}w$ has been extracted from the mean component of the streamfunction in order to simplify the matching condition as $\eta \to \infty$. The steady boundary-layer flow then satisfies

$$\phi_{\eta\eta\eta} + \phi_{\eta\eta}\phi + w(\phi_{\eta\eta}\phi_w - \phi_\eta\phi_{\eta w}) - \beta(\phi_\eta{}^2 - 1) = 0, \qquad (4.23)$$

where the pressure gradient parameter $\beta(w; \mu)$ is given by

$$\beta = \frac{1 - \mu w + \mu^2}{h^2}, \qquad (4.24)$$

together with boundary conditions

$$\phi = \phi_\eta = 0 \quad \text{at} \quad \eta = 0 \quad \text{and} \quad \phi_\eta \to 1 \quad \text{as} \quad \eta \to \infty. \qquad (4.25)$$

The time-dependent component of the boundary-layer flow satisfies the linearized

unsteady boundary-layer equation (LUBLE),

$$
\left.\begin{array}{l}
\mathcal{F}(\psi) = S^{\frac{1}{2}}h^2\dfrac{\mathrm{d}p}{\mathrm{d}w}, \\[2ex]
\mathcal{F}(\psi) \equiv \psi_{\eta\eta\eta} + (\phi + w\phi_w)\psi_{\eta\eta} + \left(iSh^2 + \dfrac{w^2 - \mu^2 - 1}{h^2}\phi_\eta - w\phi_{\eta w}\right)\psi_\eta \\[2ex]
\qquad\qquad + w(\phi_{\eta\eta}\psi_w - \phi_\eta\psi_{\eta w}) \\[2ex]
\dfrac{\mathrm{d}p}{\mathrm{d}w} = \left(iSh - \dfrac{1 - \mu(w - \mu)}{h^3}\right)u_s - \dfrac{w}{h}\dfrac{\mathrm{d}u_s}{\mathrm{d}w},
\end{array}\right\} \qquad (4.26)
$$

with boundary conditions

$$
\psi = \psi_\eta = 0 \quad \text{at} \quad \eta = 0 \quad \text{and} \quad \psi_\eta \to S^{\frac{1}{2}}hu_s \quad \text{as} \quad \eta \to \infty. \qquad (4.27)
$$

These equations must be solved numerically for each value of S and μ, and for each different free-stream disturbance, although various simplifications arise as will be seen later. The numerical solutions are described in §4.5. However, as discussed in §4.1, we are primarily interested in the solution of these equations in the large-ξ (or large-w) limit, where a component of the solution to the LUBLE matches onto the Tollmien–Schlichting wave solution of the Orr–Sommerfeld equation. In the next two sub-sections, we develop large-w asymptotic expansions for $\phi(w, \eta)$ and $\psi(w, \eta)$.

4.3.1 Large w expansion of the steady boundary-layer equation

In order to determine the form of the asymptotic eigensolution of the LUBLE that matches onto the TS wave far downstream, it is found that the expansion of the mean flow must be determined up to, and including, terms of $O(w^{-3})$. The large-w expansion of β is

$$
\beta \sim -\frac{\mu}{w} + \frac{(1 - \mu^2)}{w^2} + \frac{\mu(3 - \mu^2)}{w^3} + O\left(\frac{1}{w^4}\right). \qquad (4.28)
$$

For $\mu > 0$ an adverse pressure gradient arises on the upper surface $(w > 0)$; this adverse pressure gradient decays to zero much more slowly than the favorable pressure gradient arising in the symmetric mean-flow case $(\mu = 0)$. Guided by the $\mu = 0$ case (Van Dyke 1964), we find that the asymptotic expansion of the mean flow far downstream is given by

$$
\phi(w, \eta) \sim F(\eta) + \frac{\mu p_1(\eta)}{w} + \frac{p_2(\eta)\log w^2}{w^2} + \frac{p_3(\eta)}{w^2} + \frac{\mu p_4(\eta)\log w^2}{w^3} + \frac{\mu p_5(\eta)}{w^3} + O\left(\frac{1}{w^{\gamma_2}}\right),
$$
$$(4.29)$$

where the fractional power $\gamma_2 = 3.774$ arises as an eigensolution (Libby & Fox 1963). Here $F(\eta)$ is the Blasius solution and the $p_i(\eta)$ are determined by the set of equations $\mathcal{L}_i(p_i) = d_i$, given in Appendix D. The parameter μ appears in the p_i. As for the symmetric mean-flow case described in chapter 2, the large-w asymptotic form of the mean flow is not fully determined by the local conditions far downstream. A coefficient $B_1(\mu)$ enters the $O(w^{-2})$ and $O(w^{-3})$ terms, the value of which is dependent on conditions close to the leading edge. Hence $B_1(\mu)$ must be determined by comparing the asymptotic form (4.29) with the numerical solution obtained by integrating (4.23) from the stagnation

point $w = 0$. The asymptotic form (4.29) for the mean flow is applicable to both the surfaces of the airfoil; typically $\mu > 0$ corresponds to the upper surface and $\mu < 0$ corresponds to the lower surface.

In order to determine the large-w solution for the unsteady component of the flow, the behavior of the mean flow close to the wall is required. From the results of Appendix D, this is given by

$$\phi \sim \frac{\eta^2 U_0'(w)}{2} + \frac{\eta^3 U_0''(w)}{6} - \frac{\eta^5 F_0''^2}{5!} + O(\frac{\eta^2}{w^{r_2}}, \frac{\eta^5}{w}) \qquad (4.30)$$

where

$$\begin{aligned}
U_0'(w) &= F_0'' \left(1 + \frac{\bar{\imath}_0}{w} + A_1\frac{\log w^2}{w^2} + \frac{B_1}{w^2} + \mu A_1\bar{h}_0\frac{\log w^2}{w^3} + \mu\frac{B_1\bar{h}_0 + \bar{\jmath}_0 + \mu^2\bar{k}_0}{w^3}\right), \\
U_0''(w) &= \frac{\mu}{w} + \frac{\mu^2 - 1}{w^2} + \frac{\mu(\mu^2 - 3)}{w^3}.
\end{aligned} \right\} \qquad (4.31)$$

The functions $U_0'(w)$ and $U_0''(w)$ are the asymptotic expansions of the shear stress and the curvature of the mean boundary-layer profile at the wall, accurate to $O(w^{-3})$. The numerical values of the constants F_0'', A_1, $\bar{h}_0$, $\bar{\imath}_0$, $\bar{\jmath}_0$ and $\bar{k}_0$ are given in Appendix D. Numerical results for $B_1(\mu)$, obtained by comparing the numerical solution of (4.23) with the asymptotic form (4.29), are presented in §4.5.

4.3.2 Large $S^{1/2}w$ expansion of the linearized unsteady boundary-layer equation

We next consider the evolution of the unsteady component of the flow, which is governed by (4.26). As in the symmetric mean-flow case considered in chapter 2, far downstream in the LUBLE region ($S^{1/2}w \gg 1$) the unsteady component of the flow consists of a particular solution, ψ_p, determined entirely by the local conditions far downstream, together with a set of asymptotic eigenfunctions,

$$\psi(w, \eta; S, \mu) = \psi_p(w, \eta; S, \mu) + \sum_i C_i(S, \mu)\psi_i(w, \eta; S, \mu). \qquad (4.32)$$

The particular solution is a generalization of the classical Stokes layer solution, driven by the local value of the unsteady pressure gradient (4.26). The asymptotic eigenfunctions ψ_i are generalizations of the Lam–Rott eigenfunctions (Lam & Rott 1960), taking account of the non-Blasius mean flow. A second set of asymptotic eigenfunctions for the LUBLE were derived by Brown and Stewartson, but their relationship to Tollmien-Schlichting wave development has not been established. The eigenfunctions are 'asymptotic' because they exist only for $S^{1/2}w \gg 1$, where the mean flow takes on a slowly varying character. The ψ_i depend on the mean-flow characteristics far downstream, but are independent of the unsteady free-stream disturbance in the downstream region. The coefficients C_i of the asymptotic eigenfunctions are determined by the characteristics of the unsteady free-stream disturbance and the mean boundary-layer flow in the region nearer the leading edge where $S^{1/2}w = O(1)$. One of the asymptotic eigenfunctions, which we label ψ_1, matches on to the growing Tollmien–Schlichting wave in the Orr–Sommerfeld region farther downstream, where $S^{1/2}w = O(1/\epsilon)$. It is only through the receptivity coefficient

C_1 that the unsteady free-stream disturbance influences the amplitude of the Tollmien-Schlichting wave. In the remainder of this chapter, most attention is focused on this particular eigenfunction and on its coefficient C_1.

The form of the general asymptotic eigenfunction ψ_i is obtained in Appendix E. The asymptotic eigenfunctions have a two-layer structure, with a new inner layer of width $\eta = O(S^{-1/2}w^{-1})$. The leading-order expression for the general eigenfunction ψ_i is given by

$$
\psi_i^{(0)} = \begin{cases} \dfrac{F_0'' \rho_i^{\frac{1}{2}} e^{-\frac{1}{4}i\pi}}{\int_{-\rho_i}^{\infty} \mathrm{Ai}(z)dz} \left(\dfrac{Sw^2}{2}\right)^{\tau_i} \exp(T_i^{(0)}(w)) f_i^{(0)}(n), & n = S^{\frac{1}{2}} w\eta = O(1) \\[3mm] wS^{\frac{1}{2}} \left(\dfrac{w^2 S}{2}\right)^{\tau_i} \exp(T_i^{(0)}) F'(\eta), & \eta = O(1) \end{cases}
\tag{4.33}
$$

where ρ_i is the i-th root of $\mathrm{Ai}'(-\rho) = 0$, and τ_i, $T_i^{(0)}(w)$ and $f_i^{(0)}(n)$ are given by (E.20), (E.21) and (E.30), respectively.

In the next section, numerical solutions for the LUBLE are compared to the asymptotic eigenfunction ψ_1 in order to extract values of the receptivity coefficient C_1. The two most convenient points of comparison are the unsteady component of the wall shear, $\psi_{\eta\eta}(\eta = 0)$, and the oscillating boundary-layer thickness which is related to the value of the streamfunction far from the wall, $\psi(\eta \to \infty)$. For the first eigensolution, $\rho_1 = 1.01879$ and (4.33) gives

$$
\psi_1''(\eta = 0) \sim 0.4356(1 + i) \left(\frac{Sw^2}{2}\right)^{\tau_1 + 1} \exp(T_1^{(0)}(w)) \left[1 + O\left(w^{-\gamma_2 + 3}\right)\right], \tag{4.34}
$$

$$
\psi_1(\eta \to \infty) \sim wS^{\frac{1}{2}} \left(\frac{w^2 S}{2}\right)^{\tau_1} \exp(T_1^{(0)}(w)) \left[1 + O\left(w^{-\gamma_2 + 3}\right)\right], \tag{4.35}
$$

with

$$
\tau_1 = -0.6921 + 1.9878(1 - 6.182\mu^2)iS \tag{4.36}
$$

The exponent for the first neglected term in (4.34) and (4.35) is $-\gamma_2 + 3 = -0.774$. This term is followed by a sequence of closely-spaced correction terms of $O(w^{-1}\ln^2 w)$, $O(w^{-1}\ln w)$ and $O(w^{-1})$, as can be seen from the analysis presented in Appendix E.

Before proceeding to numerical solutions of (4.26), we first consider the validity of the LUBLE. While the eigenfunctions obtained here are uniformly valid solutions for the LUBLE as $\xi \to \infty$, they are not uniformly valid large-ξ solutions of the full equations governing the development of the viscous flow. Since $T \propto \xi^3$ at leading order, the wavelengths of the eigenfunctions decrease with distance downstream, increasing the importance of terms involving streamwise derivatives. When $\xi = O(1/\epsilon)$, terms on the right-hand side of (4.15), which were neglected in forming the LUBLE, now become significant. An irrotational layer outside the mean boundary layer, driven by the oscillating displacement thickness of the eigenfunction, must then be considered, and the pressure gradient imposed by the motion in this outer layer appears in the leading-order equations governing the wall layer. This coupled viscous–inviscid interaction has the triple-deck structure, corresponding to the small-ϵ asymptotic approximation to the Orr–Sommerfeld equation in the vicinity of the lower branch. A complete treatment of the linear development of

the instability wave would require an asymptotic solution for the Tollmien–Schlichting wave of the Orr–Sommerfeld equation, taking account of the mean pressure-gradient distribution on the airfoil. However, for $O(1)$ values of S, with ϵ and δ small quantities of the same order, the Orr–Sommerfeld region is influenced by the full airfoil camber and thickness distributions, necessitating a general development that does not seem justified in the present context.

In this chapter we restrict ourselves to examining only the receptivity process, and the remainder of the chapter is concerned with determining the receptivity coefficient C_1 as a function of the nose radius parameter S, the aerodynamic loading parameter μ, and the characteristics of the free-stream disturbance. This is accomplished by comparing numerical solutions with the asymptotic solutions obtained above.

4.4 Free-stream Disturbances

In order to calculate the unsteady flow in the boundary layer, the inviscid flow field which drives the unsteady motion in the boundary layer must be determined. In this section we consider the inviscid flow field produced by the interaction of a free-stream acoustic wave with the airfoil. The acoustic wave is assumed to be incident on the airfoil at an angle θ with respect to the airfoil chord, as illustrated in figure 1. The slip velocity and surface pressure fields generated by this interaction drive the unsteady motion in the boundary layer, leading to the generation of a Tollmien–Schlichting wave. Since the outer inviscid flow is irrotational, the unsteady pressure field is easily related to the unsteady velocity field. Thus, we present results for the unsteady slip velocity in the leading-edge region.

For a low Mach number flow, the acoustic wavelength $2\pi c/\omega$ is long compared to the hydrodynamic length scale U_e/ω. Thus, outside the boundary layer, the unsteady flow in the vicinity of the leading edge is incompressible and irrotational. Potential flow theory then shows that this local flow has the form

$$u_s(w) = \kappa_s(\theta)\frac{w-\mu}{h} + \kappa_a(\theta)S^{-\frac{1}{2}}\frac{1}{h} \tag{4.37}$$

where $h^2 = 1 + (w - \mu)^2$. Noting that $w - \mu = \bar{\xi}$, the parabolic coordinate with origin at the leading edge, it is seen that $(w - \mu)/h$ and $1/h$ correspond to purely symmetric and anti-symmetric flow about the leading edge, respectively. The coefficients κ_s and κ_a multiplying these eigenfunctions are independent of the nose geometry, but depend on the free-stream disturbance, being determined by global features of the unsteady flow. The $S^{-\frac{1}{2}}$ factor is included in the anti-symmetric term in order to retain consistency of notation with chapter 2. Expressions for the coefficients κ_s and κ_a can then be taken directly from chapter 2.

The nature of the unsteady interaction of the acoustic wave with the airfoil depends upon the magnitude of the acoustic reduced frequency $k = \omega b/c$, where c is the speed of sound in the undisturbed medium. For extremely low Mach numbers, the acoustic wavelength is long not only compared to the hydrodynamic length scale, U_e/ω, but also compared to the airfoil chord, i.e. $k \ll 1$. The unsteady interaction of the acoustic wave with the airfoil can then be analyzed using the classical unsteady airfoil theory for incompressible flow, giving

$$\kappa_s = \cos\theta, \qquad \kappa_a = a^{\frac{1}{2}}\sin\theta \tag{4.38}$$

where $a = \omega b/U_e$ is the aerodynamic reduced frequency. If we consider the other limiting case, $\omega b/c \gg 1$, the acoustic wavelength is then short compared to the airfoil chord, and the interaction of the acoustic wave with the leading edge can be analyzed by taking the airfoil chord to be semi-infinite. As in the first case, on the scale of the acoustic wavelength, the airfoil appears at leading order as a zero-thickness plate and the problem reduces to the classical Sommerfeld diffraction problem. Matching to the local solution in the vicinity of the leading edge, then gives

$$\kappa_s = \cos\theta, \qquad \kappa_a = \frac{2e^{-\frac{1}{4}i\pi}}{(\pi M_e)^{\frac{1}{2}}}\sin\tfrac{1}{2}\theta, \qquad (4.39)$$

where $M_e = U_e/c$ is the Mach number of the mean flow, which has been assumed small.

As described in chapter 2, writing $\psi = \kappa_s\psi_s + \kappa_a\psi_a$, and substituting into (4.26), it follows that the receptivity coefficient for the upper surface is given by

$$C_1 = \kappa_s(\theta)\, C_s(S,\mu) + \kappa_a(\theta)\, C_a(S,\mu), \qquad (4.40)$$

where C_s and C_a are extracted from the solutions of

$$\left. \begin{aligned} \mathcal{F}(\psi_s) &= S^{\frac{1}{2}}\left(iSh^2(w-\mu) + \frac{\mu - 2w + \mu(w-\mu)^2}{h^2}\right) \\ \mathcal{F}(\psi_a) &= iSh^2 - \frac{1+\mu^2 - w^2}{h^2} \end{aligned} \right\} \qquad (4.41)$$

respectively, with $\mathcal{F}$ defined in (4.26). Here C_s is a measure of the receptivity due to that component of the free-stream disturbance which leads to symmetric flow in the vicinity of the leading edge, and C_a is a measure of the receptivity arising from that component of the free-stream disturbance which leads to anti-symmetric flow about the leading edge.

The separation into components of the free-stream disturbance which are symmetric and anti-symmetric about the leading edge is a natural choice for consideration of airfoil thickness effects in the absence of aerodynamic loading, since in this case the symmetric and anti-symmetric components exhibit quite different dependence on the nose radius parameter $S = \omega r_n/U_e$. Specifically, when $\mu = 0$, the symmetric component of the slip velocity (4.37) varies monotonically from zero at $\bar{\xi} = 0$ to 1 as $\bar{\xi} \to \infty$, for all values of S. In contrast, for the anti-symmetric component of (4.37), the magnitude of the slip velocity near the leading edge is proportional to $S^{-1/2}$ and hence becomes large when the nose radius is small, due to flow around the 'sharp' edge. The mean flow stagnation point is at $\bar{\xi} = 0$ when $\mu = 0$, so that this difference in behavior is also reflected in the initial conditions for the numerical solutions of (4.41) for ψ_s and ψ_a. The behavior of the corresponding receptivity coefficients, $C_s(S,0)$ and $C_a(S,0)$, was discussed in chapter 2.

When aerodynamic loading and airfoil thickness effects are combined, the situation is more complex. The mean flow stagnation point is then at $\bar{\xi} = -\mu$ (or $w = 0$), so that both components of (4.37) have a finite unsteady slip velocity across the stagnation point where the solutions of (4.41) are started. In this case, an alternative separation of the unsteady slip velocity into components that are locally symmetric and anti-symmetric about the mean flow stagnation point can be considered. This takes the form

$$u_s = \kappa_s\frac{w}{h} + (\kappa_a - \mu S^{\frac{1}{2}}\kappa_s)\frac{1}{S^{\frac{1}{2}}h}, \qquad (4.42)$$

58

where the first component vanishes at the mean flow stagnation point while the second component is finite. The corresponding decomposition of the receptivity coefficient is

$$C_1 = \kappa_s C_{sSP} + (\kappa_a - \mu S^{\frac{1}{2}} \kappa_s) C_{aSP}, \tag{4.43}$$

where C_{sSP} and C_{aSP} are extracted from the numerical solutions of

$$\left.\begin{aligned}
\mathcal{F}(\psi_{sSP}) &= S^{\frac{1}{2}} w \left(iSh^2 - \frac{2(1 + \mu(\mu - w))}{h^2} \right) \\
\mathcal{F}(\psi_{aSP}) &= iSh^2 - \frac{1 + \mu^2 - w^2}{h^2}
\end{aligned}\right\}. \tag{4.44}$$

Of course, the symmetry and anti-symmetry about the mean flow stagnation point of the two components of the slip velocity (4.42) is only a local property, since h is not a symmetric function of w. However, for large values of S, the region of receptivity should be concentrated near the stagnation point, so that one might expect the differences in the local characteristics of these two components of slip velocity to be reflected in differences in the behavior of the corresponding receptivity coefficients, C_{sSP} and C_{aSP}. This is explored in the next section.

The two sets of Receptivity Coefficients are related by

$$C_s = C_{sSP} - \mu S^{\frac{1}{2}} C_{aSP}, \qquad C_a = C_{aSP}. \tag{4.45}$$

In the numerical computations, it proves convenient to solve (4.44) for ψ_{sSP} and ψ_{aSP}, thereby obtaining C_{sSP} and C_{aSP}, and to calculate C_s and C_a from (4.45). In the next section, the variation of the receptivity coefficients with the angle-of-attack parameter μ and the nose-radius parameter S is investigated numerically.

4.5 Numerical Results

In §4.3, generalizations of the Lam–Rott asymptotic eigenfunctions were obtained, taking account of the pressure gradient due to leading-edge thickness and mean aerodynamic loading. The asymptotic analysis determines the form of these eigenfunctions, but not their coefficients C_i. The coefficients are determined by the characteristics of the free-stream disturbance in the LUBLE region, $\xi = O(1)$. The first of these eigenfunctions is the precursor of the Tollmien–Schlichting wave. Thus, the free-stream disturbances influence the amplitude of the Tollmien–Schlichting wave only through the coefficient C_1. It appears that the receptivity coefficient C_1 for a particular free-stream disturbance can be determined only by numerically solving the LUBLE over the full range of ξ and examining the behavior for large ξ.

Numerical solutions are required for both the mean flow, governed by the nonlinear partial differential equation (4.23), and the linearized disturbance, governed by the LUBLE (4.26). For convenience, the numerical solutions are computed in terms of the variable w rather than ξ (see (4.20)). Since the governing equations are parabolic, the solutions were computed by marching away from the mean flow stagnation point ($w = 0$) using a Keller Box scheme (Keller & Cebeci 1970). The initial conditions at $w = 0$ correspond to the steady Hiemenz flow and its quasi-steady linear perturbation. As noted earlier, in order to consider receptivity on the upper and lower surfaces of an airfoil at a

59

positive angle of attack where the stagnation point lies on the lower surface, it is more convenient to consider $w > 0$ throughout and take $\mu > 0$ for the upper surface and $\mu < 0$ for the lower surface.

4.5.1 Mean flow

The development of the mean flow is controlled by the mean pressure gradient parameter,

$$\beta = \frac{1 - \mu w + \mu^2}{1 + (w - \mu)^2}. \tag{4.46}$$

The pressure gradient parameter is plotted as a function of w for three values of μ in figure 4.2. For $\mu = 0$, the pressure gradient is everywhere favorable, falling off monotonically away from its stagnation point value ($\beta = 1$) and approaching zero as w^{-2} far downstream. The behavior for negative w (the lower surface) is identical to that for positive w. When aerodynamic loading is introduced, the magnitude of the favorable pressure gradient along the upper surface is increased in the region from the stagnation point ($w = 0$) to the nose ($w = \mu$). The pressure gradient parameter then falls rapidly to zero at $w = \mu + \mu^{-1}$, and the pressure gradient is adverse for all locations farther downstream. The adverse pressure gradient decays to zero more slowly with downstream distance, becoming proportional to w^{-1} far downstream. In contrast to the complicated behavior of the pressure gradient on the upper surface in the presence of aerodynamic loading, the pressure gradient on the lower surface ($w < 0$) remains everywhere favorable. However, when μ is non-zero the pressure gradient on the lower surface decays only as $|w|^{-1}$ for large distances, and the magnitude of the pressure gradient increases with μ.

As the aerodynamic loading parameter is increased, the position of the minimum wall shear moves towards the nose (figure 4.3a), at the same time as the magnitude of the minimum wall shear decreases (figure 4.3b). For steady two-dimensional flows, zero wall shear corresponds to boundary-layer separation. From Ruban (1982) and Stewartson, Smith & Kaups (1982), the minimum wall shear close to the critical angle of attack is given by

$$\phi_{\eta\eta}(w_m, \eta = 0) \propto (\mu_c - \mu)^{\frac{1}{2}}.$$

Fitting this behavior to the curve in figure 4.3(b) suggests that separation occurs at $\mu_c \approx 1.15$. More accurate determination of separation criteria would require an improved numerical scheme, since the current method breaks down near the onset of flow reversal.

The coefficient $B_1(\mu)$, which appears in the functions $p_3(\eta)$ and $p_5(\eta)$ arising in the large-w asymptotic form of the mean flow (4.29), is undetermined by the asymptotic analysis. To determine $B_1(\mu)$, the wall shear $\phi_{\eta\eta}(w, 0)$ predicted by the asymptotic expansion (4.29) is compared with the wall shear obtained by numerical solution of (4.23), for each value of μ considered. In fact it proves necessary to modify (4.23) and solve for $\phi(w, \eta) - F(\eta)$ in order to obtain the required accuracy when extrapolating for B_1 in the large-w limit. In figure 4.4, it is seen that $B_1(0) \approx 2.08$ and that $B_1(\mu)$ increases approximately linearly with μ, for $-0.8 < \mu < 0.8$, before decreasing for $\mu > 0.9$. The value of B_1 is related to the 'virtual origin' of the boundary layer, as can be seen by noting that the function $\eta F' - F$ which B_1 multiplies in p_3 corresponds to the first eigensolution of Libby & Fox (1963). Their first eigensolution is the streamwise derivative of the streamfunction for the Blasius boundary layer. The value $B_1(0)$ relates to a shift of virtual origin due to the favorable pressure gradient on the nose of the parabola in the
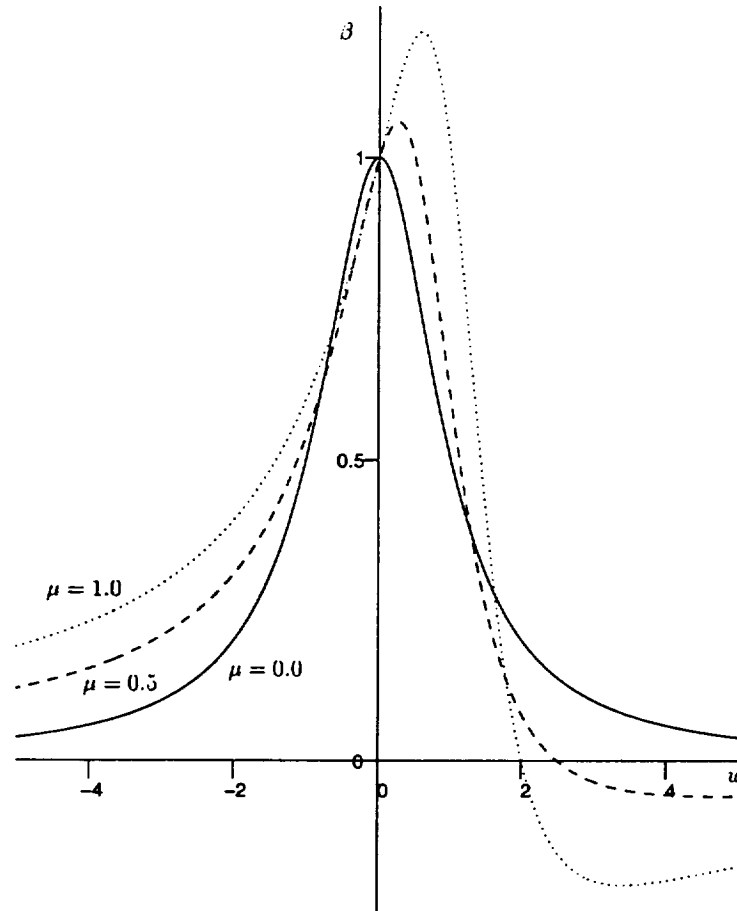
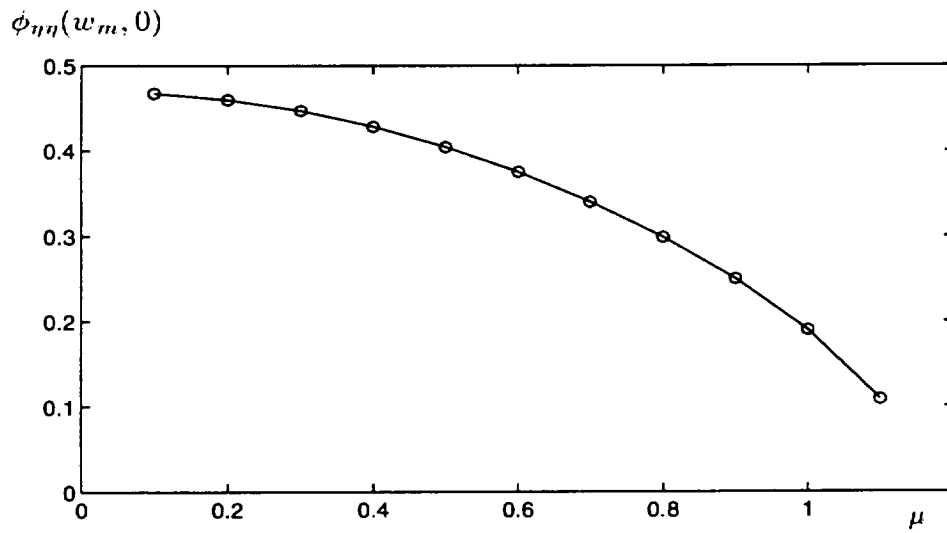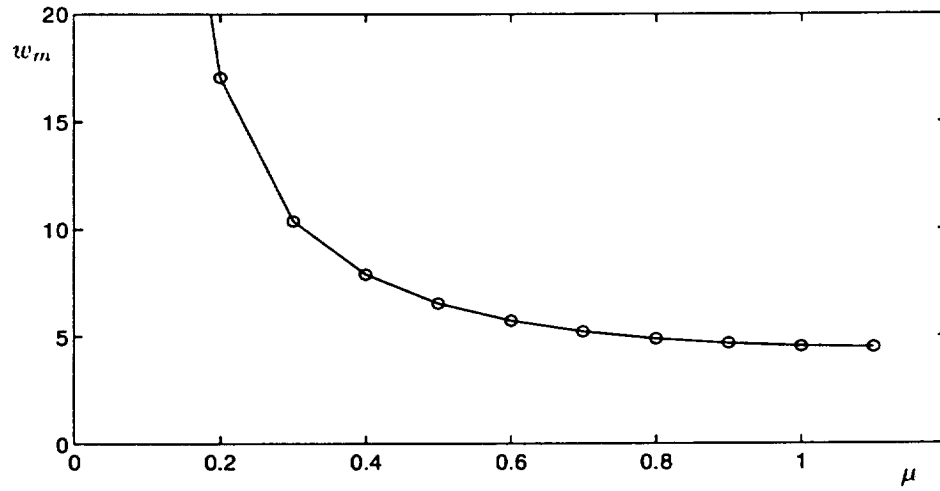Figure 4.2: Streamwise variation of the mean pressure gradient parameter, $\beta(w)$, for $\mu = 0.0, 0.5, 1.0$.

Figure 4.3: Effect of aerodynamic loading parameter on the wall shear: (a) Position of minimum wall shear, w_m; (b) Magnitude of minimum wall shear, $\phi_{\eta\eta}(w_m, \eta = 0)$.
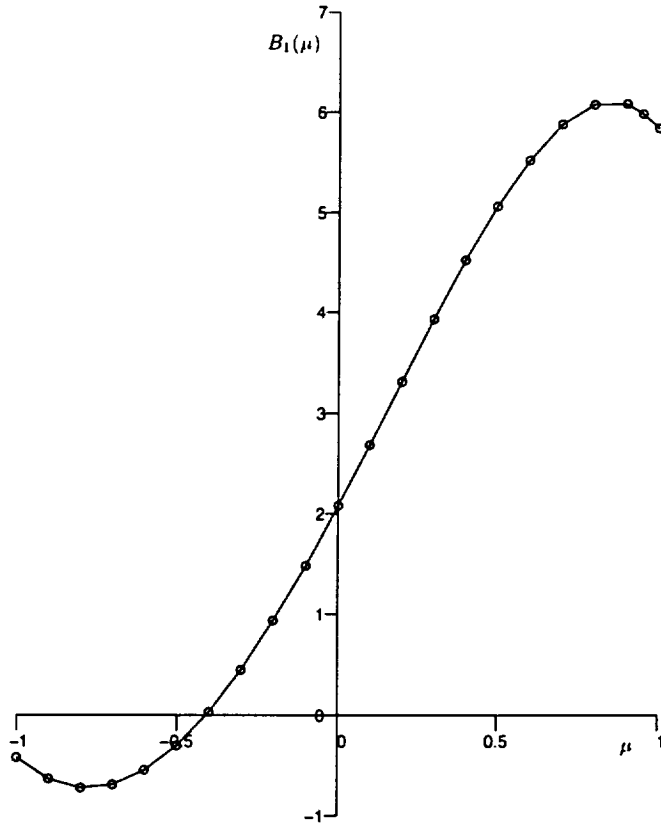
Figure 4.4: Computed values of $B_1(\mu)$, the coefficient appearing in the expansion of the base flow far downstream (4.29).

absence of aerodynamic loading; the dependence on μ relates to an additional shift of the virtual origin in the presence of aerodynamic loading.

4.5.2 Unsteady flow

The value of the Receptivity Coefficient $C_1(S, \mu)$, for a particular free-stream disturbance, is obtained by comparing numerical solutions of the LUBLE to the asymptotic forms (4.34) and (4.35).

The method used to obtain numerical values for C_s and C_a is described in chapter 2. For real w, the real part of $T_i^{(0)}(w)$ is negative. Thus, the asymptotic eigenfunctions (4.33) decay exponentially with downstream distance, while the particular solution ψ_p remains $O(1)$. In addition, the eigenfunctions are inverse ordered, so that the function $\psi_1$whose coefficient is desired decays exponentially faster than all the other eigenfunctions. To circumvent these difficulties, the streamwise integration is extended into the complex plane in order to make the first asymptotic eigenfunction dominant. Choosing $-5\pi/12 <$ $\arg w < -\pi/12$, the first eigenfunction becomes exponentially large compared to the other components of the unsteady boundary layer solution. However, the pressure gradient parameter β, defined by (4.24), has first-order poles at $w = \mu \pm i$. Thus for larger values of μ, $\arg w$ must be chosen with care in order to avoid an integration path which passes close to the singularity at $w = \mu - i$. For all the values of μ considered, integration

was performed for arg $w = -0.1\pi$ and arg $w = -0.15\pi$, while for smaller values of μ, results for arg $w = -0.2\pi$ and arg $w = -0.25\pi$ were also obtained. For these choices of arg w, the solution ψ grows exponentially with $|w|$. To avoid difficulties associated with the rapid growth of ψ as a function of $|w|$, in our numerical scheme we solve for $f = \psi \exp(-T_1^{(0)})$ rather than ψ. This allows the numerical solution to be continued much farther downstream while retaining accuracy (Heinrich & Kerschen, 1989).

Using the wall shear (4.34) as the basis for comparison, we define

$$C(\mu, S, w) = \frac{f''_{\text{Num}}(\eta = 0)}{f''_0}, \qquad (4.47)$$

where $f''_0 = 0.4356(1 + i)\,(Sw^2/2)^{\tau_1+1}$. Since the argument of w was chosen so that the first asymptotic eigenfunction dominates other components of the solution when $w \gg 1$, $f \sim C_1\psi_1 \exp(-T_1^{(0)})$ and hence

$$C \sim C_1 \left[1 + c_1\frac{1}{w^{0.774}} + c_2\frac{\ln^2 w}{w} + c_3\frac{\ln w}{w} + c_4\frac{1}{w} + \ldots \right] \qquad \text{as} \qquad w \to \infty. \qquad (4.48)$$

The value of $C_1(\mu, S)$ is then obtained by extrapolation. However, for the larger values of μ and S considered, a small error in the computed value of B_1 leads to a large error in $C(\mu, S, w)$ for $w \gg 1$, and hence limits the accuracy of the extrapolated value of C_1. In the analysis of chapter 2 for a symmetric airfoil in the absence of aerodynamic loading ($\mu = 0$), arg $w = -0.25\pi$ was used throughout. With this particular choice, any error in the extrapolated value of $|C_1|$ due to inaccuracy in the numerically determined value of B_1 is eliminated. Clearly this advantage is lost in the present study. However, C_1 should be independent of the value of arg w used in the numerical integration. By using two different values of arg w in the present analysis, any significant error due to inaccurate determination of B_1 should be readily identifiable. Unfortunately, for the larger values of μ and S considered, there is still uncertainty in the numerical value of C_1 obtained by extrapolation. For $\mu > 0.9$, the relative error may be as large as 25%.

In figure 4.5, the moduli of the receptivity coefficients, $|C_s|$ and $|C_a|$, for free-stream disturbances symmetric and anti-symmetric about the nose of the body, respectively, are plotted as a function of the aerodynamic loading parameter μ. Results are presented for two Strouhal numbers, $S = 0.1$ and $S = 0.3$. The overall patterns of the variation with the aerodynamic loading parameter μ are qualitatively similar for $|C_s|$ and $|C_a|$. However, the receptivity levels for anti-symmetric forcing are somewhat larger than those for symmetric forcing. As the aerodynamic loading parameter is increased from zero, the receptivity level on the upper surface ($\mu > 0$) decreases until $\mu \approx 0.7$. The receptivity then increases to a local maximum in the vicinity of $\mu \approx 0.9$, with a subsequent decrease in receptivity level as μ is increased further. The quantitative accuracy of the receptivity coefficient for values of μ beyond 0.9 is uncertain, however. As explained earlier, results close to the critical condition for boundary layer separation are prone to inaccuracies, due to difficulties in the extrapolation to large values of w, especially at higher values S. A further difficulty is the long downstream distance required for the boundary layer to recover from the region of low wall shear induced by the strong adverse pressure gradient just downstream of the nose.

The variations in both $|C_s|$ and $|C_a|$ as a function of μ are much larger at $S = 0.3$ than at $S = 0.1$. For $S = 0.3$, the receptivity levels on the upper surface drop significantly
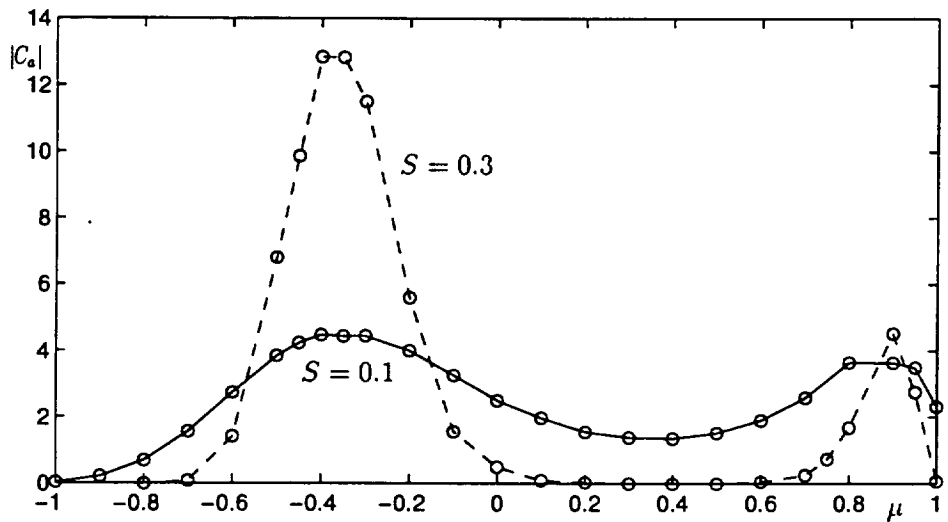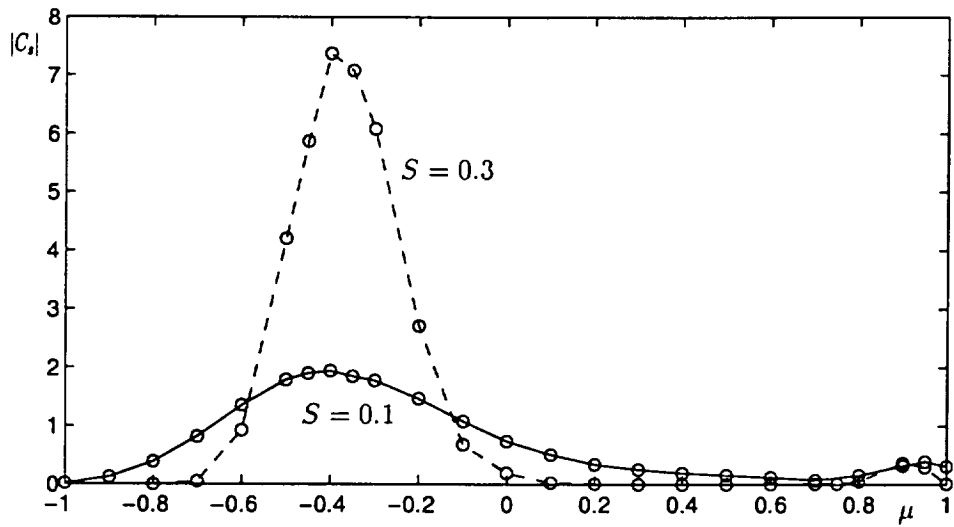
Figure 4.5: Variation of the magnitude of the receptivity coefficient as a function of the aerodynamic loading parameter μ, for two Strouhal numbers, S = 0.1 and 0.3. (a) Receptivity due to the free-stream disturbance component symmetric about the nose, $|C_s|$; (b) receptivity due to the free-stream disturbance component anti-symmetric about the nose, $|C_a|$.

for modest values of aerodynamic loading. Both $|C_s|$ and $|C_a|$ are less than 0.02 in the region $0.2 < \mu < 0.6$. (It is not possible to provide precise values in this region, because the errors that arise in extrapolation are absolute rather than relative.) The subsequent rise in receptivity level near $\mu \approx 0.9$ is particularly striking for the case of anti-symmetric forcing with $S = 0.3$, where $|C_a|$ exceeds 4.

On the lower surface of the airfoil ($\mu < 0$), the receptivity coefficients increase as aerodynamic loading is introduced, to a global maximum in the vicinity of $\mu \approx -0.4$. The receptivity coefficients then decrease toward zero as μ approaches -1. For negative μ, the value of the receptivity coefficient can be extracted from the computational results with a good degree of accuracy, since the pressure gradient is everywhere favorable and decays monotonically to zero, with no region of low wall shear.

The presence of aerodynamic loading adds significant complexity to the development of the unsteady flow, especially on the upper surface where the boundary layer first experiences a rapid acceleration, followed by a rapid deceleration and then a slow recovery. Thus it is difficult to provide a simple explanation for the dependence of the receptivity coefficient on the aerodynamic loading parameter. For the symmetric mean flow case ($\mu = 0$) considered in chapter 2, the mean pressure gradient is everywhere favorable, monotonically decreasing from its maximum value at the stagnation point to zero far downstream as seen in figure 4.2. An increase of the leading-edge nose radius (or Strouhal number) was found to decrease the receptivity coefficient. As a speculative explanation of this behavior, it was suggested that a favorable pressure gradient in the region where the receptivity occurs tends to reduce the receptivity level. At larger values of S, the region $\xi = O(1)$ where the receptivity occurs is concentrated closer to the airfoil nose, in the region of higher favorable pressure gradient. Hence, the decrease in receptivity for increasing S found in chapter 2 is consistent with this explanation.

However, certain features of the results presented in figure 4.5 are inconsistent with this simple explanation. One feature which cannot be explained in this way is the large positive peak in receptivity level which occurs on the lower surface at $\mu \approx -0.4$. It can be seen from figure 4.2 that the pressure gradient is negative everywhere on the lower surface, and that except for a small region very near the stagnation point, the magnitude of the pressure gradient increases monotonically with $|\mu|$. Thus, if the speculative explanation discussed above were valid, one would expect the receptivity coefficient to decrease monotonically with $|\mu|$ in the region $\mu < 0$. A second feature which requires further explanation is the rise in receptivity level in the vicinity of $\mu \approx 0.9$, followed by a subsequent decrease for larger values of μ. We address this latter feature first.

As discussed in §4.1, receptivity comes about through the interaction of free-stream disturbances with short-scale streamwise gradients in the boundary layer. In the leading-edge mechanism, the receptivity is concentrated in a region of length $O(U_e/\omega)$ extending downstream from the mean flow stagnation point. However, for values of μ approaching the critical value for the onset of separation, $\mu_c \approx 1.15$, additional short-scale streamwise variations develop in the mean flow in the vicinity of the location of minimum wall shear, $w = w_m$. From figure 4.3, it is seen that $w_m \approx 5$ for values of $\mu \geq 0.8$. The corresponding distance from the mean flow stagnation point is $s_m \approx 15 r_n$, so that $\omega s_m / U_e \approx 15 S$. Thus, for low values of S, the minimum wall shear point lies within the leading-edge receptivity region, and the receptivity which occurs in the vicinity of w_m can be calculated by the present method, while at higher values of S the minimum wall shear point lies downstream of the leading-edge receptivity region.

The marginal separation receptivity analysis of Goldstein *et al* (1987) assumes $\mu_c - \mu = O(\epsilon^{\frac{14}{5}})$ and $S = O(\epsilon^{-1})$. The scaling with respect to μ leads to an interactive viscous-inviscid structure for the mean flow in the vicinity of w_m, but with a local streamwise scale of $O(\epsilon^2)$ as compared to the $O(\epsilon^3)$ scale of standard triple-deck theory. The fact that the length scale of the low wall shear region is larger than that for standard triple-deck theory leads to additional complexity relative to the localized receptivity analysis of Goldstein (1985), in which the variations in surface geometry and the Tollmien–Schlichting wavelength both have the triple-deck scale. Specifically, in Goldstein's marginal separation analysis, the instability waves in the marginal separation region are interactive but their wavelength is shorter than the local scale for the mean flow. This leads to an exponentially small initial amplitude for the instability wave, but the wave undergoes exponential amplification in the marginal separation region and somewhat downstream, so that the marginal separation receptivity mechanism may well be important in applications.

Our analysis assumes a high Reynolds number $\epsilon \ll 1$ with $\mu_c - \mu = O(1)$, so that the mean flow remains non-interactive in the low wall shear region. Thus, we cannot make direct comparisons with the analysis of Goldstein *et al* (1987). However, as discussed above, at sufficiently low Strouhal numbers the region of low wall shear is contained within the leading-edge receptivity region, which is treated by our theory. It is then natural to investigate the relative importance of the receptivity in the region of low wall shear relative to the receptivity near the mean flow stagnation point.

We investigate the relative importance of receptivity near the mean flow stagnation point and receptivity in the region of low wall shear by artificially switching off the unsteady slip velocity at various downstream positions, using a smooth transition function. Here we are focusing on the *relative* receptivity for different free-stream disturbance functions, and this can be calculated very accurately even when μ is large. Essentially, the development of the unsteady disturbance along a ray in the complex w plane contains two phases. First, over a relatively short distance the asymptotic eigenfunction ψ_1 grows exponentially relative to the other components of the solution and becomes the dominant component. Second, over a much larger distance the asymptotic eigenfunction evolves algebraically toward its large-w form (4.33). Both phases of the development of the unsteady field must be calculated accurately to determine values of the receptivity coefficient. In contrast, a calculation of only the first phase is adequate to determine relative receptivity levels, since the same asymptotic behavior of the eigenfunction arises in the second phase independent of the form of the free-stream disturbance.

Thus consider a modified slip velocity

$$\hat{u}_s(w) = u_s(w)\Phi(w, w_0) \tag{4.49}$$

where the smooth transition function $\Phi(w, w_0)$ is defined by

$$\Phi(w, w_0) = \frac{1 - \tanh(z)}{1 - \tanh(z_0)}, \qquad z = \frac{w - w_0}{\delta_w}, \qquad z_0 = -\frac{w_0}{\delta_w}. \tag{4.50}$$

The modified slip velocity is the same as the physical slip velocity at the steady stagnation point ($w = 0$), then decreases smoothly and monotonically to zero in the vicinity of $w = w_0$. The transition occurs over a w-scale of δ_w. The corresponding unsteady pressure gradient is then given by

$$\frac{\mathrm{d}\hat{p}}{\mathrm{d}w} = \Phi\frac{\mathrm{d}p}{\mathrm{d}w} - \Phi_w\frac{wu_s}{h} \tag{4.51}$$

and we extract the modified Receptivity Coefficients $\widehat{C}_s(\mu, S, w_0, \delta_w)$ and $\widehat{C}_a(\mu, S, w_0, \delta_w)$ from the solutions of

$$
\left.
\begin{aligned}
\mathcal{F}(\widehat{\psi}_s) &= S^{\frac{1}{2}} \left\{ \Phi \left(iSh^2(w-\mu) + \frac{\mu - 2w + \mu(w-\mu)^2}{h^2} \right) - \Phi_w w(w-\mu) \right\}, \\
\mathcal{F}(\widehat{\psi}_a) &= \Phi \left(iSh^2 - \frac{1+\mu^2-w^2}{h^2} \right) - \Phi_w w,
\end{aligned}
\right\}
\tag{4.52}
$$

respectively. By varying w_0, it is hoped that the relative contribution of different stream-wise regions to the total receptivity can be determined. However, the introduction of a new artificial stream-wise scale (i.e. δ_w) clearly provides another possible source of receptivity. Thus care must be taken in choosing δ_w, small enough that the different regions of receptivity can be differentiated, but not so small that the receptivity associated with the rapid change in unsteady slip velocity dominates other contributions to the receptivity. Moreover, Φ is singular when $w = w_0 - \frac{1}{2}\pi\delta_w i$. Hence our choice of δ_w is restricted by the condition $\delta_w > 2w_0 \tan(\arg w)/\pi$, which ensures that the integration contour does not pass through any such singularity.

To examine the contributions to the receptivity on the upper surface when the body is close to the critical angle-of-attack, in figure 4.6 we plot the magnitude of

$$
\Gamma(\mu, S, w_0, \delta_w) = \frac{\widehat{C}_s(\mu, S, w_0, \delta_w)}{C_s(\mu, S)}
\tag{4.53}
$$

for $\mu = 1.0$ and $\delta_w = 3.0$. The results are plotted as a function of the filter switch-off point w_0, for two Strouhal numbers $S = 0.1$ and 0.3. The value of $|\Gamma|$ is seen to approach one as w_0 increases, indicating that the receptivity process is complete. The receptivity region would be expected to be concentrated closer to the mean flow stagnation point at the higher frequency $S = 0.3$, and this behavior is indeed seen in the plot of $|\Gamma_s|$. Upon closer inspection, a similar trend can be seen in the plot for $|\Gamma_a|$. The minimum wall shear point $w = 4.54$ is marked with a vertical dashed line on the plots. For $S = 0.3$, the receptivity process appears to have been completed by the time the region of low wall shear is reached. In contrast, for $S = 0.1$, $|\Gamma_s|$ does not approach the value of one until w_0 is approximately 7. Thus, in this case the region of low wall shear appears to make some contribution to the total receptivity. This is not unexpected, since the region of receptivity $\omega s/U_e = O(1)$ extends farther downstream by a factor of three for the case $S = 0.1$ as compared to the case $S = 0.3$. However, although the receptivity extends out through the region of low wall shear for the case $S = 0.1$, there is no indication in figure 4.6(a) of a concentration of receptivity in the region of low wall shear. It is interesting to note that $|\Gamma_s|$ is not a monotonically increasing function of w_0. This feature indicates that, at least for $|\Gamma_s|$, large receptivity close to the leading edge is partially cancelled out by receptivity processes farther downstream. We should note that some caution is necessary in evaluating the results for $S = 0.1$, since in that case the wavelength of the unsteady motion is longer and the results could have been influenced more by the finite value of the filter width δ_w.

The results presented in figure 4.6 show that the receptivity region extends farther downstream at lower values of the Strouhal number. In order to examine the extent to which it is possible to scale this feature out of the results, in figure 4.7 we plot $|\Gamma_s|$ as a function of $S^{\frac{1}{2}}w_0$, for a constant filter width in terms of the receptivity variable,
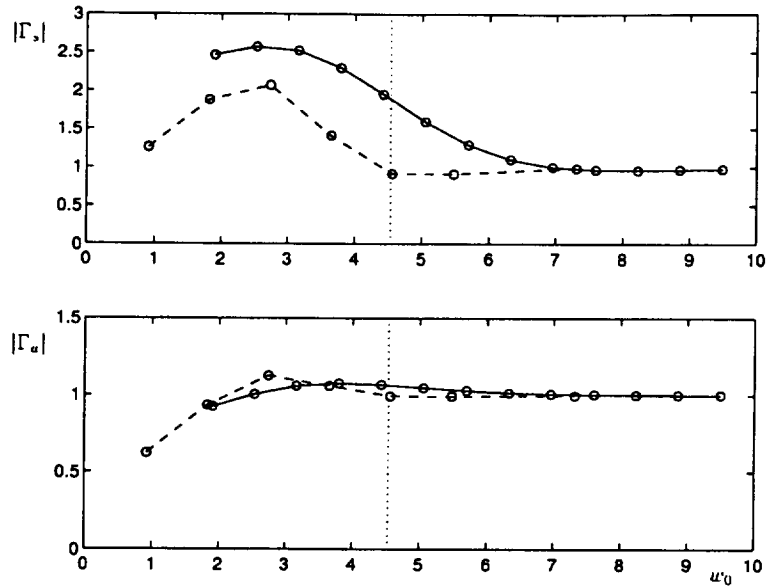
68

Figure 4.6: Plot of $|\Gamma|$ for $\mu = 1.0$, $\delta_w = 3.0$, and $S = 0.1$ (solid line) and $S = 0.3$ (dashed line), illustrating the relative receptivity as a function of the streamwise location of the filter, w_0, for (a) component of the disturbance symmetric about the nose; (b) component of the disturbance anti-symmetric about the nose. The dotted line marks the position of minimum wall shear, $w = 4.54$.

$\delta_\xi = S^{\frac{1}{2}}\delta_w = 0.96$. Results for presented for two values of the Strouhal number, $S = 0.1$ and 0.3. The case $\mu = 0$ is shown in figure 4.7(a). Here, plotting the results in terms of a variable scaled by the receptivity length scale has produced an excellent collapse of the results for the two values of S. In figure 4.7(b) for the case $\mu = 0.5$, the collapse is not as good, with the curve for $S = 0.3$ extending out to a somewhat larger value of $S^{\frac{1}{2}}w_0$ before approaching the value of one. This trend which appeared in figure 4.7(b) is magnified further in figure 4.7(c) where results for $\mu = 1.0$ are presented. However, in all cases the leading-edge receptivity process is completed by the time a downstream distance of $S^{\frac{1}{2}}w_0 = 3$ is reached. A number of factors may contribute to the lack of collapse in figures 4.7(b,c). First, the flow along the upper surface of the airfoil becomes successively more complex as the aerodynamic loading parameter is raised, so that there is not even an approximate similarity behavior for the mean boundary layer whose streamwise gradients are responsible for the receptivity process. Second, the strong acceleration of the flow between the stagnation point and the nose of the airfoil may introduce a significant shift in the 'virtual origin' of the boundary layer which could affect the streamwise development of the receptivity process. Thus, it seems unlikely that a collapse of the results for different frequencies could be achieved for cases with significant aerodynamic loading.

Similar calculations were performed for $\mu = -0.4$ and -0.8. The results for $|\Gamma|$ indicate that the receptivity on the lower surface is also concentrated in the region $S^{\frac{1}{2}}w_0 < 3$. The calculations did not produce any features which provide an explanation for the high receptivity levels in the vicinity of $\mu = -0.4$.

Despite the fact that not all aspects of the results are well understood, a number of general conclusions can be drawn. It is clear that modest levels of aerodynamic loading in

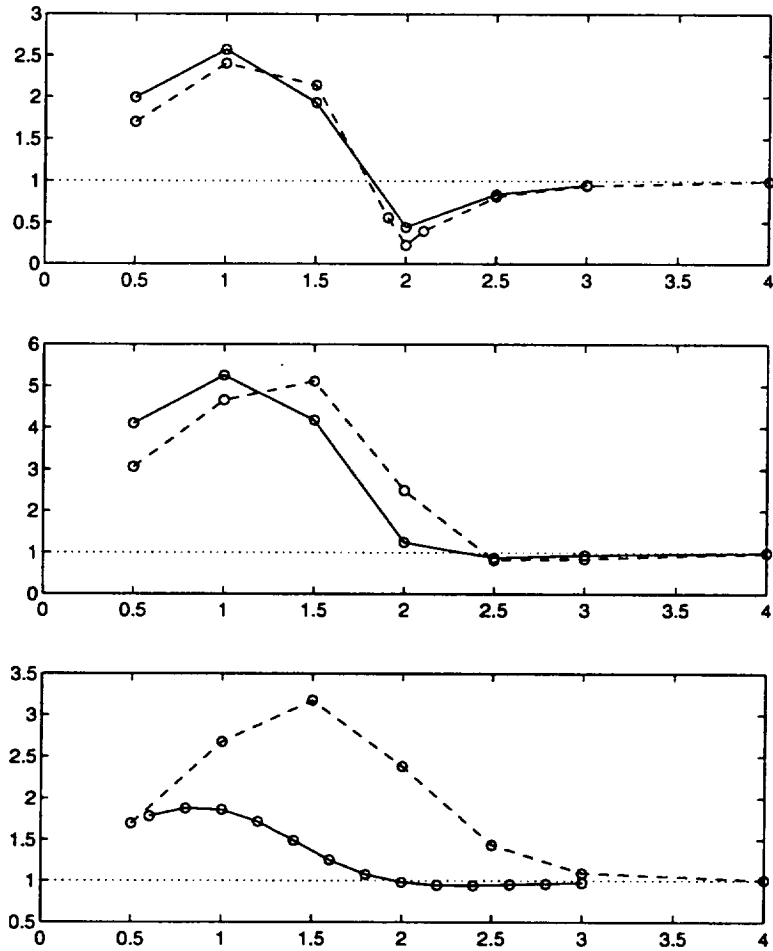69

Figure 4.7: Plot of $|\Gamma_s|$ against $S^{\frac{1}{2}}w_0$ for $S^{\frac{1}{2}}\delta_w = 0.96$ with: (a) $\mu = 0.0$, (b) $\mu = 0.5$, (c)$\mu = 1.0$. Results for $S = 0.1$ are shown with a solid line, those for $S = 0.3$ by a dashed line.

the leading-edge region cause a decrease in the receptivity level for the boundary layer on the upper surface of the airfoil, and an increase in receptivity for the lower surface. The effects are more pronounced at higher values of the Strouhal number, where the region of receptivity is concentrated nearer the stagnation point. Thus, it seems reasonable to suppose that the effects are related to the behavior of the mean flow pressure gradient near the stagnation point. For the upper surface, the introduction of aerodynamic loading leads to a movement of the stagnation point toward the lower surface, and an increased favorable pressure gradient in the region between the stagnation point ($w = 0$) and the leading edge ($w = \mu$). The decrease in receptivity level associated with these effects is consistent with the results obtained in chapter 2 for the case $\mu = 0$. The decrease in receptivity level on the upper surface in the presence of modest aerodynamic loading is of significance for applications such as laminar flow design. The subsequent rise in receptivity for values of μ nearer the critical value for separation also has important practical implications. For the lower surface, an argument that the increase in receptivity with modest aerodynamic loading is related to the pressure gradient near the stagnation point appears much more tenuous, since the changes in the pressure gradient near the stagnation point are not pronounced. However, from a practical standpoint, receptivity levels for the lower surface are usually of less interest, since the pressure gradient on the lower surface is typically favorable and the instability waves have much smaller growth rates.

It must also be kept in mind that, for leading-edge receptivity, quantities such as the instability wave amplitude at the neutral stability point depend crucially on a combination of receptivity and stability properties. There can be a subtle interplay between these, since a small change in growth/decay rate can counteract a significant change in receptivity level, for example. In fact, for the leading-edge receptivity mechanism, even the issue of the most appropriate definition of receptivity level is not straightforward. Experimental and computational researchers often favor a definition based on the lower branch amplitude. This is certainly of practical utility and has advantages with respect to measurements, but it does not distinguish between the receptivity and stability aspects of the disturbance development. The definition we have adopted has the advantage of separating the receptivity aspects from stability considerations, but of course the results must be combined with a stability calculation in order to predict amplitudes in the Orr-Sommerfeld region farther downstream.

Chapter 5

Conclusions

In this report, we have examined the influences of airfoil thickness and mean aerodynamic loading on leading-edge receptivity to acoustic free-stream disturbances. A high Reynolds number asymptotic analysis ($\epsilon = (\omega\nu/U^2)^{-\frac{1}{6}} \ll 1$) has been developed for the case of a two-dimensional airfoil with a parabolic leading edge. The airfoil is assumed thin ($\delta \ll 1$) and the mean flow Mach number $M = U/c$ is assumed small. The receptivity process takes place in the region of the boundary layer where the distance from the stagnation point is $O(U/\omega)$. Previous analyses of leading-edge receptivity considered the case of the Blasius boundary layer on a semi-infinite flat plate. In the present analysis, we assume that the radius of curvature r_n of the airfoil nose is $O(U/\omega)$. Thus, the leading-edge receptivity process takes place in the vicinity of the airfoil nose, and the receptivity coefficient depends on the thickness distribution of the airfoil only through the Strouhal number, $S = \omega r_n/U$, which has $O(1)$ values.

For a symmetric airfoil at zero angle of attack, the mean flow is symmetric about the leading edge and the receptivity characteristics on the two sides of the airfoil are the same. In contrast, for an airfoil with camber or non-zero angle of attack, there is generally a mean flow component around the leading edge and the boundary layers on the two surfaces of the airfoil have quite different characteristics. For $S = O(1)$, the leading-edge receptivity process depends on the mean aerodynamic loading only through a parameter related to the local flow in the vicinity of the airfoil nose. The aerodynamic loading parameter which enters the leading-edge receptivity analysis is

$$\mu = 2\alpha_e(\delta^2 b/r_n)^{\frac{1}{2}}, \tag{5.1}$$

where b is the airfoil semi-chord and α_e is an effective angle of attack parameter for the leading-edge region, discussed below. An aerodynamically loaded body typically has a mean flow component around the leading edge, from the lower surface to the upper, corresponding to positive values of α_e and μ. The parameter μ is a measure of the asymmetry of the mean flow in the leading-edge region. Separation of the boundary layer, on the upper surface just downstream of the leading edge, occurs when μ reaches the critical value $\mu_c \approx 1.15$. When discussing results below, positive values of μ are taken to correspond to receptivity on the upper surface for a typical aerodynamically loaded body, while negative values of μ correspond to receptivity on the lower surface for a typical aerodynamically loaded body.

The parameter μ is seen to depend on the airfoil thickness ratio δ, semi-chord b and nose radius r_n, in addition to the effective angle of attack parameter α_e. A brief discussion

72

of these dependencies seems worthwhile. The strength of the mean flow component around the leading edge depends on both the geometric angle of attack and the camber distribution of the airfoil; these dependencies are contained in the parameter α_e, defined by (4.8). For a thin airfoil, the camber and angle of attack must be small in order to avoid flow separation; hence, in defining α_e the small parameter δ has been extracted from the physical angle of attack and from the camber function, so that $\alpha_e = O(1)$. For a thin airfoil with a parabolic nose, the nose radius of curvature r_n is $O(\delta^2 b)$, so that the quantity under the radical is also $O(1)$. Physically, when the airfoil thickness is decreased the nose radius also decreases, leading to higher flow velocities around the sharper edge, so that the camber and/or angle of attack must be decreased correspondingly in order to avoid flow separation.

The asymptotic structure for high Reynolds number ($\epsilon \ll 1$) involves two stream-wise regions. In the first region, corresponding to downstream distances of $O(U/\omega)$, the unsteady component of the motion in the boundary layer is governed by the linearized unsteady boundary layer equation (LUBLE). Here the inviscid pressure field and slip velocity induced by the free-stream disturbances drives the unsteady motion in the boundary layer. The leading-edge receptivity process takes place in the LUBLE region. The second region is farther downstream, at distances of $O(\epsilon^{-2}U/\omega)$. In this region the unsteady disturbance is governed by the triple-deck structure, corresponding to the high Reynolds number asymptotic form of the Orr–Sommerfeld equation (OSE) in the vicinity of the lower branch. The free-stream disturbance that is present in the OSE region generates only a Stokes wave in the boundary layer, which is unrelated to the TS wave eigensolution. Thus, the amplitude of the TS wave cannot be determined by analysis of the OSE region alone. Rather, the amplitude of the instability wave is determined by the asymptotic matching of the LUBLE and OSE regions.

The asymptotic matching of the LUBLE and OSE regions is carried out in the over-lap region, $1 \ll \omega x^*/U \ll \epsilon^{-2}$, where x^* is the dimensional distance from the stagnation point. (The analysis was carried out in a parabolic coordinate system, but the physical variable x^* is utilized in this discussion for convenience.) Thus, the overlap region corresponds to distances 'far downstream' in the LUBLE region, but 'far upstream' in the OSE region. Far downstream in the LUBLE region, the unsteady flow consists of a generalized Stokes wave driven by the local unsteady pressure gradient in the free stream, plus an infinite set of asymptotic eigensolutions, ψ_i. These asymptotic eigensolutions were first found by Lam & Rott (1960) for the case of the Blasius boundary layer. The asymptotic eigensolutions of the LUBLE obtained in the present work are generalizations of the Lam–Rott expression, taking account of the influences of airfoil thickness and aerodynamic loading. The Lam–Rott eigensolutions are 'asymptotic' in the sense that they exist only for $\omega x^*/U \gg 1$, where the mean flow varies slowly in the streamwise direction relative to the scale U/ω. The Lam–Rott eigensolutions contain velocity but not pressure fluctuations, and are uniformly valid solutions of the LUBLE for $\omega x^*/U \gg 1$. (However, they are *not* uniformly valid solutions to the full Navier–Stokes equations, as discussed below.) The asymptotic analysis for $\omega x^*/U \gg 1$ determines the form of the Lam–Rott eigensolutions, but not their coefficients C_i. These coefficients can be obtained only through a full solution of the LUBLE, which must be determined by numerical methods.

The wavelengths of the Lam–Rott eigensolutions shorten progressively with distance downstream. When the OSE region is reached ($\omega x^*/U = O(\epsilon^{-2})$), the self-induced

73

pressure field associated with the displacement thickness of each asymptotic eigensolution becomes significant, and the triple-deck structure replaces the LUBLE as the correct asymptotic approximation to the Navier–Stokes equation. The asymptotic matching of the LUBLE and OSE regions in the overlap domain $1 \ll \omega x^*/U \ll \epsilon^{-2}$ shows that the first Lam–Rott eigensolution ψ_1 of the LUBLE matches onto the TS wave eigensolution of the OSE. Thus, the form of the free-stream disturbance and the geometry close to the nose influence the amplitude of the TS wave only through the coefficient C_1 of the first asymptotic eigensolution. Therefore, we call C_1 the 'receptivity coefficient'. The primary objective of this work is to determine the receptivity coefficient as a function of the leading-edge nose radius parameter S, aerodynamic loading parameter μ, and free-stream disturbance characteristics.

In order to determine the receptivity coefficient, a numerical solution of the LUBLE is obtained for specified values of the nose radius parameter S and the aerodynamic loading parameter μ. The free-stream disturbance must also be specified; it can be represented as a superposition of components symmetric and anti-symmetric about the nose, as discussed below. The value of the receptivity coefficient C_1 is then found by comparing the numerical solution for large downstream distances $(\omega x^*/U \gg 1)$ with the analytical expression for the first asymptotic eigensolution, ψ_1. However, this procedure cannot be carried out for real values of x^*, because the first asymptotic eigensolution becomes exponentially small far downstream. Moreover, the asymptotic eigensolutions are inversely ordered, so that the higher-order eigensolutions ψ_i, $i = 2, 3, \ldots$ are exponentially large compared to ψ_1. Thus, it is extremely difficult to extract the coefficient C_1 from the numerical solution for real x^*. This difficulty is circumvented by taking advantage of the fact that the LUBLE is analytic in x^*, and extending the computation into a region of the complex x^*-plane where the asymptotic eigensolutions grow exponentially with downstream distance. The inverse ordering of the eigensolutions is also rectified by this process, so that ψ_1 is exponentially dominant far downstream, allowing its coefficient to be extracted from the numerical results. A number of analytical features are exploited in implementing the numerical computations, in order to increase the precision of the results for C_1. However, calculations for conditions very near boundary layer separation are difficult, so that despite these efforts there is still uncertainty in the numerical value of C_1 for values of μ near $\mu_c \approx 1.15$.

For sufficiently small amplitudes of the unsteady motion, the receptivity and the initial growth of the instability wave are linear processes. Our theory addresses this linear regime. Thus, it is natural to define the receptivity level as a ratio of the amplitude of the instability wave in the boundary layer, or its upstream precursor, to the unsteady motion in the free stream. For localized receptivity which occurs in the OSE region, an instability wave is generated directly at the receptivity site (e.g. a short-scale wall hump), so that the receptivity level can be expressed in terms of the instability wave amplitude at that point. In contrast, for leading-edge receptivity, the receptivity process occurs upstream in the LUBLE region. In this case the 'best' definition of receptivity level is not so obvious. Various measures of receptivity can be considered. We have chosen to define C_1, the coefficient of the first Lam–Rott asymptotic eigensolution, as the 'receptivity coefficient'.

Alternative definitions of receptivity level that have been considered in computations and experiments are values based on the TS wave amplitude at the lower neutral-stability point (branch I), or an extrapolation of the TS wave amplitude back to the leading edge.

A receptivity level defined in terms of the TS wave amplitude at the lower branch neutral-stability point does allow easy comparison with experiments or computations, but has the disadvantage that the results depend on both frequency and Reynolds number, making presentation of the results much less compact. Extrapolation of the TS wave amplitude back to the leading edge is not advisable, since the TS wave is not a valid solution of the disturbance equations near the leading edge. In fact, in extrapolating back to the leading edge, the slowly varying amplitude $A(x^*)$ multiplying the mode-shape function of the TS wave should be considered, and $A(x^*)$ is singular as $x^* \to 0$, becoming infinite at the leading edge.

From a theoretical standpoint, the coefficient C_1 of the first Lam–Rott asymptotic eigensolution of the LUBLE is the most attractive measure of receptivity. This Lam–Rott eigensolution evolves into the unstable TS wave farther downstream so that, when appropriate scaling factors related to the asymptotic matching of the LUBLE and OSE regions are introduced, C_1 is also the coefficient of the TS wave. An extremely attractive feature of this receptivity measure is that C_1 is independent of the frequency and the (asymptotically large) Reynolds number, thus providing the receptivity results in the simplest dimensionless form. The quantity C_1 is determined by the unsteady flow behavior upstream of the region of instability and therefore focuses on the receptivity aspect of the unsteady flow development, with much less influence from the global stability properties of the flow. Also, for fixed values of the frequency and Reynolds number, variations in the receptivity coefficient C_1 with changes in the free-stream disturbance characteristics translate directly into variations in the TS wave amplitude.

The instability wave amplitude which is found for a given free-stream disturbance in a specific situation depends on a number of processes. First, the free-stream disturbance interacts with the body (and other surrounding surfaces, if present) to produce an inviscid unsteady pressure gradient and slip velocity which drives the unsteady motion in the boundary layer. Next, through the receptivity process, some of the energy contained in the unsteady motion just outside the boundary layer is transferred to the first Lam–Rott asymptotic eigensolution, which eventually evolves into the TS wave of the OSE region. Obviously, both the inviscid processing and the subsequent receptivity process influence the amplitude of the TS wave.

The present work has addressed receptivity to free-stream acoustic waves. The disturbance velocity of the acoustic wave far from the airfoil has been utilized in normalizing the receptivity coefficient C_1. The acoustic wave is assumed to propagate in a direction perpendicular to the airfoil span, so that the unsteady interaction is two-dimensional. The angle between the direction of propagation and the airfoil chordline is denoted by θ. The Mach number has been assumed small, so that the acoustic wavelength is long compared to the hydrodynamic length scale U/ω for the unsteady motion. Thus, in analyzing the LUBLE region, the flow can be considered incompressible.

Since S has been assumed $O(1)$, only the characteristics of the free-stream disturbance on the scale of the nose radius, r_n, are required. The incompressible irrotational flow in the vicinity of the airfoil nose can be represented by a superposition of two components: (a) a symmetric flow past the parabolic nose, and (b) an anti-symmetric flow around the parabolic nose. The disturbance slip velocity which drives the unsteady motion in the boundary layer can similarly be separated into symmetric and anti-symmetric components, with coefficients $\kappa_s(\theta)$ and $\kappa_a(\theta)$, respectively (2.50). Since the equations governing the unsteady motion in the LUBLE region are linear, the response to the

symmetric and anti-symmetric components of the disturbance slip velocity near the airfoil nose can be superposed, so that the receptivity coefficient can be expressed in the form (2.52)

$$C_1 = \kappa_s(\theta)C_s(S,\mu) + \kappa_a(\theta)C_a(S,\mu). \tag{5.2}$$

This expression effectively separates the effects of the inviscid processing (contained in κ_s and κ_a) from the intrinsic receptivity of the boundary layer. The quantities C_s and C_a are the receptivity coefficients to the symmetric and anti-symmetric components of the disturbance slip velocity, respectively. The receptivity coefficients C_s and C_a are universal functions which do not depend on the propagation angle of the acoustic wave or the mean flow Mach number. Results for C_s and C_a are discussed below.

In a given physical situation, the behavior observed for the receptivity as a function of various parameters may be influenced strongly by the inviscid processing of the disturbance as represented by the coefficients κ_s and κ_a. In addition to the incidence angle of the acoustic wave, κ_s and κ_a depend on the acoustic reduced frequency $k = \omega b/c$. Relatively simple expressions for κ_s and κ_a can be obtained for the two limiting cases of $k \ll 1$ and $k \gg 1$, as discussed in section 2.4. The acoustic reduced frequency can be expressed as the product $k = aM$, where $a = \omega b/U$ is the aerodynamic reduced frequency. For extremely low Mach numbers, the acoustic wavelength is long not only compared to the hydrodynamic length scale U/ω, but also compared to the airfoil chord. Then $k \ll 1$ and we obtain (2.58),

$$\kappa_s = \cos\theta, \qquad \kappa_a = a^{\frac{1}{2}}\sin\theta. \tag{5.3}$$

Note that $a = Sb/r_n$, which is a large quantity for a thin airfoil with $S = O(1)$. The second limit is that of M small but a very large. Then $k \gg 1$ and the acoustic wavelength is short compared to the airfoil chord (but still long compared to the airfoil nose radius). For $k \gg 1$, we obtain (2.62)

$$\kappa_s = \cos\theta, \qquad \kappa_a = \frac{2e^{-\frac{1}{4}i\pi}}{(\pi M)^{\frac{1}{2}}}\sin\frac{1}{2}\theta. \tag{5.4}$$

In both limits, the coefficient for the anti-symmetric component of the disturbance is large compared to the coefficient for the symmetric component. Basically, the unsteady disturbance level near the airfoil nose is much larger for an oblique acoustic wave than for a wave propagating parallel to the airfoil chord ($\theta = 0$), due to the induced flow around the relatively sharp leading edge of the thin airfoil. For $k \ll 1$, the size of κ_a is determined by finite chord effects, while for $k \gg 1$ the size of κ_a is determined by compressibility effects. It should be noted that the dependence of κ_a on θ is quite different for the two limits $k \ll 1$ and $k \gg 1$. These results are for the case of an obliquely propagating acoustic wave in free space. When the acoustic field is contained in an enclosed region, such as within a wind tunnel, more complicated behavior is found (see Heinrich & Kerschen 1989).

In chapter 2, results for $C_s(S)$ and $C_a(S)$ are presented for the case of a symmetric mean flow past a parabolic leading edge ($\mu = 0$). The magnitude of C_s is plotted as a function of S in figure 2.4. The magnitude of C_s at first rises slightly for very small S ($0 < S < 0.02$), then decays monotonically with further increases in S. For $S = 0.3$, the value of $|C_s|$ is only about 15% of its value for $S = 0$. The decay of $|C_s|$ appears to be exponential in S, although this has not been verified analytically. The phase,

arg(C_s), also plotted in figure 2.4, increases monotonically with S. The increase in arg(C_s) corresponds to a lag in phase of the TS wave.

The magnitude and argument of the ratio of receptivity coefficients, $\Lambda = C_a/C_s$, is plotted in figure 2.5. The magnitude $|\Lambda|$ is approximately 6 in the flat-plate limit $S \to 0$, where the anti-symmetric component of the slip velocity has a square-root singularity at the leading edge. The value of $|\Lambda|$ decreases rapidly as a finite nose radius is introduced, relieving the singularity at the leading edge. Thus, the behavior of C_a for very small S is quite different from that for C_s, where a small rise in magnitude was seen. The behavior of C_a for $S \ll 1$ is in fact singular, as discussed below. Beyond $S = 0.05$ the decline in $|\Lambda|$ becomes more gradual, the value of $|\Lambda|$ remaining above 2.5 right out to $S = 0.3$. For all values of S examined, the anti-symmetric component of the slip velocity was found to be more effective than the symmetric component in generating a TS wave.

The important role of the inviscid processing of the free-stream disturbance is illustrated in figures 2.6 and 2.7. In figure 2.6, the receptivity coefficient C_1 is plotted as a function of the incidence angle θ of the acoustic wave, for the case $k \ll 1$ and $a = 10$. The overall pattern is similar to the function $|\sin\theta|$, indicating that the dominant contribution comes from the receptivity to the anti-symmetric part of the disturbance. This behavior is explained by noting that the ratios $|\kappa_a/\kappa_s|$ and $|\Lambda| = |C_a/C_s|$ are both significantly greater than one. In figure 2.7, the corresponding results are plotted for the case $k \gg 1$ and $M = 0.1$. The overall pattern in this case is similar to the function $|\sin\frac{1}{2}\theta|$, indicating that the dominant contribution again comes from the receptivity to the anti-symmetric part of the disturbance, since $|\kappa_a/\kappa_s|$ is significantly greater than one in this limit as well.

The results presented in figure 2.5 suggest that C_a is singular in the limit $S \to 0$. In chapter 3, a small-S asymptotic theory is developed for the case of a symmetric mean flow past a parabolic leading edge ($\mu = 0$). For small values of S, the nose radius r_n of the airfoil is small compared to the streamwise length scale U/ω for the LUBLE region where the receptivity occurs. Thus, in this case three streamwise regions must be considered: the nose region (which scales on r_n), the LUBLE region (which scales on U/ω) and the OSE region (which scales on $\epsilon^{-2}U/\omega$). The solution in the nose region is a quasi-steady perturbation at leading order. In contrast, the solution in the LUBLE region is fully unsteady, and viscous-inviscid interactions appear in the OSE region. The matching of the LUBLE and OSE regions follows that discussed above. From the forms of the expansions in the nose and LUBLE regions, the receptivity coefficient to the symmetric component of the free-stream disturbance, $C_s(S)$, has an expansion in terms of S^0, $S\log S$, S, $S^{1.887}$, ...; the corresponding expansion for $C_a(S)$ contains S^0, $S^{\frac{1}{2}}$, $S\log S$, S, $S^{1.387}$, ... However, asymptotic matching of the (numerical) solutions for the nose and LUBLE regions leads to the surprising result that the coefficients of the $S\log S$ terms in C_s and C_a are approximately zero (i.e. to within the accuracy of the computations). The following asymptotic expansions are obtained:

$$C_s(S) \sim (-0.441 + 0.841\,\mathrm{i}) + (0.62 + 3.67\,\mathrm{i})S + O(S^{1.887}),$$

$$C_a(S) \sim (-5.33 + 1.66\,\mathrm{i}) + (12.08 + 6.34\,\mathrm{i})S^{\frac{1}{2}} + (-10.7 + 24.2\,\mathrm{i})S + O(S^{1.387}).$$

These small-S asymptotic results are compared to numerical results in chapter 3. The small-S expansions are found to have only a small range of validity near $S = 0$. However, the singular structure of $C_a(S)$ has been elucidated, and the asymptotic formula provides

accurate quantitative results in the region near $S = 0$ where the receptivity coefficient varies most rapidly with respect to this parameter.

The influence of aerodynamic loading on the leading-edge receptivity process was investigated in chapter 4. The analysis of the Lam–Rott asymptotic eigensolution is much more complicated in this case, due to the presence of two parameters (S and μ) and the need to retain many more terms in the asymptotic expansions. The numerical computations are also more demanding. For $\mu = 0$, a single computation is adequate to fully describe the mean flow in the vicinity of the parabolic leading edge. In contrast, in the presence of aerodynamic loading, a separate computation for the mean flow is required for each value of μ. For conditions in the vicinity of boundary layer separation ($\mu_c \approx 1.15$), the mean flow calculation becomes much more difficult since the behavior of the boundary layer becomes very sensitive to small changes in parameter values, and a large downstream distance is required for the boundary layer to recover from the region of low wall shear. The numerical extraction of the receptivity coefficient becomes correspondingly more difficult. Thus, for conditions near boundary layer separation, values of the receptivity coefficient cannot be obtained to the same accuracy as elsewhere.

In figure 4.5, results for $|C_s|$ and $|C_a|$ are presented as a function of the aerodynamic loading parameter μ, for two values of the Strouhal number, $S = 0.1$ and 0.3. The overall patterns of the variation with μ are qualitatively similar for $|C_s|$ and $|C_a|$. However, the receptivity levels for anti-symmetric forcing are somewhat larger than those for symmetric forcing, as found previously in the absence of aerodynamic loading (see figure 2.5). As the aerodynamic loading parameter is increased from zero, the receptivity level on the upper surface ($\mu > 0$) decreases until $\mu \approx 0.7$. The receptivity level then increases to a local maximum in the vicinity of $\mu \approx 0.9$, with a subsequent decrease in receptivity level as μ is increased further. On the lower surface ($\mu < 0$), the receptivity level increases as aerodynamic loading is introduced, to a global maximum in the vicinity of $\mu \approx -0.4$. The receptivity level then decreases as μ approaches -1. The variations in both $|C_s|$ and $|C_a|$ as a function of μ are much larger for $S = 0.3$ than for $S = 0.1$.

As discussed earlier, receptivity can occur in the leading-edge region, or in a localized region farther downstream in the boundary layer where some external feature forces the boundary layer to adjust on a short streamwise length scale. For conditions near boundary layer separation where $\mu_c - \mu = O(\epsilon^{\frac{14}{5}})$, the mean boundary layer develops a short local streamwise length scale of $O(\epsilon^2)$. Goldstein, Leib & Cowley (1987) developed a local receptivity analysis for this 'marginal separation' case, also assuming that $S = O(\epsilon^{-1})$. The streamwise length scale of $O(\epsilon^2)$ for marginal separation is longer than the standard triple-deck length scale of $O(\epsilon^3)$ associated with localized receptivity, leading to additional complexity in the analysis. We cannot make direct comparisons with the results of Goldstein et al., since our analysis assumes $\mu_c - \mu = O(1)$ and $S = O(1)$. However, at sufficiently low Strouhal numbers, the region of low wall shear is contained within the leading-edge receptivity region and hence is treated by our theory. We investigated the relative importance of receptivity in the region of low wall shear for these cases by artificially switching off the unsteady slip velocity at various downstream positions, using a smooth transition function. For small values of S and larger values of μ, within the parameter range examined, the region of low wall shear appears to make some contribution to the receptivity, but it is not dominant over the receptivity from the region nearer the leading edge. It should be noted that this observation does not contradict the conclusions of Goldstein et al., since they addressed a different region of parameter space.

In summary, the leading-edge receptivity theory has been extended to address the influences of leading-edge thickness and mean aerodynamic loading. Receptivity coefficients have been calculated for the case of acoustic free-stream disturbances in a low Mach number flow. A number of general conclusions can be drawn. The introduction of leading-edge thickness causes a decrease in receptivity levels relative to the case of a flat plate. It is also clear that modest levels of aerodynamic loading decrease the receptivity on the upper surface, but increase the receptivity on the lower surface. The effects are more pronounced at higher values of the Strouhal number, where the region of receptivity is concentrated nearer the stagnation point. A rise in receptivity level on the upper surface occurs for larger values of aerodynamic loading. The decrease in receptivity level on the upper surface in the presence of modest aerodynamic loading is of significance for applications such as laminar flow design. The subsequent rise in receptivity for values of μ nearer the critical value for separation also has important practical implications.

It must be kept in mind that, for leading-edge receptivity, quantities such as the instability wave amplitude at the lower branch neutral-stability point depend crucially on a combination of receptivity and stability properties. There can be a subtle interplay between these, since a small change in growth/decay rate can counteract a significant change in receptivity level, for example. There is a need to relate receptivity levels defined in terms of C_1 to levels expressed in terms of branch I amplitudes. In the asymptotic theory, this is achieved by developing the asymptotic expression for the TS wave in the OSE region and matching this expression to the generalized Lam–Rott asymptotic eigensolution. An alternative approach is the numerical solution of the disturbances equations, using the Lam–Rott asymptotic eigensolution as a starting condition and continuing downstream of branch I.

Important questions for further study include the receptivity to vortical free-stream disturbances, and compressibility effects for high subsonic and supersonic Mach numbers. Corroboration of the present theory with experimental and computational results is also an important objective. In comparing results of the asymptotic theory with computations or experiments, it is essential to take proper account of differences in the definitions of receptivity levels.

Chapter 6

References

ABRAMOWITZ, M. & STEGUN, I. A. 1965 *Handbook of Mathematical Functions.* Dover.

ACKERBERG, R.C. & PHILLIPS, J.H. 1972 The unsteady laminar boundary layer on a semi-infinite flat plate due to small fluctuations in the magnitude of the free-stream velocity. *J. Fluid Mech.* **51**, 137–157.

BROWN, S.N. & STEWARTSON, K. 1973 On the propagation of disturbances in a laminar boundary layer. *Proc. Camb. Phil. Soc.* **73**, 493–514. CHENG, H. K. & ROTT, N. 1954 Generalizations of the inversion formula of thin airfoil theory. *J. Rat. Mech. Anal.* **3**, 357-382.

CHOUDHARI, M. & KERSCHEN, E.J. 1989 Receptivity to three-dimensional convected gusts. In *Proceedings of ICASE/NASA Langley Instability and Transition Workshop,*, Springer Verlag.

CHOUDHARI, M. 1990 Boundary layer receptivity mechanisms relevant to laminar flow control. Ph.D. thesis, University of Arizona.

CHOUDHARI, M. & KERSCHEN, E.J. 1990 Instability wave patterns generated by interaction of sound waves with three-dimensional wall suction or roughness *AIAA* 90–0119.

GARRICK, I.E. 1957 Nonsteady wing characteristics. In *Aerodynamic components of aircraft at high speeds* (eds. A.F. Donovan & H.R. Lawrence) pp. 658–794. Princeton University Press.

GASTER, M. 1965 On the generation of spatially growing waves in a boundary layer. *J. Fluid Mech.* **22**, 433–441.

GOLDSTEIN, M.E. 1983 The evolution of Tollmien-Schlichting waves near a leading edge. *J. Fluid Mech.* **127**, 59–81.

GOLDSTEIN, M.E. 1985 Scattering of acoustic waves into Tollmien-Schlichting waves by small streamwise variations in surface geometry. *J. Fluid Mech.* **154**, 509–529.

GOLDSTEIN, M.E. & HULTGREN, L.S. 1989 Boundary-layer receptivity to long-wave free-stream disturbances. *Ann. Rev. Fluid Mech.* **21**, 137–166. GOLDSTEIN, M.E., LEIB, S.J. & COWLEY, S.J. 1987 Generation of Tollmien–Schlichting waves on interactive marginally separated flows. *J. Fluid Mech.* **181**, 485–517.

GOLDSTEIN, M.E., SOCKOL, P.M. & SANZ, J. 1983 The evolution of Tollmien-Schlichting waves near a leading edge. Part 2. Numerical determination of amplitudes. *J. Fluid Mech.* **129**, 443–453.

HAMMERTON, P.W. & KERSCHEN, E.J. 1996 Boundary-layer receptivity for a parabolic leading edge. *J. Fluid Mech.* **310**, 243–267.

HAMMERTON, P.W. & KERSCHEN, E.J. 1997 Boundary-layer receptivity for a parabolic leading edge. Part 2. The small-Strouhal number limit. *J. Fluid Mech.* **353**, 205–220.

HAMMERTON, P.W. & KERSCHEN, E.J. 1998 Leading-edge receptivity for bodies with mean aerodynamic loading. Submitted to *J. Fluid Mech.*

HEINRICH, R.A., CHOUDHARI, M. & KERSCHEN, E.J. 1988 A comparison of boundary layer receptivity mechanisms. *AIAA* 88-3758.

HEINRICH, R.A.E. 1989 Flat-plate leading-edge receptivity to various free-stream disturbance structures. PhD thesis, University of Arizona.

HEINRICH, R.A.E. & KERSCHEN, E.J. 1989 Leading-edge boundary layer receptivity to various free-stream disturbance structures. *Z. angew. Math. Mech.* **69** 6, T596–598.

KACHANOV, YU.S., KOZLOV, V.V., & LEVCHENKO, V.YA. 1982 Initiation of Turbulence in Boundary Layers. Novosibirsk: Nauka Publ. Siberian Div.

KELLER, H.B. & CEBECI, T. 1970 Accurate numerical methods for boundary layer flows– I. Two-dimensional laminar flows. In *Proceedings of the Second International Conference on Numerical Methods in Fluid Mechanics* (ed. M. Holt) pp. 92–100. Springer.

KERSCHEN, E.J. 1989 Boundary layer receptivity. *AIAA* 89-1109.

KERSCHEN, E.J., CHOUDHARI, M., & HEINRICH, R.A. 1989 Generation of boundary layer instability waves by acoustic and vortical free-stream disturbances. In *IUTAM 3rd Symposium on Laminar-Turbulent Transition.* Springer Verlag

KERSCHEN, E.J. 1990 Boundary layer receptivity theory. *Appl. Mech. Rev.* **43**, 152–157.

LAM, S.H. & ROTT, N. 1960 Theory of linearized time-dependent boundary layers. *Cornell Univ. Grad. School of Aero. Engineering Rep.* AFOSR TN-60-1100.

LAM, S.H. & ROTT, N. 1993 Eigen-functions of linearized unsteady boundary layer equations. *J. Fluids Eng.* **115**, 597–602.

LIBBY, P.A. & FOX, H. 1963 Some perturbation solutions in laminar boundary layer theory. Part 1: The momentum equation. *J. Fluid Mech.* **17**, 433–449.

LIGHTHILL, M.J. 1954 The response of laminar skin friction and heat transfer to fluctuations in the free-stream velocity. *Proc. R. Soc. Lond.* A **224** 1–23.

LIN, N., REED, H.L. & SARIC, W.S. 1992 Effect of leading-edge geometry on boundary-layer receptivity to freestream sound. In *Instability, Transition & Turbulence* (eds: Hussaini, M.Y., Kumar, A., & Streett, C.L.). Springer.

MURDOCH, J.W. 1981 Tollmien-Schlichting waves generated by unsteady flow over parabolic cylinders. AIAA-81-0199.

MORKOVIN, M.V. 1969 Critical evaluation of transition from laminar to turbulent shear layers with emphasis on hypersonically traveling bodies. *Air Force Flight Dyn Lab., Wright-Patterson AFB, Ohio.* AFFDL-TR-68-149.

NISHIOKA, M. & MORKOVIN, M.V. 1986 Boundary layer receptivity to unsteady pressure gradients: Experiments and overview. *J. Fluid Mech.* **171**, 219–261.

NOBLE, B. 1958 *Methods based on the Wiener-Hopf Technique.* Pergamon.

REED, H. L. & LYTTLE, I. 1998 DNS of leading edge receptivity to sound. *AIAA* 98-2644.

ROGLER, H. L. & RESHOTKO, E. 1975 Disturbances in a Boundary Layer Introduced by a Low Intensity Array of Vortices. *SIAM J. Appl. Math.* **28**(2) 431–462.

RUBAN, A.I. 1982 Asymptotic theory of short separation regions on the leading edge of a slender airfoil. *Fluid Dyn.* **17**, 33–41 (Engl. Trans.).

SARIC, W.S., WEI, W. & RASMUSSEN, B. 1994 Effect of leading edge on sound receptivity. In *Laminar-Turbulent Transition* (ed. R. Kobayashi) pp. 413–420. Springer.

SARIC, W.S., WEI, W., RASMUSSEN, B.K. & KRUTCKOFF, T.K. 1995 Experiments on leading-edge receptivity to sound. *AIAA* 95-2253.

SARIC, W. S. & WHITE, E. B. 1998 The influence of high amplitude noise on boundary layer transition to turbulence. *AIAA* 98-2645.

SEDOV, L.I. 1965 *Two-dimensional problems in hydrodynamics and aerodynamics.* Interscience Publishers.

STEWARTSON, K., SMITH, F.T. & KAUPS, K. 1982 Marginal Separation.

TAM, C. K. W. 1981 The Excitation of Tollmien-Schlichting Waves in Low Subsonic Boundary Layers by Free-stream Sound Waves. *J. Fluid Mech.* **109**, 483–501. *Stud. Appl. Maths* **67**, 45–61.

VAN DYKE, M.D. 1964a Higher approximations in boundary layer theory. Part 3. Parabola in uniform stream. *J. Fluid Mech.* **19**, 145–159.

VAN DYKE, M.D. 1964b *Perturbation methods in Fluid Mechanics.* Academic.

Appendix A

Evaluation of integrals involving Airy functions

Here we obtain alternative expressions for the integrals J_i, defined by

$$J_i = \int_{z_0}^{\infty} [z - z_0]^i \text{Ai}^2(z)\, dz, \qquad (A.1)$$

where $\text{Ai}'(z_0) = 0$. Setting $w = \text{Ai}^2(z)$, this satisfies

$$w''' - 4zw' - 2w = 0 \qquad (A.2)$$

(Abramowitz & Stegun (1965); equation 10.4.57), and hence

$$\int^{z} w(z')\, dz' = -\tfrac{1}{2}(w'' - 4zw). \qquad (A.3)$$

Thus $J_0(z_0)$ follows, noting that $w''(z_0) = 2z_0\text{Ai}^2(z_0)$. The other integrals J_i are then obtained by successive integration by parts,

$$
\begin{aligned}
J_i &= \frac{i}{2} \int_{z_0}^{\infty} (z - z_0)^{i-1}(w'' - 4zw)\, dz \\
&= -2iJ_i - 2iz_0 J_{i-1} + \frac{i}{2} \int_{z_0}^{\infty} (z - z_0)^{i-1} w''\, dz. \qquad (A.4)
\end{aligned}
$$

Hence,

$$
\left.
\begin{aligned}
J_0 &= -z_0\text{Ai}^2(z_0), \\
J_1 &= -\tfrac{2}{3}z_0 J_0, \\
J_2 &= \tfrac{1}{5}(-4z_0 J_1 + \text{Ai}^2(z_0)), \\
J_i &= -\frac{2i}{1 + 2i} z_0 J_{i-1} + \frac{i(i-1)(i-2)}{2(1 + 2i)} J_{i-3}, \qquad i \geq 3.
\end{aligned}
\right\} \qquad (A.5)
$$

Appendix B

Matching of asymptotic eigenfunctions to Tollmien-Schlichting modes

As the wavelength of the asymptotic eigenfunctions of the Linearized Unsteady Boundary Layer Equations progressively shortens with distance downstream, an outer inviscid layer begins to interact with the wall viscous layer. This occurs when $\xi = O(\epsilon^{-1})$. Writing $\hat{\xi} = \epsilon\xi$, we anticipate the rapid variation of ψ' by writing

$$\psi' = G(\eta, \hat{\xi}) \exp(i \int k \, d\hat{\xi}/\epsilon^3) \tag{B.1}$$

where the scaling is dictated by the need to match back to (3.17) as $\hat{\xi} \to 0$. As in the LUBLE regime, the exponential streamwise variation $k(\hat{\xi})$ is determined as an eigenvalue from the matching between the different layers. In the Orr-Sommerfeld region, the main deck ($\eta = O(1)$) is matched to an outer irrotational layer ($\eta = O(\epsilon^{-1})$) and to the inner viscous layer ($\eta = O(\epsilon)$). When $\xi = O(\epsilon^{-1})$, the classic triple deck scalings arise and the effect of the outer layer enters the expression for k at leading order. In the present investigation, $k(\hat{\xi})$ was determined using direct matching of the stream function between the decks, rather than by trying to modify standard Orr-Sommerfeld results to include wall curvature and mean pressure gradients effects.

Details of the matching are not included here, but an implicit expression for $k(\hat{\xi}, \epsilon)$ is eventually obtained,

$$\widehat{Q}(z_0) = \gamma^{-3} \left(1 - \frac{2S}{\hat{\xi}^2}\epsilon^2\right) h(z_0, \epsilon, \hat{\xi}), \tag{B.2}$$

where

$$\widehat{Q}(z_0) \equiv \frac{e^{\frac{1}{2}i\pi} z_0^2 \mathrm{Ai}'(z_0)}{\int_\infty^{z_0} \mathrm{Ai}(\tilde{z}) d\tilde{z}}, \qquad z_0 = \left(\frac{-i\widehat{H}^6}{U_0'^2 \gamma^2 \hat{\xi}^2 k^2}\right)^{\frac{1}{3}}, \qquad \gamma = 1 + A\frac{\ln \xi^2/S}{\xi^2/S} + B\frac{1}{\xi^2/S}$$

and

$$h(z_0, \epsilon, \hat{\xi}) \equiv \tilde{\xi}^3 + e^{i\pi/4} \tilde{\xi}^2 z_0^{3/2} \left(2 - \frac{\widehat{J}_1 \tilde{\xi}^3}{i z_0^3}\right) \epsilon + \tilde{\xi} z_0^3 i \left(1 + \frac{2\widehat{J}_2 \tilde{\xi}^3}{i z_0^3} - \frac{\widehat{J}_3 \tilde{\xi}^6}{z_0^6}\right) \epsilon^2 + O(\epsilon^3 \ln \epsilon),$$

Here $\tilde{\xi} = \hat{\xi}/U_0'$ and $\hat{J_i}$ are numerical constants involving integrals of the mean flow through the boundary layer, given by Goldstein (1983: equations 4.44-4.45). Solving (B.2) for $z_0(\hat{\xi}, \epsilon)$ gives

$$z_0 = \bar{z}_0 \left(1 + \frac{\tilde{\xi}^3 \Gamma}{\bar{z}_0 \hat{Q}'(\bar{z}_0)} \right) \qquad (B.3)$$

where $\bar{z}_0 \sim z_{00} + \epsilon z_{01} + \epsilon^2 z_{02} + O(\epsilon^3 \ln \epsilon)$ is the flat-plate result, and

$$\Gamma = -3A \frac{\ln \xi^2/S}{\xi^2/S} - (3B + 2)\frac{1}{\xi^2/S} = O(\epsilon^2 \ln \epsilon). \qquad (B.4)$$

Here we have written γ and Γ in terms of ξ rather than $\hat{\xi}$ for conciseness. Thus we finally obtain

$$k = \bar{k} \left(1 - A \frac{\ln \xi^2/S}{\xi^2/S} + (\tfrac{3}{2} - B)\frac{1}{\xi^2/S} \right) \left(1 - \frac{3\tilde{\xi}^3 \Gamma}{2\bar{z}_0 \hat{Q}'(\bar{z}_0)} \right) \qquad (B.5)$$

where $\bar{k} = e^{3i\pi/4}\hat{\xi}^2 \bar{z}_0^{-3/2}/U_0'$ is the flat plate result.

The leading order term in the small-ϵ expansion of $\bar{z}_0$ is given implicitly by

$$\hat{Q}(z_{00}) = \tilde{\xi}^3, \qquad (B.6)$$

which has a set of roots $z_{00}^{(i)}(\hat{\xi})$. As $\hat{\xi} \to 0$, $z_{00}^{(i)} \to -\rho_i$, where ρ_i is defined in §3, namely the i-th root of $\mathrm{Ai}'(-\rho) = 0$. The set of roots $k^{(i)}(\hat{\xi})$ then follows from (B.5). As $\hat{\xi} \to 0$,

$$k^{(i)} \sim \epsilon^2 \frac{e^{\frac{1}{4}i\pi}\xi^2}{U_0'\rho_i^{3/2}} \left(1 - A \frac{\ln \xi^2/S}{\xi^2/S} + (\tfrac{3}{2} - B)\frac{1}{\xi^2/S} \right) \qquad (B.7)$$

and hence

$$\frac{i}{\epsilon^3} \int_0^{\hat{\xi}} k^{(i)} d\hat{\xi} \sim -\frac{e^{-\frac{1}{4}i\pi}\xi^3}{U_0'\rho_i^{\frac{3}{2}}} \left(\frac{1}{3} - A_1 S \frac{\ln(\xi^2/S)}{\xi^2} + (2A_1 + 3/2 - B_1)\frac{S}{\xi^2} \right), \qquad (B.8)$$

which matches to the exponential variation of the eigenfunctions of the LUBLE region (3.17). Numerical solution of $\hat{Q}(z_{00}) = \tilde{\xi}^3$ shows that as $\tilde{\xi}$ increases, the imaginary part of the leading order term in $k^{(i)}$ stays positive for $i = 2, 3, \ldots$, corresponding to damped modes, but that $\mathrm{Im}(k^{(1)}) < 0$ for $\tilde{\xi} > 3.03$, which corresponds to a growing wave. Thus we have demonstrated that the first LUBLE eigenfunction does indeed match on to the unstable Tollmien-Schlichting mode. Moreover, (B.5) can be used to calculate the change in the position of the neutral stability point compared to the flat plate case.

Appendix C

Definition of the operators $\mathcal{N}^{(i)}_{\beta,\gamma}(w)$ and $\mathcal{R}^{(i)}_{\beta,\gamma}(w)$

In §§3.3 and 3.4 a set of partial differential operators $\mathcal{N}^{(i)}_{\beta,\gamma}(w)$ are used. These are defined as

$$
\left.
\begin{aligned}
\mathcal{N}^{(0)}_{\beta,\gamma}(w) &= w_{\eta\eta} + F w_{\eta\eta} + [i\xi^2 + (\beta + \lambda\xi^3)F']w_\eta + (\gamma - \lambda\xi^3)F''w \\
&\quad + \xi(F'' w_\xi - F' w_{\eta\xi}), \\
\mathcal{N}^{(3)}_{\beta,\gamma}(w) &= \frac{1}{\xi^2}\overline{\mathcal{N}}^{(3)}_{\beta,\gamma}(w), \\
\mathcal{N}^{(4)}_{\beta,\gamma}(w) &= -\frac{\ln(\xi^2)}{\xi^2}\overline{\mathcal{N}}^{(3)}_{\beta,\gamma}(w) + \frac{1}{\xi^2}\overline{\mathcal{N}}^{(4)}_{\beta,\gamma}(w) + iw_\eta.
\end{aligned}
\right\}
\tag{C.1}
$$

where

$$
\left.
\begin{aligned}
\overline{\mathcal{N}}^{(3)}_{\beta,\gamma}(w) &= \overline{G}_1 w_{\eta\eta} - (\beta + \lambda\xi^3)\overline{G}'_1 w_\eta - (\gamma - \lambda\xi^3)\overline{G}''_1 w - \xi(\overline{G}''_1 w_\xi - \overline{G}'_1 w_{\eta\xi}), \\
\overline{\mathcal{N}}^{(4)}_{\beta,\gamma}(w) &= (2\overline{G}_1 - \overline{G}_2)w_{\eta\eta} + ((\beta + \lambda\xi^3)\overline{G}'_2 - 2(F' + \overline{G}'_1))w_\eta \\
&\quad + (\gamma - \lambda\xi^3)\overline{G}''_2 w + \xi(\overline{G}''_2 w_\xi - \overline{G}'_2 w_{\eta\xi})
\end{aligned}
\right\}
\tag{C.2}
$$

In addition, the set of differential operators $\mathcal{R}^{(i)}_{\beta,\gamma}(f)$ are used, defined by

$$
\left.
\begin{aligned}
\mathcal{R}^{(3)}_{\beta,\gamma}(f) &= \overline{G}_1 f_{\eta\eta} - \beta\overline{G}'_1 f_\eta - \gamma\overline{G}''_1 f \\
\mathcal{R}^{(4)}_{\beta,\gamma}(f) &= (2\overline{G}_1 - \overline{G}_2)f_{\eta\eta} + (\beta\overline{G}'_2 - 2(F' + \overline{G}'_1))f_\eta + \gamma\overline{G}''_2 f
\end{aligned}
\right\}
\tag{C.3}
$$

so that

$$
\overline{\mathcal{N}}^{(i)}_{\beta,\gamma}(e^{\lambda\xi^3/3}f(\eta)) = e^{\lambda\xi^3/3}\mathcal{R}^{(i)}_{\beta,\gamma}(f(\eta))
\tag{C.4}
$$

for $i = 3, 4$.

Appendix D

Asymptotic form of base flow far downstream

In order to determine the form of the unsteady perturbation to the steady boundary-layer flow, the steady flow must be calculated accurately. In particular, to obtain the large-ξ asymptotic eigensolutions of the LUBLE, the base flow far downstream must be calculated correct to $O(w^{-3})$. Far downstream, the asymptotic expansion of the base flow is given by

$$\phi \sim F + \frac{\mu p_1}{w} + \frac{p_2 \log w^2}{w^2} + \frac{p_3}{w^2} + \frac{\mu p_4 \log w^2}{w^3} + \frac{\mu p_5}{w^3} + O\left(\frac{1}{w^{\gamma_2}}\right), \qquad (D.1)$$

where the fractional power $\gamma_2 \approx 3.774$ arises from the second eigensolution of Libby & Fox (1963). Here $F(\eta)$ is the Blasius solution and the $p_i(\eta)$ are determined by

$$\mathcal{L}_i(p_i) = d_i, \qquad (D.2)$$

where

$$\left.\begin{aligned}
\mathcal{L}_1(p) &\equiv p''' + Fp'' + F'p', \\
\mathcal{L}_2(p) \equiv \mathcal{L}_3(p) &\equiv p''' + Fp'' + 2F'p' - F''p, \\
\mathcal{L}_4(p) \equiv \mathcal{L}_5(p) &\equiv p''' + Fp'' + 3F'p' - 2F''p,
\end{aligned}\right\} \qquad (D.3)$$

and

$$\left.\begin{aligned}
d_1 &= 1 - F'^2, \\
d_2 &= 0, \\
d_3 &= [F'^2 - 1 - 2(p_2 F'' - p_2' F')] - \mu^2[F'^2 - 1 + 2F'p_1' + p_1'^2], \\
d_4 &= p_1'' p_2 - 3p_1' p_2' - 2F'p_2', \\
d_5 &= p_1'' p_3 - 3p_1' p_3' - 2F'p_3' + 2(F'p_4' - F''p_4) + 2(p_1'p_2' - p_1''p_2) + 2F'p_1' - \\
& \qquad 3(1 - F'^2) - \mu^2(F'^2 - 1 + 2F'p_1' + p_1'^2).
\end{aligned}\right\} \qquad (D.4)$$

These equations must be solved subject to the boundary conditions $p_i(0) = p_i'(0) = 0$, and the matching condition $p_i' \to 0$ exponentially as $\eta \to \infty$. The latter condition is necessary to ensure that vorticity decays exponentially at the outer edge of the boundary layer.

The function $p_1(\eta)$ is the response of the mean boundary-layer profile to the $O(w^{-1})$ term of the mean pressure gradient (4.28). An exact solution for $p_1(\eta)$ can be obtained in terms of the Blasius function $F(\eta)$; since the expression is cumbersome and only the wall

shear stress $p_1''(0)$ appears in our final results, $p_1(\eta)$ is not presented here. The second term in the mean pressure gradient is proportional to w^{-2}. However, if the series (D.1) for ϕ were assumed to proceed only in inverse powers of w, the solution that would be obtained for the $O(w^{-2})$ term would not exhibit exponential decay of vorticity at the outer edge of the boundary layer. Exponential decay of the vorticity is restored by including a term of $O(w^{-2} \log w^2)$ in (D.1), as discussed by Van Dyke (1964) for the symmetric flow case ($\mu = 0$). The equations governing $p_2(\eta)$ are homogeneous but admit an eigensolution, $p_2 = A_1(\eta F' - F)$. The coefficient A_1 is then determined by a secularity condition on the differential equation $\mathcal{L}_3(p_3) = d_3$ governing the $O(w^{-2})$ term. Multiplying both sides of this equation by F and integrating, after some manipulation we obtain

$$(1 - \mu^2)\left\{\log\left(\frac{\gamma}{F_0''}\right) - \frac{1}{4}\right\} + A_1 - \mu^2 \int_0^\infty F(2F'p_1' + p_1'^2)d\eta = 0, \qquad (D.5)$$

where $F_0'' \equiv F''(0) = 0.4696$ and $\gamma = 0.33054$, a constant appearing in the large-η asymptotic form of $F(\eta)$. Thus, setting $A_1 = \overline{A}_1 + \mu^2 \tilde{A}_1$, the numerical values of these constants are found to be

$$\overline{A}_1 = 0.60115, \qquad \tilde{A}_1 = -2.1656. \qquad (D.6)$$

Next consider the solution for $p_3(\eta)$. The operator $\mathcal{L}_3$ is identical to $\mathcal{L}_2$, so that $p_3(\eta)$ also contains an eigensolution $B_1(\eta F' - F)$. However, in this case the function $w^{-2}(\eta F' - F)$ is an eigensolution of the partial-differential perturbation equation (in fact, it is the first eigensolution of Libby & Fox (1963)). Therefore, the coefficient $B_1(\mu)$ remains undetermined in the large-w analysis. In §5, $B_1(\mu)$ is determined by comparing the large-w asymptotic expression for the wall shear with results obtained by numerical integration of the mean flow equations starting from the stagnation point $w = 0$.

The ordinary differential equation governing p_3 is inhomogeneous, so that a particular solution is also required. The need for numerical solution for each value of μ can be avoided by noting the form of the dependence on μ of the inhomogeneous term d_3. Similar remarks apply for p_4 and p_5. Thus we set

$$\left.\begin{array}{rcl} p_3 &=& B_1(\eta F' - F) + \bar{p}_3 + \mu^2 \tilde{p}_3, \\ p_4 &=& A_1 \bar{p}_4, \\ p_5 &=& B_1 \bar{p}_4 + \bar{p}_5 + \mu^2 \tilde{p}_5, \end{array}\right\} \qquad (D.7)$$

where the functions $\bar{p}_3$, $\tilde{p}_3$, $\bar{p}_4$, $\bar{p}_5$ and $\tilde{p}_5$ satisfy third-order ordinary differential equations which are independent of μ. Since $\mathcal{L}_3$ admits an eigensolution, we ensure uniqueness of $\bar{p}_3$ and $\tilde{p}_3$ by enforcing the additional conditions $\bar{p}_3''(0) = \tilde{p}_3''(0) = 0$. The solutions for $\bar{p}_3$, $\tilde{p}_3$, $\bar{p}_4$, $\bar{p}_5$ and $\tilde{p}_5$ are obtained by numerical integration. The values of $\bar{p}_4''(0)$, $\bar{p}_5''(0)$ and $\tilde{p}_5''(0)$ are determined by a shooting technique.

Finally, the wall shear, $U_0'(w) \equiv \phi_{\eta\eta}(\eta = 0)$, which appears in (4.29) has the asymptotic expansion

$$U_0'(w) = F_0''\left(1 + \mu\frac{\bar{i}_0}{w} + A_1\frac{\log w^2}{w^2} + \frac{B_1}{w^2} + \mu A_1 \bar{j}_0 \frac{\log w^2}{w^3} + \right. \qquad (D.8)$$

$$\left. \mu\frac{B_1\bar{j}_0 + \bar{k}_0 + \mu^2 \bar{l}_0}{w^3} + O(w^{-r_2})\right),$$

where the numerical constants are calculated to be

$$\left. \begin{array}{llll} \bar{\imath}_0 & \equiv p_1''(0)/F_0'' = & -3.591, & \bar{\jmath}_0 & \equiv \bar{p}_4''(0)/F_0'' = & 0.814, \\ \bar{k}_0 & \equiv \bar{p}_5''(0)/F_0'' = & 8.230, & \bar{l}_0 & \equiv \tilde{p}_5''(0)/F_0'' = & -3.235. \end{array} \right\} \quad (D.9)$$

The expression (4.31) for the curvature of the boundary-layer profile at the wall, $U_0''(w) \equiv \phi_{\eta\eta}(\eta = 0)$, which also appears in (4.29), immediately follows from (D.1) and (D.4), since $p_i'''(0) = d_i(0)$.